

SINGLE MOLECULE DETECTION ON SURFACES

THÈSE N° 3854 (2007)

PRÉSENTÉE LE 3 AOÛT 2007

À LA FACULTÉ DES SCIENCES ET TECHNIQUES DE L'INGÉNIEUR

Laboratoire d'optique biomédicale

PROGRAMME DOCTORAL EN PHOTONIQUE

ÉCOLE POLYTECHNIQUE FÉDÉRALE DE LAUSANNE

POUR L'OBTENTION DU GRADE DE DOCTEUR ÈS SCIENCES

PAR

Marcel LEUTENEGGER

ingénieur en microtechnique diplômé EPF
de nationalité suisse et originaire de Wängi (TG)

acceptée sur proposition du jury:

Prof. Ph. Renaud, président du jury

Prof. T. Lasser, directeur de thèse

Prof. S. Hell, rapporteur

Prof. H. Vogel, rapporteur

Prof. J. Widengren, rapporteur



ÉCOLE POLYTECHNIQUE
FÉDÉRALE DE LAUSANNE

Suisse
2007

The work presented in this thesis was performed at the Laboratoire d'Optique Biomédicale, École Polytechnique Fédérale de Lausanne, Lausanne, Switzerland.

The author gratefully acknowledges grants from the Swiss National Science Foundation (200021-103333) and from the European Commission (FuSyMEM project, 6th Framework Programme).

Contents

Abstract	v
Kurzfassung	vii
I Overview	9
1 Introduction	11
2 Theory	14
2.1 Excitation field	16
2.2 Excitation rate	17
2.3 Fluorescence	17
2.4 Emission rate	21
2.5 Emitted dipole field	26
2.6 Detection efficiency	27
2.7 Fluorescence signal	30
3 Experiments	32
3.1 Nano-apertures	32
3.2 Dual-color TIR-FFS	36
3.3 Membrane proteins	42
3.3.1 Sample preparation	49
3.3.2 Image correlation spectroscopy	50
3.3.3 Image segmentation	52
3.3.4 Point spread function	55
4 List of articles	56
5 Conference contributions	58
6 Conclusions and outlook	59
Acknowledgements	62
References	63
A Fluorescence	67

II Articles	69
L2 SMD at surfaces	71
L3 Focus fields	85
L4 2C-TIR-FCCS	101
L7 FCS on apertures	105
Curriculum vitae	119

Abstract

Monitoring biological relevant reactions on the single molecule level based on fluorescence spectroscopy techniques has become one of the most promising approaches for understanding a variety of phenomena in biophysics, biochemistry and life science. By applying techniques of fluorescence spectroscopy to labeled biomolecules a manifold of important parameters becomes accessible. For example, molecular dynamics, energy transfer, and ligand–receptor reactions can be monitored at the molecular level. This huge application field was and still is a major drive for innovative optical methods as it opens the door for new quantitative insights of molecular interactions on a truly micro- and nano-scope scale.

This thesis contributes new single molecule detection (SMD) concepts, correlation analysis and optical correlation spectroscopy to study fluorophores or labeled biomolecules close to a surface. The search beyond the classical confocal volume towards improved confinement was a key objective.

In a first approach, fluorescence correlation spectroscopy (FCS) using near field light sources to achieve highly confined observation volumes for detecting and measuring fluorophores up to micromolar concentration was investigated. In a second approach, FCS and fluorescence intensity distribution analysis (FIDA) based on dual-color total internal reflection fluorescence (TIRF) microscopy was conceived to achieve a common observation volume for dual-color fluorescence measurements.

This resulted in two novel fluorescence fluctuation spectroscopy instruments providing observation volumes of less than 100al. The first instrument generates a near field observation volume around and inside nano-apertures in an opaque metal film. Back-illumination of such an aperture results in a highly confined excitation field at the distal aperture exit. This instrument was characterized with FCS and observation volumes as small as 30al were measured. The second instrument confines the observation volume with total internal reflection (TIR) at a glass–water interface. Today, the last-generation instrument provides a dual-color ps pulsed excitation and time-resolved detection for coincidence analysis and time-correlated single photon counting. It was characterized with FCS and FIDA and observation volumes of 70al to 100al were achieved. Moreover, the presence of the interface favors emission into the optically denser medium, such that nearly 60% of the emitted fluorescence can be collected. This very efficient light collection resulted in a two- to three-fold stronger fluorescence signal and led to a high signal to background ratio, which makes this instrument particularly suitable for SMD studies on surfaces.

In parallel to these experimental investigations, a theoretical analysis of the total SMD process including an analysis of optical focus fields, molecule–interface interactions, as well as the collection and detection efficiency was performed. This analysis was used as a guideline for steady instrument improvements and for the understanding of the SMD process.

Finally, SMD concepts were applied for a first investigation of *in vitro* expression of an odorant receptor and for monitoring the vectorial insertion into a solid-supported lipid membrane. These receptors were incorporated and immobilized in the lipid membrane. With increasing expression time, an increasing amount of receptors as well as an increasing aggregation was observed. The incorporation density and the receptor aggregation were investigated with TIRF microscopy and image correlation spectroscopy.

Key words: Single molecule detection; Fluorescence microscopy; Fluctuation spectroscopy; Correlation spectroscopy; Evanescent field; Total internal reflection; Artificial membrane; Odorant receptor.

OCIS codes: (170.0180) Microscopy; (170.2520) Fluorescence microscopy; (300.2530) Fluorescence, laser induced; (170.6280) Spectroscopy, fluorescence and luminescence; (240.6490) Spectroscopy, surface; (240.6690) Surface waves; (220.2560) Focus; (070.2580) Fourier optics; (260.1960) Diffraction theory; (050.1220) Apertures; (160.3900) Metals; (100.2000) Digital image processing; (100.2960) Image analysis.

Kurzfassung

Die Beobachtung biologisch relevanter Reaktionen auf Einzelmolekülebene mittels Fluoreszenzspektroskopie ist eine der vielversprechendsten Methoden für das Verständnis vieler Phänomene in der Biophysik, der Biochemie und in den Lebenswissenschaften geworden. Eine Vielzahl von wichtigen Parametern wurde durch Fluoreszenzspektroskopie von fluoreszierenden Biomolekülen zugänglich. Zum Beispiel können die Dynamik von Molekülen, Energietransfers und Ligand-Rezeptor-Reaktionen auf Einzelmolekülebene gemessen werden. Dieses grosse Anwendungsgebiet förderte und fordert weiterhin innovative optische Konzepte, da diese neuen Methoden einen Zugang zu quantitativen Einblicken in die Interaktion von Molekülen im Mikro- und Nanometer-Masstab erlauben.

Diese Arbeit stellt neue Konzepte zur Einzelmoleküldetektion sowie zur Korrelationsanalyse und -spektroskopie vor, um fluoreszierende Farbstoffe oder Biomoleküle an Oberflächen zu untersuchen. Ein ständiges Hauptziel war die Suche nach deutlich kleineren Beobachtungsvolumen als mittels klassischer Technik erreicht werden können.

In einem ersten Ansatz wurden Fluoreszenz-Korrelations-Spektroskopie (FCS) und Nahfeld-Lichtquellen untersucht, um immer kleinere Beobachtungsvolumen zur Detektierung und Charakterisierung von Farbstoffen bis zu einer mikromolaren Konzentration zu erreichen. In einem zweiten Ansatz wurden FCS und Fluoreszenz-Intensitäts-Verteilungs-Analysen (FIDA) im evaneszenten Lichtfeld eines intern total reflektierten Laserstrahls entwickelt, um ein überlappendes Beobachtungsvolumen für Zweifarbmessungen an der Oberfläche zu erzeugen.

Daraus ergaben sich zwei neuartige Messinstrumente für Fluoreszenzspektroskopie, welche Beobachtungsvolumen von 100al oder weniger erreichen. Das erste Instrument erzeugt dieses Beobachtungsvolumen im optischen Nahfeld eines Nanolochs durch einen undurchsichtigen Metallfilm. Die rückseitige Beleuchtung eines Nanolochs führt zu einem Lichtfeld an der Austrittsöffnung, welches auf die Dimension der Öffnung beschränkt bleibt. Dieses Instrument wurde mittels FCS charakterisiert und Beobachtungsvolumen bis hinunter zu 30al gemessen. Das zweite Instrument schränkt das Beobachtungsvolumen ein, indem es einen Laserstrahl an der Deckglas-Wasser-Grenzfläche intern total reflektiert (TIRF). Der aktuelle Aufbau ermöglicht gepulste Anregung mit ps-Laserpulsen und zeitaufgelöste Messungen zur Koinzidenzanalyse und zeitkorrelierter Einzelphotonenspektroskopie. Dieses Instrument wurde mit FCS und FIDA charakterisiert und Beobachtungsvolumen von 70al bis 100al gemessen. Die nahe Glasoberfläche begünstigt die Fluoreszenzabstrahlung in das optisch dichtere Medium, so dass fast 60% der Gesamtfluoreszenz erfasst werden kann. Diese sehr hohe Lichtausbeute ergab ein zwei- bis dreifach helleres Signal und führte zu einem hohen Signal-zu-Hintergrund-Verhältnis, welches das Instrument für die Einzelmoleküldetektion an Oberflächen prädestiniert.

Parallel zu den experimentellen Arbeiten wurde eine vollständige theoretische Analyse des kompletten Vorgangs der Einzelmoleküldetektion durchgeführt. Diese Analyse beinhaltet eine Untersuchung von optischen Fokusfeldern, der Interaktion von Molekülen mit der Oberfläche, sowie der Detektionseffizienz. Sie diente als Leitfaden zur fortwährenden Verbesserung der Messinstrumente und vertiefte das Verständnis des Messvorgangs.

Schliesslich wurden Methoden der Einzelmoleküldetektion angewendet, um erste Untersuchungen des gerichteten *in-vitro*-Einbaus von Geruchsrezeptoren in fixierten Lipidmembranen durchzuführen. Die Geruchsrezeptoren wurden in die Membran eingebaut und darin immobilisiert. Mit zunehmender Einbaudauer wurde eine erhöhte Einbaudichte sowie eine verstärkte Aggregation von Rezeptoren nachge-

wiesen. Einbaudichte und Aggregation wurden mittels TIRF-Mikroskopie sowie Bildverarbeitung und Korrelationsanalyse gemessen.

Schlüsselwörter: Einzelmoleküldetektion; Fluoreszenzmikroskopie; Fluktuationsspektroskopie; Korrelationspektroskopie; Evaneszentes Feld; Totale interne Reflektion; Künstliche Membrane; Geruchsrezeptor.

OCIS Codes: (170.0180) Mikroskopie; (170.2520) Fluoreszenzmikroskopie; (300.2530) Fluoreszenz, Laser-induziert; (170.6280) Spektroskopie, Fluoreszenz und Lumineszenz; (240.6690) Oberflächenwellen; (240.6490) Spektroskopie, Oberfläche; (220.2560) Fokus; (070.2580) Fourieroptik; (260.1960) Diffraktionstheorie; (050.1220) Öffnungen; (160.3900) Metalle; (100.2000) Digitale Bildverarbeitung; (100.2960) Bildanalyse.

Part I

Overview

Chapter 1

Introduction

In the past three decades, fluorescence imaging and spectroscopy became an integral part in life science, cellular and molecular biology, and medicine. Research in these fields is more and more driven by the availability of specific labeling and sensitive measurement techniques. The combination of bright fluorescent markers with ultra-sensitive measurement instrumentation enabled investigations down to the single molecule level with unprecedented spatio-temporal resolution and sensitivity. Progress in microscopy, detector and signal processing technology still continues pushing fluorescence techniques to ever-new horizons.

Classical fluorescence microscopy and fluorescence lifetime imaging (FLIM) [1, 2, 3] allow localizing and identifying cellular structures within tissue or sub-cellular structures within cells. Fluorescence (time-)correlation spectroscopy (FCS) [4, 5], fluorescence intensity distribution analysis (FIDA) [6, 7], fluorescence recovery after photo-bleaching (FRAP) [8], fluorescence image correlation spectroscopy (ICS) [70], Förster resonant energy transfer (FRET) [10] and many other techniques are suitable for characterizing samples at the molecular level. In addition, multi-parameter fluorescence detection and fluorescence burst analysis [11] allow characterizing and identifying single molecules. All these techniques rely on the Stokes shift between the excitation light and the induced fluorescence emission as well as state of the art instrumentation. Whereas the Stokes shift allows a very selective chromatic filtering to separate the fluorescence emission from the excitation light, the instrument should also provide a high collection efficiency of the fluorescence emission and an efficient shot-noise limited single photon detection. Altogether, these features contribute to a high signal to background ratio (SBR) as well as an unprecedented signal to noise ratio (SNR). A corner stone was set in the late 1980s, when the first individual fluorophores in a biologically relevant environment were observed [12]. This break-through opened a vast field of fluorescence imaging and spectroscopy applications and marked the renaissance of *single molecule detection* (SMD) [13]. It marked also the transition from former time-resolved flash lamp techniques to a much simpler instrumentation: the confocal microscope [14]. Thanks to its compactness, robustness, efficiency and ease-of-use, the confocal microscope became rapidly *the* base platform for virtually all fluorescence techniques. Since the very beginnings, fluorescence spectroscopy was extensively applied for investigating processes at the nanometer scale, i.e. chemical reactions [15], enzyme activity [16], molecular motors [17], intra-cellular transport and signaling [18]. Reviews of SMD applications are found in [5, 19, 20]; and Wazawa and Ueda [21] reviewed SMD imaging techniques and applications.

A very interesting class of fluorescence techniques featuring single-molecule sensitivity is fluorescence fluctuation spectroscopy (FFS). Whereas imaging techniques rely on the (time-)average fluorescence intensity, FFS regroups techniques analyzing spatio-temporal fluctuations of the fluorescence intensity. These fluctuations are caused by various kinetic processes in the sample, i.e. translational and rotational diffusion due to thermal (Brownian) motion, active or passive transport, flow and triplet blinking. In principle, every process manifesting itself in a fluctuating fluorescence intensity can be investigated with FFS. For observing and measuring these fluctuations with high fidelity, the detection system must follow the time course of these photon events, i.e. the total detection bandwidth must be high enough for capturing the signal content encoded in the detected photon trace. Single photon detectors, i.e. avalanche

photo diodes (APD), and digital signal processing are commonly used for that purpose. In addition, the observation volume must be small enough to observe only a few fluorophores simultaneously. FFS experiments in the 1970s and 1980s usually involved large sampling volumes populated by several thousand molecules. Due to the minute fluctuations around the average intensity, these measurements last typically several hours or even a day before achieving a sufficient SNR. However, using a confocal microscope the overall measurement time was substantially shortened to a *few seconds* [14]. A well-defined sampling volume smaller than 1fl is essential to achieve short measurements.

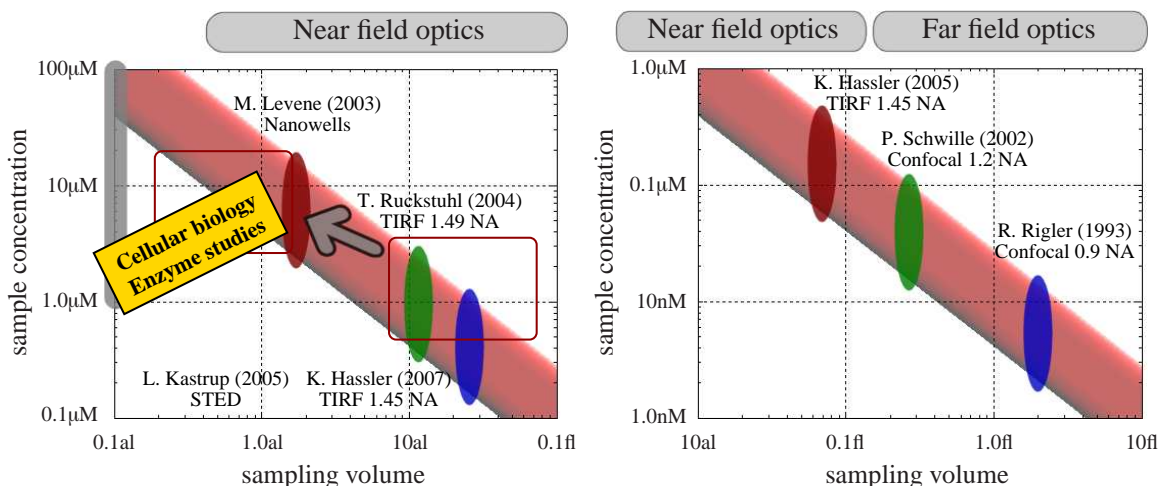


Figure 1.1: Evolution of the sampling volume and optimal concentration range for FFS measurements. The boxes outline the gap to bridge for single molecule DNA sequencing.

The evolution of the observation volume (sampling volume) in the past decades is outlined in figure 1.1, which indicates not only the progress but as well a trend towards applying FFS for higher concentrations. The indicated concentration range corresponds to a population N of 3–15 molecules in this volume. Rigler et al. [14] and Schwille et al. [18] used confocal microscopes with a numerical aperture (NA) of 0.9 and 1.2, respectively. Hassler et al. [22] and Ruckstuhl et al. [23] used an epi-illumination total internal reflection fluorescence (epi-TIRF) setup. An objective with ≥ 1.45 NA allowed obtaining a sampling volume of less than 50al. Kastrup et al. [24] generated nanoscale focal volumes by stimulated emission depletion (STED). To date, STED is the only method that can create nanoscale volumes *inside* the bulk sample, e.g. it does neither rely on optical near fields nor on a constrained sample volume. Levene et al. [25] proposed an evanescent epi-illumination at the bottom of a nano-aperture in a metal film. Except for fabrication issues, this method allows principally to reach sampling volumes far less than 1al. A similar concept using nano-channels in a transparent medium was proposed by Webb et al. [26].

The framework of this thesis was the development and the characterization of novel FFS concepts achieving sampling volumes significantly smaller than in the far field diffraction limit. This work was motivated by recent single enzyme investigations and receptor–ligand measurements. Single enzyme observation basically requires immobilizing the enzyme and feeding a fluorescent educt or obtaining a fluorescent product. Real-time observation of the enzyme activity is a true SMD application based on the ability to observe single educt molecules or the processing of substrate molecules. At room temperature or above, FFS is the method of choice because of its high SMD sensitivity and its fast time response. In consequence, at least the educt, the enzyme–educt/product complex or the product must be fluorescent. Immobilization is important because moving enzymes could not be observed for longer than the diffusion

time, which is typically a few milliseconds only. Recently, horseradish peroxidase was studied when oxidizing a quenched fluorophore and forming a fluorescent product [27]. This experimental scheme is relatively simple because only the product is bright, which allows SMD nearly regardless of the educt concentration.

As the sampling volume is the overlap volume of the excitation and the detection *in the sample*, reducing the excitation, the detection and/or the sample volume confines it. Near a surface, evanescent or plasmonic excitation reduces the excitation volume [28, 29] and anisotropic fluorescence emission reduces the detection volume [4, 7, 8, 22]. Besides a minute sampling volume, a high average brightness is desirable to overcome shot noise, background light and detector noise. Whatever confinement is used, the detection optics will rely on a high NA objective to maximize the detection efficiency and to confine the detection volume simultaneously. In this work, we focused on the confinement of the excitation volume. In a first investigation, we designed, fabricated and characterized nanohole arrays with sub-wavelength aperture diameters (section 3.1). In contrast to previous studies by Levene et al. [25] and Rigneault et al. [30], we proposed a trans-illumination concept for obtaining a small excitation volume above the apertures without restricting the sample volume. Although promising results were obtained, we abandoned these investigations due to the hole-to-hole variations, the sample preparation and handling. Instead, we enhanced a novel total internal reflection excitation scheme for dual-color excitation and detection (section 3.2). This versatile instrument achieves similar excitation volumes as with the nanoholes but offers a quite simple and inexpensive sample preparation and handling. It was then used for characterizing the insertion of membrane proteins into a solid-supported planar lipid membrane (section 3.3).

This thesis is organized as follows:

Chapter 2 gives an overview on fluorescence and instrumentation, which form the basis for FFS measurements. It presents the calculation of the core characteristic of any FFS instrument, namely the sampling volume and the fluorescence signal. This calculation integrates the excitation field, the response of the fluorophore and its interaction with the environment, as well as the detection efficiency of the collection optics. Chapter 3 summarizes the experiments and discusses key results. The FFS techniques relevant for these measurements are outlined. Limitations and artifacts are discussed and improvements are suggested. Section 3.1 presents a novel near field excitation for FFS measurements, which was able to provide sampling volumes as small as 30a³. Section 3.2 outlines a novel dual-color total internal reflection FFS instrument. An excellent performance for coincidence measurements was achieved. Section 3.3 presents an investigation of odorant receptors in a solid-supported lipid membrane. The measurements and first results are discussed. Chapter 4 and 5 list the author's articles and conference contributions, respectively. Finally, conclusions are drawn in chapter 6.

Chapter 2

Theory

Any FFS process can be described as a step-by-step process, e.g. a total process from excitation light-matter interaction until final detection and signal analysis. This chapter analyzes the FFS process with a special emphasis on the photonic and optical aspects. The FFS process is outlined in figure 2.1, signal processing and data analysis are summarized in chapter 3 with the corresponding measurements.

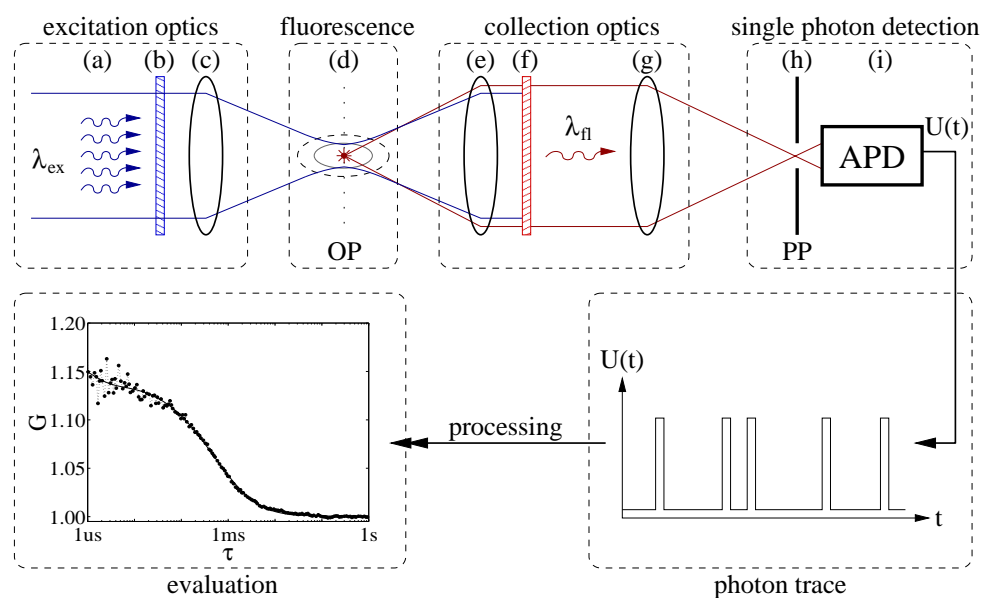


Figure 2.1: Overview of FFS methods for single molecule detection. OP: object plane, PP: conjugated pinhole plane. (a) Excitation light, (b) excitation band-pass filter, (c) focusing optics, (d) excitation (solid line) and detection (dashed line) volumes, (e) collection optics, (f) emission band-pass filter, (g) tube lens, (h) pinhole, (i) single photon detector.

Reprinted from Leutenegger et al. [2] with permission by American Chemical Society.

The excitation light (a) is spectrally filtered with a band-pass filter (b) and focused into the sample (c). The excitation field within the sample is well confined to provide a small open volume (d: solid) that is the excitation volume where the labeled molecules are excited. The induced fluorescence emission is collected (e) from within a small open detection volume (d: dashed) encompassing the excitation volume. A band-pass filter (f) separates the emission spectrum from the excitation spectrum (b). The fluorescence emission is then imaged (g) onto the pinhole (h), which provides a spatial filtering and defines the detection volume (d: dashed). A single photon detector (i) detects the fluorescence photons as a sequence of single photon events. Finally, this photon trace is numerically processed to extract information on the measured fluorescent sample.

Classically, a broadband light source (incandescent lamp) is used for fluorescence microscopy. How-

ever, laser light provides a much better defined source for obtaining a well-confined diffraction limited excitation volume. Therefore, the excitation light (a) was modeled as monochromatic and spatio-temporally coherent. An additional excitation filter (b) is usually required to block stray emission, i.e. blue/UV light from gas lasers (pump light) or red/IR light from solid-state lasers (spontaneous emission). The biological sample under investigation is contained in a solvent, i.e. water. The induced fluorescence is due to auto-fluorescent or specifically labeled structures. If not immobilized, these samples diffuse and rotate freely due to thermal motion. The fluorophore is described as a dipole absorbing photons at the excitation wavelength λ_{ex} and emitting fluorescence within a wavelength range λ_{fl} , where $\lambda_{fl} \gtrsim \lambda_{ex}$ for single photon excitation.

As usual, we omit the time dependency $\exp(-i\omega t)$, where $\omega = 2\pi c_0/\lambda$ is the angular frequency, c_0 the speed of light and λ the wavelength in free space. And we assume a relative magnetic permeability μ_r of 1 for all materials. Therefore, the refraction index n is given by the dielectric permittivity $\epsilon_r = n^2$.

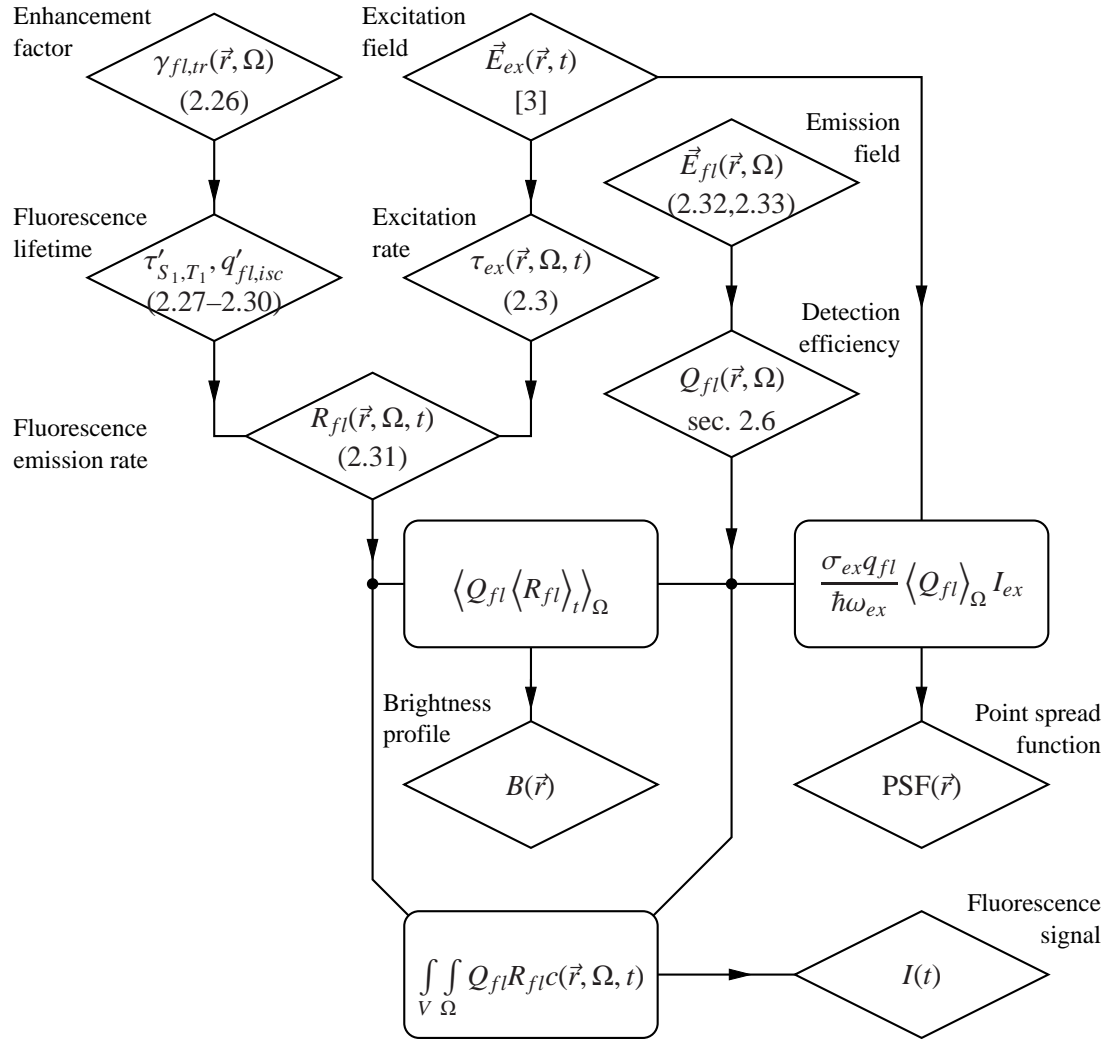


Figure 2.2: Overview of the fluorescence signal $I(t)$ calculation. The pathway starting from initial parameters as analyzed in this chapter is indicated.

Under these assumptions, we decompose the general FFS process as:

1. the excitation field $\vec{E}_{ex}(\vec{r}, t)$,
2. the excitation cross-section $\vec{\sigma}_{ex}(\vec{r}, \Omega)$ and the excitation rate $\tau_{ex}^{-1}(\vec{r}, \Omega, t)$ of the fluorophore,
3. the photo-physical and photo-chemical response of the fluorophore,
4. the emission rate $R_{fl}(\vec{r}, \Omega, t)$ of the fluorophore,
5. the emitted field $\vec{E}_{fl}(\vec{r}, \Omega)$ from the fluorophore and
6. the detection efficiency $Q_{fl}(\vec{r}, \Omega)$ of this radiation,
7. which yield finally the detected fluorescence signal $I(t)$ from the sample.

All these quantities vary in general with the position $\vec{r} = (x, y, z)$ and the dipole orientation $\Omega = (\Theta, \varphi)$ of the fluorophore, as well as with the wavelength of excitation and emission. The subscript refers to the wavelength used for calculating the corresponding quantity. A graphical representation is outlined in figure 2.2.

The main result of this description is the detected fluorescence signal $I(t)$ from the sample. As stated above, further processing and the analysis of $I(t)$ is presented together with measurement results in the following chapter 3.

2.1 Excitation field

The calculation of the excitation field for confocal excitation with high NA objectives was recently published by Leutenegger et al. [3] (annexed). It is based on the vectorial Debye diffraction integral expressed as a particular Fourier transform of the incident field in the aperture of a microscope objective. The efficient implementation allows the calculation of the excitation field $\vec{E}_{ex}(\vec{r}, t)$ within a 3D volume near the focus. With an 1.20 NA water immersion objective, excitation volumes of 0.3fl to 0.6fl are calculated for $\lambda_{ex} = 488\text{nm}$ and 633nm , respectively. At a glass–water interface, excitation volumes of about 70al can be achieved with a 1.45 NA oil immersion objective. Figure 2.3 shows an example calculation for a x -polarized excitation at $\lambda_{ex} = 488\text{nm}$.

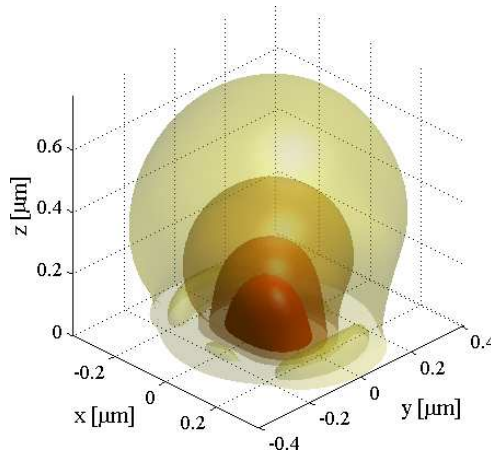


Figure 2.3: Intensity distribution near the focus of a 1.45 NA oil immersion objective. The iso-surfaces show $I(\vec{r}) = e^{-1 \dots -4} I_{(0)}$ in the sample.

In addition, in reference [7] (annexed), we showed results obtained with confined excitation volumes in the near field of sub-wavelength apertures in an opaque gold layer. With circular apertures of $\lambda_{ex}/3$ diameter, sampling volumes of about 50al for $\lambda_{ex} = 633\text{nm}$ were measured (see section 3.1). However, the gold added a significant background, which was very sensitive to small irregularities in the nano-apertures resulting from fabrication.

2.2 Excitation rate

This analysis is based on a classical description of absorption and re-emission, i.e. the fluorophore is described as an absorbing and emitting dipole. Any intrinsic fluorophore process can be integrated in a quantum-mechanical description, which will result in a semi-classical analysis of absorption and fluorescence. However, this is not of importance within the framework of this description as all molecule-specific processes are given with the absorption and emission spectra and lifetime parameters. A detailed quantum-mechanical description was recently given by Girard et al. [31].

Assuming a quickly rotating fluorophore, the absorption cross-section σ_{ex} is isotropic (time average). Such a fluorophore absorbs photons at a rate

$$\tau_{ex}^{-1}(\vec{r}, t) = \frac{\sigma_{ex}(\vec{r})}{\hbar\omega_{ex}} I_{ex}(\vec{r}, t) \quad (2.1)$$

where I_{ex} is the excitation intensity given by

$$I_{ex}(\vec{r}, t) = \frac{1}{2} \sqrt{\frac{\epsilon_0}{\mu_0}} \text{Re}(n) \vec{E}_{ex}^{*T}(\vec{r}, t) \vec{E}_{ex}(\vec{r}, t). \quad (2.2)$$

\vec{E}_{ex}^{*T} denotes the conjugate transpose of the electric field vector. This isotropic description is valid if the mean excitation time τ_{ex} is much longer than the mean rotation time τ_r of the molecule. Otherwise, the orientation of the fluorophore has to be taken into account. The excitation rate is then given by

$$\tau_{ex}^{-1}(\vec{r}, \Omega, t) = \frac{\text{Re}(n)}{2\hbar\omega_{ex}} \sqrt{\frac{\epsilon_0}{\mu_0}} \vec{E}_{ex}^{*T}(\vec{r}, t) \overleftrightarrow{\sigma}_{ex}(\vec{r}, \Omega) \vec{E}_{ex}(\vec{r}, t). \quad (2.3)$$

For a fluorophore with a single absorption transition dipole, the orientation dependent absorption cross-section is a diagonal tensor.

$$\overleftrightarrow{\sigma}_{ex}(\vec{r}, \Omega) = \sigma_{ex}(\vec{r}) \begin{pmatrix} |\cos \varphi \sin \Theta| & 0 & 0 \\ 0 & |\sin \varphi \sin \Theta| & 0 \\ 0 & 0 & |\cos \Theta| \end{pmatrix} \quad (2.4)$$

2.3 Fluorescence

The Jablonski diagram 2.4 outlines the molecular energy levels and electronic states as well as the transitions governing fluorescence. S_0 is the ground state of the fluorophore, S_1 the first excited state and T_1 the lowest triplet state. In thermal equilibrium, the occupation probability of the energy levels is given by the Maxwell-Boltzmann distribution. The energy differences between S_0 and the excited states are sufficiently large that within a very good approximation all fluorophores are in S_0 . τ_{fl} , τ_{nr} , τ_{isc} and τ_{T_1}

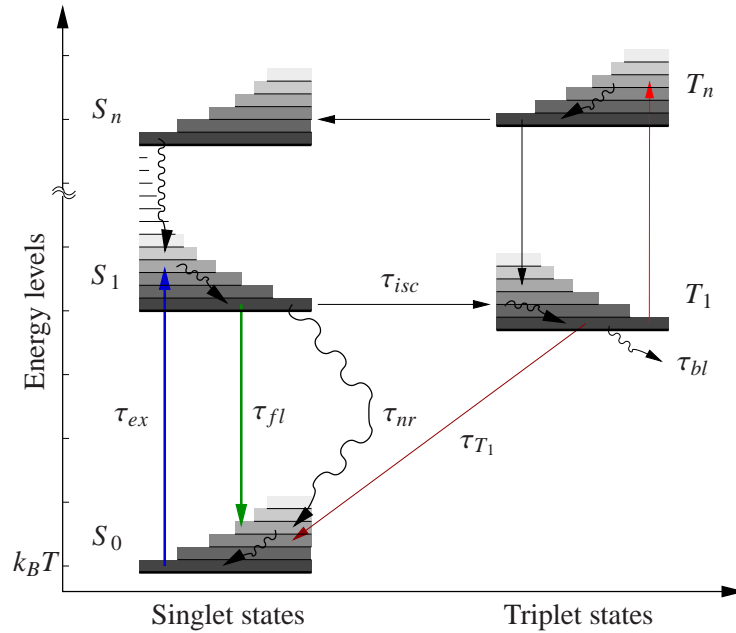


Figure 2.4: Molecular energy levels, electronic states and transition rates (τ_{xx}^{-1}). Thin lines indicate vibration and rotation sub-levels of the electronic states.

are the fluorescence lifetime, the non-radiative transition lifetime (internal conversion), the intersystem crossing lifetime and the triplet state lifetime, respectively. τ_{ex} is the average excitation time as calculated previously.

When absorbing a photon (blue \uparrow) with wavelength λ_{ex} the fluorophore becomes excited, that means it transits from S_0 to one of the excited singlet states S_n . The absorption is strongest if the photon energy matches the energy difference for a transition $S_0 \rightarrow S_1$. If the absorbed photon energy is higher, the excess energy is usually dissipated within a few picoseconds down to the first excited state S_1 (black \curvearrowright), that is the fluorophore does not stay in S_n .

After the absorption, the fluorophore relaxes to a low sublevel of S_1 before it returns to S_0 or transits to T_1 by a non-radiative intersystem crossing. A radiative transition to S_0 (green \downarrow) leads to the emission of a fluorescence photon with wavelength $\lambda_{fl} > \lambda_{ex}$. Internal conversion to S_0 (black \curvearrowright) is mostly due to collisions with solvent molecules inducing energy transfer or dissipation. From the triplet state T_1 , the fluorophore returns to S_0 (dark red \swarrow) by emission of a phosphorescence photon ($\lambda_{ph} > \lambda_{fl}$) or by energy dissipation. Because the transitions $S_1 \rightarrow T_1$ and $T_1 \rightarrow S_0$ are spin-forbidden, they occur only with low probability. This makes the triplet state T_1 metastable with a lifetime τ_{T_1} in the range of micro- to milliseconds or even longer, whereas the lifetime τ_{S_1} of the excited state S_1 is only a few nanoseconds.

The fluorescence process is described in standard textbooks, i.e. Lakowicz [32]. A short summary is given in the appendix A. Taking into account just S_0 , S_1 and T_1 and solving for the occupation probability P_{S_1} , the average rate of fluorescence emissions per molecule is obtained:

$$R_{fl} = \frac{q_{fl}}{\tau_{ex} + \tau_{S_1} + q_{isc}\tau_{T_1}} \quad (2.5)$$

where $\tau_{S_1} = (\tau_{fl}^{-1} + \tau_{nr}^{-1} + \tau_{isc}^{-1})^{-1}$ is the singlet state lifetime, $q_{fl} = \tau_{S_1}/\tau_{fl}$ is the fluorescence quantum yield and $q_{isc} = \tau_{S_1}/\tau_{isc}$ is the intersystem crossing probability. The denominator $\tau_{ex} + \tau_{S_1} + q_{isc}\tau_{T_1}$

corresponds to the average cycle time. At strong excitation, $\tau_{ex} \rightarrow 0$ and the fluorescence emission saturates as exemplified by figure 2.5 for Rhodamine Green in water. If this fluorophore is excited near

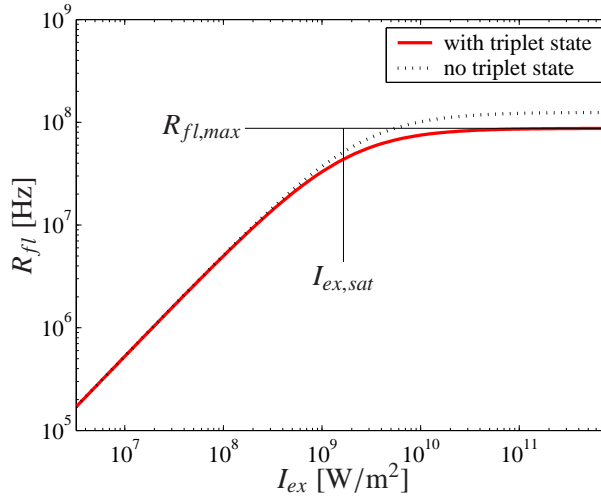


Figure 2.5: Saturation of Rhodamine Green in water for excitation intensities I_{ex} above the saturation intensity $I_{ex,sat} = 1.65\text{mW}/\mu\text{m}^2$. Assuming a quantum yield $q_{fl} = 52\%$, the maximal emission rate is $R_{fl,max} = 87\text{MHz}$.

its absorption peak in a confocal configuration with a 1.20 NA water immersion objective, it is not uncommon to reach detection count rates of $\gtrsim 100\text{kHz}$ per molecule (kCPM). For instance, a focused laser beam with a power of $400\mu\text{W}$ at $\lambda_{ex} = 488\text{nm}$ or $160\mu\text{W}$ at $\lambda_{ex} = 514\text{nm}$ results in an emission rate $R_{fl} \approx 25\text{MHz}$. The average brightness \bar{B} can then be as high as about 200kCPM depending on filtering, transmission and detection losses.

As a rule of thumb, an input power $P_{ex} \gtrsim 100\mu\text{W}$ results in a fluorescence power $P_{fl} \lesssim 1\text{pW}/\text{molecule}$ on the detector. For single molecule detection it is therefore of vital importance to detect no more than about $10^{-9} P_{ex}$ of laser light (background). On a confocal microscope for instance, $\lesssim 0.1\%$ of the laser power is back scattered in the sampling volume (far from optical interfaces). The dichroic mirror transmits $\approx 1\%$ of this laser light and the band pass filter a fraction of $\approx 10^{-6}$, respectively. In this example, only a fraction $\lesssim 10^{-11}$ of the initial laser light reaches the detector which results in a background count rate of $\approx 1\text{kHz}$ and a signal to background ratio (SBR) $\gtrsim 100$.

So far, we assumed that the fluorophore characteristics do not alter with time. But real fluorophores undergo chemical interactions and/or permanent structural changes. For instance, bleaching is an irreversible chemical or structural modification of the fluorophore blocking the fluorescence emission. As a major consequence, the information yield per fluorophore is ultimately bleaching-limited.

As such, bleaching is a rather complicated phenomenon due to the many possible pathways [33, 34, 35, 36]. Figure 2.4 just outlines one of the major processes, namely the photodecomposition of the fluorophore at a rate $1/\tau_{bl}$ from the triplet state T_1 . Bleaching from T_1 is important because (a) the triplet state is long-lived, that means that energy transfer to collision partners is likely, and because (b) oxygen is an efficient triplet quencher, thereby becoming a radical. In addition, indirect bleaching from T_1 is probable if secondary excitations by light to T_n occurs because the energy of higher excited states can be sufficient to photo-dissociate the fluorophore directly.

In general, every excited state can be associated with a bleaching rate accounting for all potential

bleaching processes initiated from that state. From the first excited states S_1 and T_1 , bleaching is mainly attributed to chemical reactions with binding partners as the fluorophore's excitation energy significantly lowers the activation barrier. From higher excited states S_n and T_n , bleaching due to broken chemical bonds can become significant or even dominant. In consequence, the overall survival time of the fluorophore depends strongly on the excitation intensity. Figure 2.6 sketches the average number of fluorescence photons per fluorophore N_{bl} versus the excitation intensity I_{ex} . For weak excitation, N_{bl}

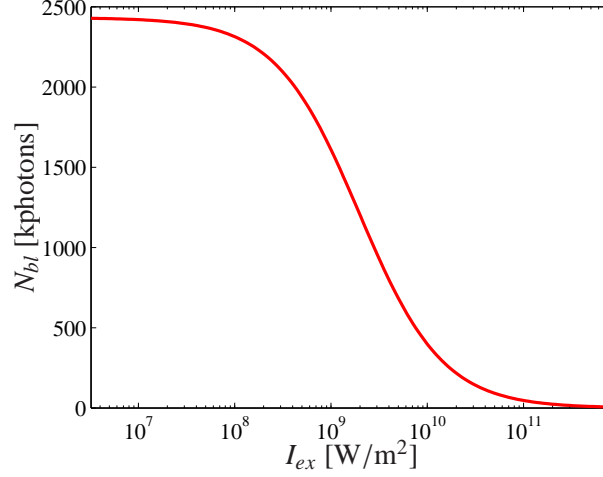


Figure 2.6: Average number of photon emissions before bleaching N_{bl} versus excitation intensity I_{ex} . N_{bl} decreases due to $T_1 \rightarrow T_n$ excitations, which become significant at about the saturation intensity in this example.

is maximum and does not depend on I_{ex} . Introducing a bleaching rate $\tau_{bl,ss}^{-1}$ from state ss , the average bleaching probability q_{bl} per cycle is expressed as

$$q_{bl} = 1 - \prod_{ss} (1 - q_{bl,ss}) = 1 - \left(1 - \frac{\tau_{S_1}}{\tau_{bl,S_1}}\right) \left(1 - q_{isc} \frac{\tau_{T_1}}{\tau_{bl,T_1}}\right) \quad (2.6)$$

where $q_{bl,ss} = \tau_{bl,ss}^{-1} \cdot \text{occupation time/cycle}$ is the bleaching probability from state ss . The average fluorescence yield per fluorophore is then simply

$$N_{bl} = \frac{q_{fl}}{q_{bl}}. \quad (2.7)$$

At medium excitation, secondary triplet excitation $T_1 \rightarrow T_n$ becomes significant (red \uparrow) and N_{bl} decreases [37, 38, 39]. Taking into account only triplet transitions $T_1 \leftrightarrow T_n$ where $\tau_{ex,T_1}^{-1} = \sigma_{ex,T_1} I_{ex} / \hbar \omega_{ex}$ is the mean excitation rate $T_1 \rightarrow T_n$, the bleaching yield from T_n is given by

$$q_{bl,T_n} = 1 - \left(1 - \frac{\tau_{T_n}}{\tau_{bl,T_n}}\right)^{q_{isc} \tau_{T_1} / \tau_{ex,T_1}} \quad (2.8)$$

where the exponent is the average number of $T_1 \rightarrow T_n$ excitations per cycle. For strong excitation, even secondary singlet excitations $S_1 \rightarrow S_n$ are possible and N_{bl} is further decreased. Fluorescence measurements are commonly performed at weak to medium excitation conditions. However, strong excitation is easily encountered with pico- or femtosecond pulsed laser excitation, even if the average excitation

intensity is lower than for cw excitation. For instance, two-photon excitation can efficiently excite many fluorophores due to the broad two-photon absorption spectra. But it is known to enhance bleaching by exciting higher singlet states S_n and/or high vibration levels of S_1 .

2.4 Emission close to planar interfaces

The previous section 2.3 described a fluorophore residing inside a homogeneous medium, e.g. far from any interface. This section describes the interaction of the fluorophore with planar layers and calculates the emission rate $R_{fl}(\vec{r}, \Omega, t)$.

The decay rate Γ of an electronic state defines the overall rate of all de-excitation channels from that state. In general, Γ contains a radiative decay Γ_{em} and a non-radiative decay Γ_{nr} and is simply

$$\Gamma(\vec{r}, \Omega) = \Gamma_{em}(\vec{r}, \Omega) + \Gamma_{nr} . \quad (2.9)$$

Γ_{em} is associated with electromagnetic radiation in, and interaction with, the environment; whereas Γ_{nr} stands for any non-electromagnetic dissipation, i.e. an intrinsic relaxation. The presence of a layered structure affects the radiative decay Γ_{em} of the fluorophore because it modifies the local density of states (LDOS). For instance, a high index medium in the near field of the fluorophore increases the LDOS at the fluorophore position. In consequence, Γ_{em} increases, or equivalently τ_{S_1} is shortened, because more radiation modes are available. On the other hand, Γ_{nr} is assumed to depend only on the fluorophore's microenvironment. Therefore, Γ_{nr} is not affected by the position and orientation dependent LDOS but rather by adsorption to a surface.

The dissipated power in a semi-classical picture is given by the dipole–light interaction. In a quantum-mechanical description, the dissipated power is analyzed with the transition probabilities and results in equivalent formulae. In the following, the dissipated power of a point dipole with fixed dipole moment $\vec{\mu}$ is calculated for two cases:

- a) inside a homogeneous medium, e.g. far from interfaces, and
- b) near a planar structured medium, e.g. near planar interfaces.

First, case (a) is calculated as reference for obtaining the radiative enhancement factor $\gamma(\vec{r}, \Omega)$ in case (b). Because $\Gamma_{em} = P/\hbar\omega$, the radiative enhancement $\gamma(\vec{r}, \Omega) = \Gamma_{em}(\vec{r}, \Omega)/\Gamma_{em,\infty}$ is reproduced by the ratio $P(\vec{r}, \Omega)/P_\infty$, where the subscript ∞ indicates the unperturbed case (a). In this context, we should keep in mind that the dissipated power describes the total power emitted via the dipole field, i.e. photon emission as well as radiative loss.

In the late seventies, Lukosz calculated the emission of electric and magnetic dipoles near a planar dielectric interface [40, 41]. In the eighties, Burghardt and Thompson [42] and Hellen and Axelrod [43] refined the calculation for TIRF microscopy. Recently, Novotny [44] revisited the theory for calculating the light field of interacting dipolar particles; and Mertz [45] unified the description of a classical dipole near a dielectric interface with a simple input–output formalism based on the Lorentz reciprocity theorem. The following description relies on the general ideas given by Ford and Webber [46]. This description is particularly advantageous because only the electric field at the dipole position is required for calculating the dissipated power. Figure 2.7 introduces the coordinate system for the calculation. The total dissipated power of a point dipole (fluorophore) at position \vec{r}_0 is given by

$$P = \frac{\omega}{2} \text{Im} \left(\vec{\mu}^* \cdot \vec{E}(\vec{r}_0) \right) \quad (2.10)$$

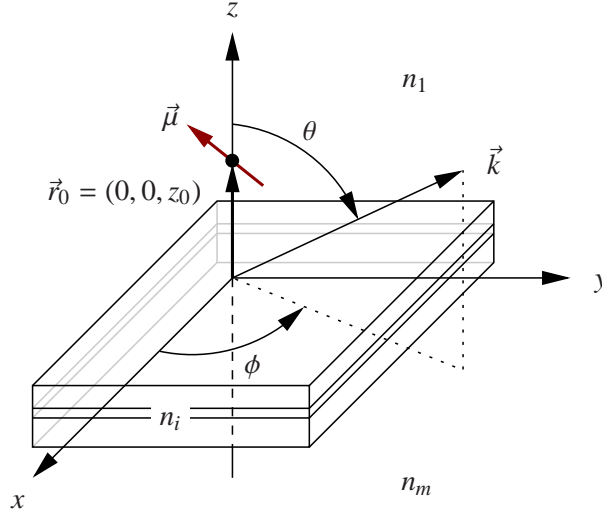


Figure 2.7: Dipole $\vec{\mu}$ located at \vec{r}_0 above the first interface. n_1 is the refractive index of the upper half-space ($z > 0$) around the dipole. n_m is the refractive index of the lower half-space ($z < -d$) and n_i the refractive indices of the intermediate layers ($-d < z < 0$).

where $\vec{\mu}$ is the dipole moment and $\vec{E}(\vec{r})$ the electric field radiated by this dipole. The dipole is described as a current source $\vec{j}(\vec{r}) = -i\omega\vec{\mu}\delta(\vec{r} - \vec{r}_0)$ in medium 1 and the radiated field has to fulfill the Maxwell equations.

$$\vec{\nabla} \times \vec{E}(\vec{r}) = \mu_0 \frac{\partial}{\partial t} \vec{H}(\vec{r}) \quad \vec{\nabla} \times \vec{H}(\vec{r}) + \epsilon_0 \epsilon_1 \frac{\partial}{\partial t} \vec{E}(\vec{r}) = \vec{j}(\vec{r}) \quad (2.11)$$

Using time harmonic fields and a plane wave expansion

$$\vec{E}(\vec{r}) = \int \vec{E}_k \exp(i\vec{k} \cdot \vec{r}) d\vec{k} \quad (2.12)$$

the Maxwell equations (2.11) read as

$$\vec{k} \times (\vec{k} \times \vec{E}_k) + k_1^2 \vec{E}_k = -\omega^2 \mu_0 \vec{\mu} \delta(\vec{r} - \vec{r}_0). \quad (2.13)$$

Solving for the electric field \vec{E}_k propagating along \vec{k} yields

$$\vec{E}_k = -\mu_0 \exp(-i\vec{k} \cdot \vec{r}_0) \frac{\omega^2}{k_1^2} \left(\vec{\mu} + \frac{\vec{k} \times (\vec{k} \times \vec{\mu})}{k^2 - k_1^2} \right). \quad (2.14)$$

Substituting this expression in (2.12) and splitting the lateral and axial integration, an integral representation of the radiated field is obtained.

$$\begin{aligned} \vec{E}(\vec{r}) = & -\mu_0 \frac{\omega^2}{k_1^2} \int d\vec{k}_{xy} \exp(i\vec{k}_{xy} \cdot (\vec{r} - \vec{r}_0)) \\ & \times \int_{-\infty}^{+\infty} dk_z \left(\vec{\mu} + \frac{\vec{k} \times (\vec{k} \times \vec{\mu})}{k_z^2 - k_{1z}^2} \right) \exp(ik_z(z - z_0)) \end{aligned} \quad (2.15)$$

The k_z integral is a contour integral in the complex plane, which can be evaluated using the complex residues at the first order poles $k_z = \pm k_{1z}$. With $\vec{k}_1 = \vec{k}_{xy} + \vec{k}_{1z}(z - z_0)/|z - z_0|$, the electric field is then

$$\begin{aligned} \vec{E}(\vec{r}) = & -2\pi\mu_0 \frac{\omega^2}{k_1^2} \int d\vec{k}_{xy} \exp(i\vec{k}_{xy} \cdot (\vec{r} - \vec{r}_0)) \\ & \times \left\{ \delta(z - z_0) \vec{\mu}_z + \frac{i}{2k_{1z}} \vec{k}_1 \times (\vec{k}_1 \times \vec{\mu}) \exp(ik_{1z}|z - z_0|) \right\}. \end{aligned} \quad (2.16)$$

The first term does not contribute to the dissipated power because it is real valued. The second term is imaginary only for $k_{xy} < k_1$, which is the far field radiation domain in medium 1. Now, the dissipated power is obtained with (2.10) and

$$\vec{E}(\vec{r}_0) = -i\pi\mu_0 \frac{\omega^2}{k_1^2} \int_{k_{xy} < k_1} \frac{d\vec{k}_{xy}}{k_{1z}} \vec{k}_1 \times (\vec{k}_1 \times \vec{\mu}) \quad (2.17)$$

Integrating over all directions of \vec{k}_{xy} yields

$$P_\infty = \frac{\pi^2 \mu_0 \omega^3}{2k_1^2} \int_0^{k_1} dk_{xy} \frac{k_{xy}}{k_{1z}} \left(2k_{xy}^2 |\vec{\mu}_z|^2 + (2k_1^2 - k_{xy}^2) |\vec{\mu}_{xy}|^2 \right), \quad (2.18)$$

and the dissipated power is finally given by

$$P_\infty = \frac{2}{3} \pi^2 \mu_0 \omega^3 k_1 |\vec{\mu}|^2. \quad (2.19)$$

Note Equation (2.16) describes the electric field by the coupling between the dipole moment $\vec{\mu}$ and the electric field \vec{E}_k , i.e. by a projection of $\vec{\mu}$ onto \vec{E}_k . The projection is expressed by $\vec{k}_1 \times (\vec{k}_1 \times \vec{\mu})$, which requires particular attention if $\text{Im}(\vec{k}_1) \neq 0$. This is taken into account using equation (2.20) below.

In the second case (b) where the dipole is near to planar interfaces, the radiation towards the interfaces is partially reflected and interferes with the direct radiation \vec{E}_d of the dipole as outlined in figure 2.8. The calculation involves the reflection coefficients $r_{1m}^{p,s}$ at the interfaces $n_1 \rightarrow n_m$ for p - and s -polarized fields $\vec{E}_k^{p,s}$. Therefore, the field in equation (2.16) is separated in the p - and s -polarized components using the vector identity

$$-\vec{k}_1 \times (\vec{k}_1 \times \vec{\mu}) = (\vec{p} \cdot \vec{\mu}) \vec{p} + (\vec{s} \cdot \vec{\mu}) \vec{s} \quad (2.20)$$

where $\vec{p} = k_{xy} \vec{e}_z + k_{1z} \vec{e}_{xy}$ and $\vec{s} = k_1 \vec{e}_z \times \vec{e}_{xy}$ with the unit vectors $\vec{e}_{xy} = \vec{k}_{xy}/k_{xy}$ and $\vec{e}_z = (0, 0, 1)$. Hence, the first term gives the p -polarized component \vec{E}_k^p and the second the s -polarized component \vec{E}_k^s . Using this in equation (2.16), the field propagating towards the interfaces is

$$\vec{E}^\downarrow(\vec{r}) = i\pi\mu_0 \frac{\omega^2}{k_1^2} \int \frac{d\vec{k}_{xy}}{k_{1z}} \exp(i\vec{k}_{xy} \cdot (\vec{r} - \vec{r}_0) - ik_{1z}(z - z_0)) \{ (\vec{p} \cdot \vec{\mu}) \vec{p} + (\vec{s} \cdot \vec{\mu}) \vec{s} \}. \quad (2.21)$$

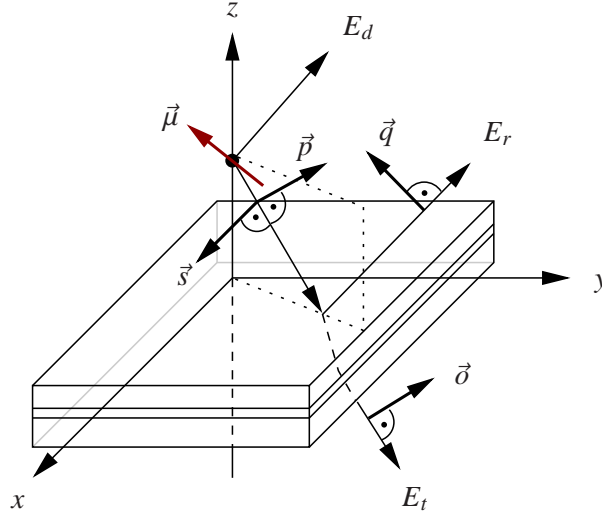


Figure 2.8: Coupling of the dipole moment $\vec{\mu}$ with the electric fields. E_d represents the direct dipole field, E_r the reflected field and E_t the transmitted field. \vec{s} is perpendicular to the incidence plane, whereas \vec{p} , \vec{q} and \vec{d} are parallel to the incidence plane.

The total field in the region $0 < z < z_0$ is this downward propagating dipole field plus an upward propagating reflected field. Upon reflection, the p -polarized component becomes proportional to $\vec{q} = k_{xy}\vec{e}_z - k_{1z}\vec{e}_{xy}$. Therefore, the total field in this region is

$$\vec{E}^{\uparrow\downarrow}(\vec{r}) = i\pi\mu_0 \frac{\omega^2}{k_1^2} \int \frac{d\vec{k}_{xy}}{k_{1z}} \exp(i\vec{k}_{xy} \cdot (\vec{r} - \vec{r}_0) + ik_{1z}z_0) \times \quad (2.22)$$

$$\left\{ (\vec{p} \cdot \vec{\mu}) \left(\exp(-ik_{1z}z) \vec{p} + r_{1m}^p \exp(ik_{1z}z) \vec{q} \right) + (\vec{s} \cdot \vec{\mu}) \left(\exp(-ik_{1z}z) + r_{1m}^s \exp(ik_{1z}z) \right) \vec{s} \right\}$$

where $r_{1m}^{p,s}$ are the reflection coefficients on the structure n_1 to n_m for p - and s -polarizations. The power dissipated by the dipole in the presence of the planar interfaces is obtained by inserting (2.22) in (2.10). Integrating over all directions of \vec{k}_{xy} , the dissipated power for a dipole at position \vec{r} is

$$P(\vec{r}, \Omega) = \frac{\pi^2 \mu_0 \omega^3}{2k_1^2} \text{Re} \int_0^\infty dk_{xy} \frac{k_{xy}}{k_{1z}} \left\{ 2k_{xy}^2 \left(1 + r_{1m}^p \exp(2ik_{1z}z) \right) |\vec{\mu}_z|^2 \right. \quad (2.23)$$

$$\left. + \left[k_1^2 \left(1 + r_{1m}^s \exp(2ik_{1z}z) \right) + |\vec{\mu}_{xy}|^2 k_{1z}^2 \left(1 - r_{1m}^p \exp(2ik_{1z}z) \right) \right] |\vec{\mu}_{xy}|^2 \right\}$$

The dissipated power in case (b) can be rewritten as P_∞ plus a contribution $\Delta P_z(\vec{r}, \Omega)$ from $\vec{\mu}_z$ perpendicular to the structure and a contribution $\Delta P_{xy}(\vec{r}, \Omega)$ from $\vec{\mu}_{xy}$ parallel to the interfaces. That is $P(\vec{r}, \Omega) = P_\infty + \Delta P_z(\vec{r}, \Omega) + \Delta P_{xy}(\vec{r}, \Omega)$ with

$$\Delta P_z(\vec{r}, \Omega) = \frac{\pi^2 \mu_0 \omega^3}{k_1^2} \text{Re} \int_0^\infty dk_{xy} \frac{k_{xy}}{k_{1z}} \exp(2ik_{1z}z) k_{xy}^2 r_{1m}^p |\vec{\mu}_z|^2 \quad \text{and} \quad (2.24)$$

$$\Delta P_{xy}(\vec{r}, \Omega) = \frac{\pi^2 \mu_0 \omega^3}{2k_1^2} \text{Re} \int_0^\infty dk_{xy} \frac{k_{xy}}{k_{1z}} \exp(2ik_{1z}z) (k_1^2 r_{1m}^s - k_{1z}^2 r_{1m}^p) |\vec{\mu}_{xy}|^2. \quad (2.25)$$

Figure 2.9 shows results for a horizontal and a vertical dipole near an air–glass and a water–glass interface, respectively. The dissipated power is significantly enhanced if the dipole–interface distance is less

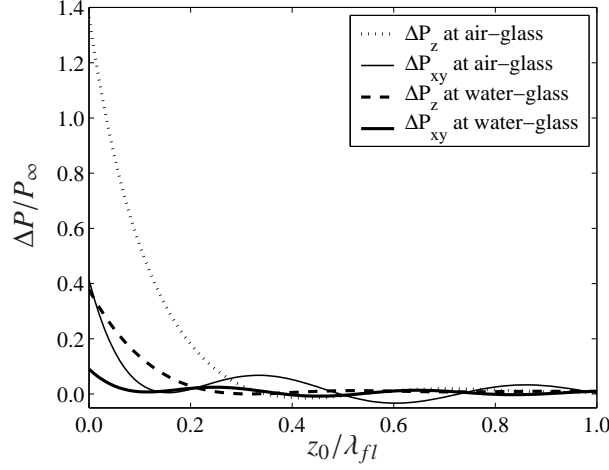


Figure 2.9: Enhanced power dissipated by a vertical and a horizontal dipole near an interface.

than about $\lambda_{fl}/5$. For the horizontal dipole, the power enhancement shows an oscillation caused by the interferences between the direct and the reflected field in medium 1 (air, water). For the vertical dipole, the enhancement simply decreases with increasing distance (approximately exponentially). In addition, the enhancement is significantly stronger for the vertical dipole, which reflects the stronger coupling of the p -polarized near field in medium 1 to waves propagating at super-critical angles in the denser medium 2 (glass).

Now, the interaction of a fluorophore with planar interfaces can be calculated. Taking into account that $|\vec{\mu}_z| = |\vec{\mu}| \cos \Theta$ and $|\vec{\mu}_{xy}| = |\vec{\mu}| \sin \Theta$, the radiative enhancement factor $\gamma(\vec{r}, \Omega)$ is given by $1 + \Delta P_z(\vec{r}, \Omega)/P_\infty + \Delta P_{xy}(\vec{r}, \Omega)/P_\infty$.

$$\gamma(\vec{r}, \Omega) = 1 + \frac{3}{4k_1^3} \text{Re} \int_0^\infty dk_{xy} \frac{k_{xy}}{k_{1z}} \exp(2ik_{1z}z) \left\{ 2k_{xy}^2 r_{1m}^p \cos^2 \Theta + (k_1^2 r_{1m}^s - k_{1z}^2 r_{1m}^p) \sin^2 \Theta \right\} \quad (2.26)$$

In the limit $z \rightarrow \infty$, the integral vanishes which corresponds to the homogeneous case (a).

As shown in the Jablonski diagram (figure 2.4), the singlet state S_1 decays via three decay channels. The fluorescence decay is attributed to Γ_{em} and the other decay channels are attributed to Γ_{nr} , namely non-radiative decay and intersystem crossing. The fluorescence decay rate is now $\gamma_{fl}(\vec{r}, \Omega)/\tau_{fl}$, which reduces the singlet state lifetime to

$$\tau'_{S_1} = \left(\frac{\gamma_{fl}}{\tau_{fl}} + \frac{1}{\tau_{nr}} + \frac{1}{\tau_{isc}} \right)^{-1} = \frac{\tau_{S_1}}{\gamma_{fl} q_{fl} + 1 - q_{fl}}. \quad (2.27)$$

The quantum yield is increased to

$$q'_{fl} = \frac{\tau'_{S_1}}{\tau_{fl}} = \frac{\gamma_{fl} q_{fl}}{\gamma_{fl} q_{fl} + 1 - q_{fl}} \quad (2.28)$$

and the probability of intersystem crossing is decreased to

$$q'_{isc} = \frac{q_{isc}}{\gamma_{fl} q_{fl} + 1 - q_{fl}}. \quad (2.29)$$

In addition, the triplet decay rate is increased. Assuming the radiative decay (phosphorescence) with probability q_{ph} , the triplet state lifetime reduces to

$$\tau'_{T_1} = \frac{\tau_{T_1}}{\gamma_{ph} q_{ph} + 1 - q_{ph}}. \quad (2.30)$$

In summary, the vicinity of a planar structure affects the rate of the electromagnetic emissions of the fluorophore. This influence manifests itself as a modification of the excited state lifetimes as well as the fluorescence quantum yield. The emission rate, e.g. the rate of the fluorescence transition as given by equation (2.5), is in the general case given by

$$R_{fl}(\vec{r}, \Omega, t) = \gamma_{fl}(\vec{r}, \Omega) \frac{q_{fl}}{\tau_{S_1}} P'_{S_1}(t). \quad (2.31)$$

We should keep in mind that $R_{fl}(\vec{r}, \Omega, t)$ is the radiation rate into different channels. This radiation is either transmitted to the far field in medium 1 or m , coupled to a wave-guide mode or surface plasmon, or absorbed in the structure. For instance, if the fluorophore approaches a metal, its emission rate will significantly increase as well as q'_{fl} does. But this increased emission is counter-balanced by an increased energy dissipation, i.e. due to electron-hole excitations in the metal. For a fluorophore–metal distance ≤ 20 nm, the energy loss becomes so dominant that the observable fluorescence intensity is effectively lower than that far from the metal (c.f. also [47, 48]).

2.5 Emitted dipole field

In this section, the far field emission is calculated in view of describing the collection efficiency by the microscope objective. For this purpose, the radiated far field is described as a plane wave spectrum according to equation (2.12). Analogous to (2.16), (2.21) and (2.22), in medium 1 it is given by the dipole field superimposed by the reflected field, both propagating towards the collection optics.

$$\begin{aligned} \vec{E}_k^{\uparrow\uparrow} &= i\pi\mu_0 \frac{\omega^2}{k_1^2} \frac{\exp(-i\vec{k}_1 \cdot \vec{r}_0)}{k_{1z}} \\ &\times \left\{ \left(\vec{q} \cdot \vec{\mu} + (\vec{p} \cdot \vec{\mu}) r_{1m}^p \exp(2ik_{1z}z_0) \right) \vec{q} + (\vec{s} \cdot \vec{\mu}) \left(1 + r_{1m}^s \exp(2ik_{1z}z_0) \right) \vec{s} \right\} \end{aligned} \quad (2.32)$$

The far field spectrum in medium m is given by the transmitted downward propagating field. The transmission coefficients through the structure are given by $t_{1m} = t_{m1} k_{1z} / k_{mz}$ and the field spectrum is

$$\vec{E}_k^{\downarrow\downarrow} = i\pi\mu_0 \frac{\omega^2}{k_1^2} \frac{\exp(-i\vec{k}_1 \cdot \vec{r}_0)}{k_{mz}} \left((\vec{p} \cdot \vec{\mu}) t_{m1}^p \vec{\sigma} + (\vec{s} \cdot \vec{\mu}) t_{m1}^s \vec{s} \right) \exp(-ik_{mz}d) \quad (2.33)$$

where d is the total thickness of all layers and $\vec{\sigma} = k_{xy}\vec{e}_z + k_{mz}\vec{e}_{xy}$.

Figure 2.10 shows the far field spectrum emitted by a horizontal dipole along the x -axis. In case (a), i.e. no interface, the dipole radiates homogeneously around its axis (thin lines outline the xz and yz cross-sections). In case (b), i.e. on a glass–water interface, the dipole radiates mainly into two lobes in the

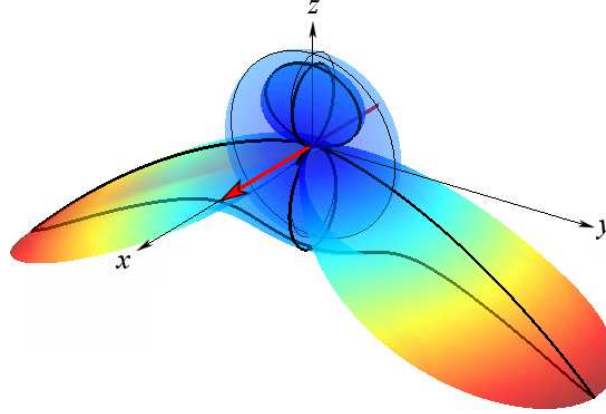


Figure 2.10: Radiated angular power density $\propto |\vec{E}_k|^2$ for a horizontal dipole along the x -axis (arrow). The dipole is located at the glass–water interface.

yz -plane (thick lines). The maximum radiation indicates the critical angle for total internal reflection at the interface. The total radiated power increases by less than 10%, but more than 69% of the radiation is directed into the glass. Compared with case (a), the radiated power is substantially increased in the glass whereas it is decreased by about 33% in the water.

The emitted field $\vec{E}_{fl}(\vec{r}, \Omega)$ can be calculated from these far field spectra of a dipole at position \vec{r} with orientation Ω . This representation as a \vec{k} spectrum of the p - and s -polarized components is required anyhow for calculating the propagation to the pinhole in section 2.6. We would like to emphasize that it is important to consider the fluorophore as a *fixed power* dipole, whose power is imposed by the current emission rate. Therefore, we could require $P_{fl}(\vec{r}, \Omega) = R_{fl}(\vec{r}, \Omega, t)\hbar\omega$ for normalizing the dipole moment $|\vec{\mu}(\vec{r}, \Omega)|$ right here. Instead, we include this normalization in the detection efficiency when dividing the detected power by $P_{fl}(\vec{r}, \Omega)$ for obtaining the detection efficiency $Q_{fl}(\vec{r}, \Omega)$.

2.6 Detection efficiency

The detection efficiency can be considered as the complementary part of the excitation field. In the following, it is defined by the probability of receiving a photon in the detection aperture (pinhole) if this photon was emitted at position \vec{r} by a fluorophore with dipole orientation Ω . Figure 2.11 summarizes the calculation of the detection efficiency $Q_{fl}(\vec{r}, \Omega)$, which is accomplished by calculating the ratio $q_d T_{fl} P_p(\vec{r}, \Omega) / P_{fl}(\vec{r}, \Omega)$ with P_p the power transmitted through the pinhole. q_d is the quantum yield of the detector and T_{fl} the transmission efficiency of the filter set, both at the fluorescence wavelength λ_{fl} .

$P_p(\vec{r}, \Omega)$ is obtained by integrating the intensity falling on the pinhole. This requires calculating the electromagnetic field in the pinhole plane \mathbb{P} . Using the superscripts p and s for the p - and s -polarized components, the calculation of the field in the pinhole can be subdivided into three steps:

Step 1 The fluorescence emission is collected by the high NA objective.

The emitted field \vec{E}_k in the direction of the wavevector \vec{k} is calculated based on equations (2.32) or (2.33). The field \vec{E}_o collected by the objective is essentially \vec{E}_k , but the phase is referenced to the object focus \mathbf{F}_o . Reversing the calculation of the excitation field in [3] (annexed) leads to the field \vec{E}_a

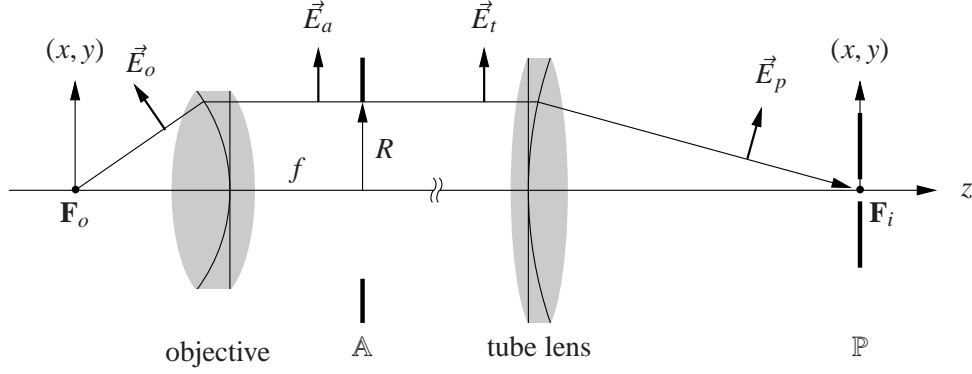


Figure 2.11: Calculation of the electromagnetic field in the pinhole plane \mathbb{P} .

in the objective aperture \mathbb{A} (the reciprocity in optics was recently reviewed by Potton [49]). Considering medium n_m as the immersion medium allows us to identify $n_t = n_m$ and $k_t = k_m$. Recall that f and R are the focal length and the aperture radius of the objective with numerical aperture NA. Then, equations (1,8) in [3] read as

$$x, y = \frac{R}{k_0 \text{NA}} k_{x,y} \quad \text{and} \quad d\vec{k}_{xy} = \left(\frac{k_0 \text{NA}}{R} \right)^2 dx dy. \quad (2.34)$$

The electric field arriving at the aperture \mathbb{A} is then

$$E_a^{p,s}(x, y) = \frac{k_0 \text{NA}}{R} t_{ta}^{p,s} E_o^{p,s}(k_x, k_y) \quad (2.35)$$

The transmission coefficients t_{at} given by equations (21,22) in [3] were calculated from the aperture \mathbb{A} to the immersion. For the reverse direction, they are given by $t_{ta} = n_t t_{at}$ (\mathbb{A} is in air).

Figure 2.12a shows the electric field $|\vec{E}_a|$ in the aperture \mathbb{A} of a 1.45 NA oil immersion objective observing a dipole in the focus at the coverslip–sample interface. For a x -oriented dipole (left), the field is relatively homogeneous at sub-critical angles ($\text{NA} < 1.33$). At super-critical angles, it exhibits a significant increase in particular perpendicular to the dipole axis, e.g. along the y -axis. Along the x -axis, the field vanishes right at the critical angle. The vertical dipole (right) emits a rotationally symmetric field (p -polarized), which is particularly strong at super-critical angles.

Step 2 The fluorescence emission is propagated to the tube lens.

Because the field distribution in \mathbb{A} can be described as paraxial and the propagation distance $z_p - z_a \gtrsim 120\text{mm}$, the Fresnel approximation for this free space propagation can be applied. In general, the Fresnel approximation is valid for

$$(z_p - z_a)^3 \gg \frac{\pi}{4\lambda} \max\left((x_a - x_p)^2 + (y_a - y_p)^2\right)^2. \quad (2.36)$$

This is a sufficient condition, which would demand a propagation distance $z_p - z_a \gtrsim 500\text{mm}$. However, if the main contribution of the field \vec{E}_t at point (x_p, y_p, z_p) comes from points (x_a, y_a, z_a) close to (x_a, y_a, z_p) , the Fresnel approximation is also valid for smaller propagation distances. This is achieved with the pseudo-paraxial Fresnel transformation for removing the wave front tilt [50] and an equivalent transform [51, 52] for reducing the wave front curvature.

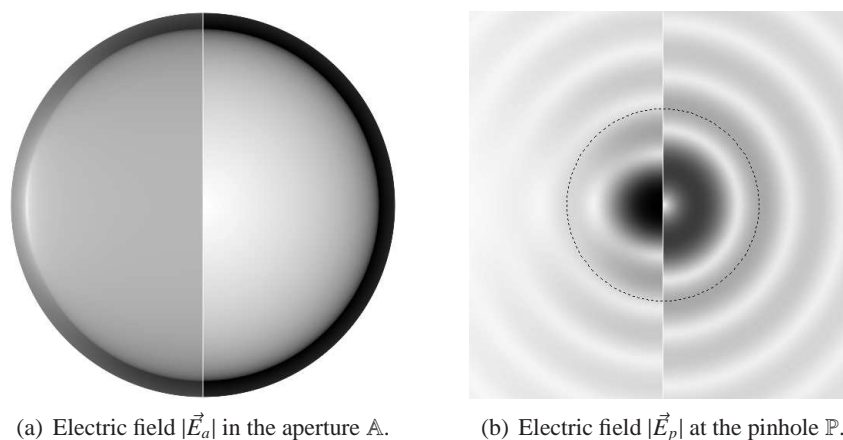


Figure 2.12: Electric fields in the aperture of a 1.45 NA oil immersion objective (a) and at the pinhole (b) for a dipole at the coverslip–sample interface. The circle in (b) indicates the $\varnothing 50\mu\text{m}$ pinhole. The left half-pictures show the field of the horizontal dipole. The field of the vertical dipole is shown in the right half-pictures.

Step 3 The fluorescence emission is focused onto the pinhole.

The field \vec{E}_p near the focus \mathbf{F}_i in the pinhole plane is calculated with the Debye diffraction integral following the method by Leutenegger et al. [3]. If the focusing angles are small, the Fraunhofer approximation may be used.

Figure 2.12b shows the electric field $|\vec{E}_p|$ at the pinhole \mathbb{P} . The image of the horizontal dipole resembles a deformed Airy pattern, whereas the field of the vertical dipole is strongest in a ring around the axis.

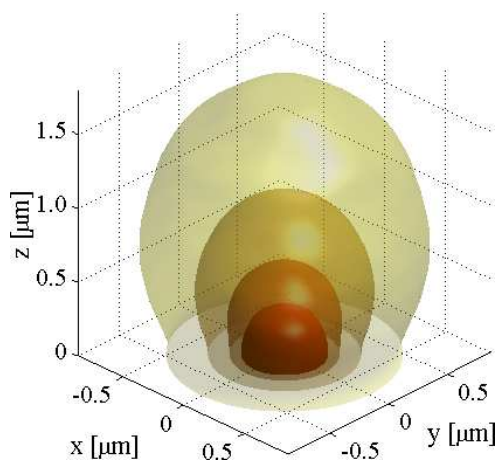


Figure 2.13: Detection efficiency of a 1.45 NA oil immersion objective focused on the cover glass–water interface. The iso-surfaces show $Q_{fl}(\vec{r}) = e^{-1\dots-4}Q_{fl}(0)$ in the sample.

Figure 2.13 shows the average detection efficiency for a 1.45 NA oil immersion objective observing randomly oriented fluorophores emitting at a wavelength $\lambda_{fl} = 525\text{nm}$ near the glass–sample interface. The projected pinhole diameter is $0.5\mu\text{m}$ on the interface, which results in a hemi ellipsoidal detection

volume of $0.7\mu\text{m}$ base diameter and $0.5\mu\text{m}$ axial extension. Assuming $q_d T_{fl} = 1$, the peak detection efficiency at the focus is about 27%, which is about 4–5 \times better than with a 1.20 NA water immersion objective collecting fluorescence emitted into the sample half-space (i.e. used by Lieto et al. [28]).

2.7 Fluorescence signal

In fluorescence fluctuation spectroscopy, the detected fluorescence signal is given as

$$I(t) = \iint Q_{fl}(\vec{r}, \Omega) c(\vec{r}, \Omega, t) R_{fl}(\vec{r}, \Omega, t) d\Omega d\vec{r} \quad (2.37)$$

where $c(\vec{r}, \Omega, t)$ is the sample concentration and orientation density given by the concentration $c(\vec{r}, t)$ at position \vec{r} times the probability $P(\Omega, t)$ of occupying the orientation Ω . $I(t)$ is the count rate of photon detections, which is equivalent to the number of detection events within a short time interval Δt in the photon trace $U(t)$ as shown in figure 2.1.

The observed count rate summarizes the spatio-temporal distribution and orientation of fluorophores, their emission rate and the detection efficiency. $I(t)$ forms the basis of every FFS experiment and the subsequent analysis principally evaluates its temporal evolution and/or its distribution. However, an analysis based on equation (2.37) is rather complex and cumbersome, in particular if the time-dependency needs to be taken into account as with FCS for instance. Fortunately, a number of simplifications apply for the majority of measurement cases. For instance, if the translational diffusion is much slower than the rotational diffusion and the lifetime τ_{S_1} of the excited state much longer than the mean rotation time τ_r , the orientation dependency as a whole can be evaluated a priori. The excitation rate is then given by equation (2.3) and (2.4) averaged over all orientations Ω .

$$\tau_{ex}^{-1}(\vec{r}, t) = \int_0^\pi d\Theta \int_{-\pi}^{+\pi} P(\Omega(\Theta, \varphi), t) \tau_{ex}^{-1}(\vec{r}, \Omega(\Theta, \varphi), t) d\varphi \quad (2.38)$$

Further assuming a homogeneous angular distribution $P(\Omega, t) = 1/4\pi$, the excitation rate is given by

$$\tau_{ex}^{-1}(\vec{r}, t) = \frac{1}{3} \left(\tau_{ex}^{-1}(\vec{r}, \Omega_z, t) + \tau_{ex}^{-1}(\vec{r}, \Omega_x, t) + \tau_{ex}^{-1}(\vec{r}, \Omega_y, t) \right) \quad (2.39)$$

where the terms are the excitation rates for z -, x - and y -oriented fluorophores. Of course, this is exactly the isotropic excitation rate described by equation (2.1). Because of $\tau_{S_1} \gg \tau_r$, the emission anisotropy is not correlated with the excitation anisotropy and the emission rate $R_{fl}(\vec{r}, t)$ can be calculated with equations (2.27) to (2.31) using the average enhancement factors $\gamma_{fl}(\vec{r})$ and $\gamma_{ph}(\vec{r})$, where

$$\gamma_{fl,ph}(\vec{r}) = \frac{1}{3} \left(\gamma_{fl,ph}(\vec{r}, \Omega_z) + \gamma_{fl,ph}(\vec{r}, \Omega_x) + \gamma_{fl,ph}(\vec{r}, \Omega_y) \right) . \quad (2.40)$$

Similarly, the average detection efficiency at \vec{r} is obtained by

$$Q_{fl}(\vec{r}) = \frac{1}{3} \left(Q_{fl}(\vec{r}, \Omega_z) + Q_{fl}(\vec{r}, \Omega_x) + Q_{fl}(\vec{r}, \Omega_y) \right) . \quad (2.41)$$

Therefore, equation (2.37) simplifies to the common isotropic expression

$$I(t) = \int Q_{fl}(\vec{r}) c(\vec{r}, t) R_{fl}(\vec{r}, t) dV . \quad (2.42)$$

This isotropic description also applies for measuring a large number of randomly oriented fluorophores, such that the anisotropic fluorescence response is averaged out.

Note that the time-averaged response $Q_{fl}(\vec{r})R_{fl}(\vec{r})$ is the brightness profile $B(\vec{r})$, that is the detected count rate from a fluorophore at position \vec{r} . Neglecting fluorescence saturation, the brightness profile is commonly approximated by $B(\vec{r}) \approx \sigma_{ex}q_{fl}Q_{fl}(\vec{r})I_{ex}(\vec{r})/\hbar\omega_{ex}$ and represents the point spread function (PSF) of the measurement system, also called molecule detection efficiency (MDE). Calculation examples are given in the following chapter.

Chapter 3

Experiments

3.1 Near field excitation on structured surfaces

Scanning near field optical microscope (SNOM) is a well-known near field imaging technique. SNOM probes are typically metal-coated conical glass fibers ending with or without an aperture at the fiber apex. Apertureless probes are sensing through plasmonic interaction between the sample and the fiber core. They are typically used as near field sensors, whose resolution beyond the diffraction limit is due to the sharp metal tip at the apex (in the order of 50nm to 100nm). On the other hand, SNOM probes with a nano-aperture have a relatively flat uncoated apex, which exposes the fiber end directly within the near field of the interrogated sample. The light transmission is sufficiently high for applying these probes as efficient near field light sensors.

Motivated by the search for ever smaller sampling volumes (compare figure 1.1), near field illumination concepts were recently adopted for FFS as the NA of conventional optics cannot be increased substantially beyond 1.45 with glass substrates or 1.65 with sapphire substrates. For instance, Levene et al. [25] were among the first using near field excitation for FCS by exploiting the confinement of the sampling volume inside a sub-wavelength sized aperture through a supported metal film. The aperture diameter was about an order of magnitude smaller than the wavelength. Epi-illumination of such an aperture creates a strongly evanescent field inside the aperture, hence a very confined excitation volume at the entry. In addition, fluorescence detection is efficient at the very bottom of the aperture and in particular at the aperture edge. The sampling volume was showed to be $\ll 1\lambda$ allowing micromolar sample concentrations.

Using FCS, we characterized the light confinement obtained with nano-structured surfaces (c.f. Leutenegger et al. [7] in the annex). Adopting the principle of an aperture SNOM probe, we calculated the light transmission through a metallic aperture as well as the light distribution at its exit. Figure 3.1 shows the light distribution through the back-illuminated aperture. The excitation wavelength λ_{ex} was 633nm and the laser beam was focused with an effective NA of about 0.6. Figure 3.1a sketches the electric field through the aperture ($\varnothing = 150\text{nm}$, 150nm thick gold layer on glass substrate). The incident field is x -polarized and propagates through the aperture mainly via surface plasmons on the aperture wall at the left and right. These surface plasmons are efficiently excited because the local polarization is perpendicular to the aperture wall (gold–water interface). At the aperture exit ($z = 150\text{nm}$), the field is strongest within two crescent-shaped volumes near the aperture rim as shown in figure 3.1b. The plasmonic fine structure extends up to about 50nm above the aperture. It is then enclosed by an ellipsoid-like volume with x -, y - and z -half-axes of about 140nm, 100nm and 80nm, respectively.

Figure 3.2 shows a first array of nano-apertures in a 150nm thick gold film. In this array, the apertures had a diameter of 420nm and were aligned on a square grid with 2.5 μm lattice. This figure exemplifies irregularities of the aperture rims of $\pm 20\text{nm}$. Improved fabrication procedures led to irregularities of less than $\pm 10\text{nm}$. The following measurements were performed on these improved arrays.

FCS measurements were performed using an aqueous Cy5 solution of 12nM or 30nM fluorophore

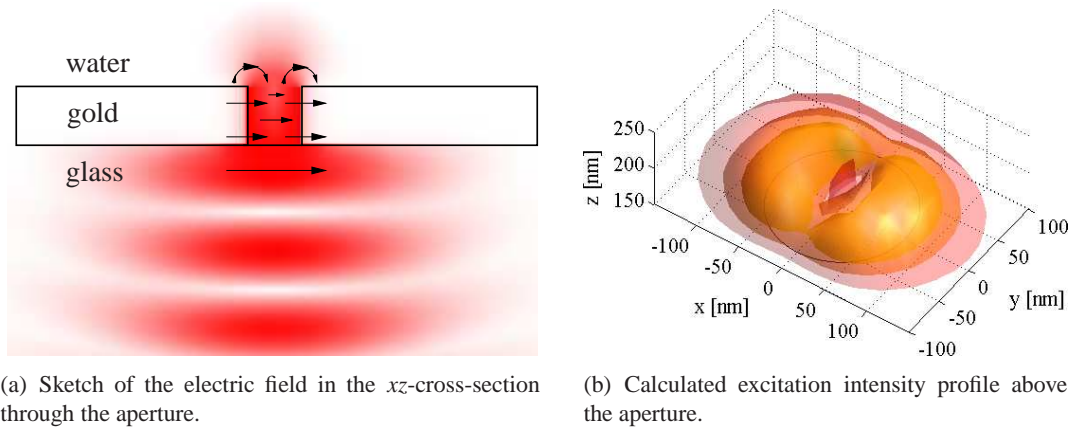


Figure 3.1: Light distribution inside and above a nano-aperture in a gold film.

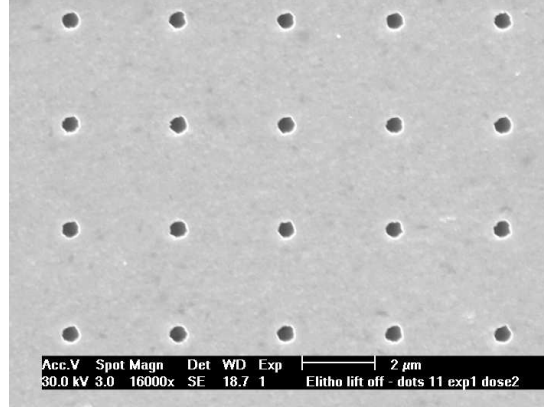


Figure 3.2: Array of $\varnothing 420\text{nm}$ apertures in a 150nm thick gold film.

concentration. This sample was filled in a $90\mu\text{m}$ gap between the structured gold layer and a glass coverslip. The induced fluorescence was collected through the coverslip with a 1.20 NA water immersion objective (C-Apochromat $40\times 1.20\text{w}$, Carl Zeiss) and imaged on a multimode fiber with $38\mu\text{m}$, $50\mu\text{m}$ or $100\mu\text{m}$ core diameter. A single photon counting module (SPCM-AQR-14-FC, PerkinElmer) detected the photon sequence. This photon trace was then correlated with a hardware correlator (Flex99OEM-12C, Correlator.com) and the correlation curve $G(\tau)$ was analyzed using a non-linear least squares fit on the model curve.

For FCS, the normalized auto-correlation $G(\tau)$ of the photon trace $I(t)$ given by

$$G(\tau) = \frac{\langle I(t)I(t+\tau) \rangle}{\langle I(t) \rangle \langle I(t+\tau) \rangle} = (T-\tau) \frac{\int_0^{T-\tau} I(t)I(t+\tau) dt}{\int_0^{T-\tau} I(t) dt \int_{\tau}^T I(t) dt} \quad (3.1)$$

is compared against a model curve calculated with the brightness profile $B(\vec{r})$ and the diffusion properties of the sample. For a standard three-dimensional Gaussian $B(\vec{r})$ and unconstrained diffusion, an analytical

model curve can be derived [5, 20, 53, 54, 55].

$$G(\tau) = G_\infty + \left(1 - \frac{I_B}{\langle I \rangle}\right)^2 \frac{\gamma}{N} \left\{ \left(1 + \frac{\tau}{\tau_d}\right)^{-1} \left(1 + \frac{\tau}{K^2 \tau_d}\right)^{-1/2} + \frac{P_t}{1 - P_t} \exp\left(-\frac{\tau}{\tau_t}\right) \right\} \quad (3.2)$$

where $G_\infty \approx 1$ is the correlation amplitude in the long lag time limit $\tau \rightarrow \infty$, N is the average number of molecules in the sampling volume, τ_d is the lateral diffusion time, K is the ratio of axial over lateral extension of the sampling volume, P_t is the triplet state population and τ_t is the correlation time of this triplet state population. I_B is the background count rate and $\langle I \rangle$ is the mean count rate (fluorescence intensity and background). γ was assumed to be 1/2 because of the half-ellipsoid excitation volume [8]. It is evident that the effective brightness profile is not 3D Gaussian and the diffusion is at least partially constrained near the aperture. Despite of the crude approximations, this simple model equation provided reasonable fits as figure 3.3 shows. In free liquid and for the 490nm aperture, equation (3.2) fits well with

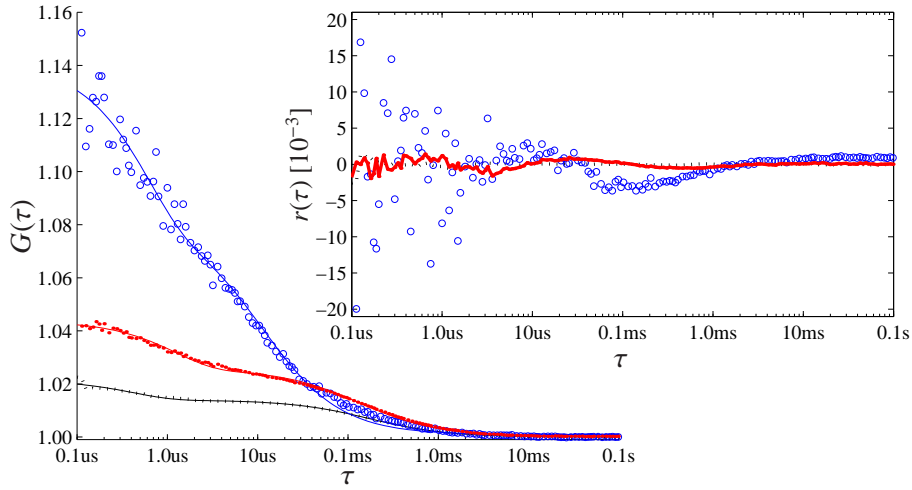


Figure 3.3: Auto-correlations and fits $G(\tau)$ versus lag time τ for aperture diameters of 125nm (blue circles), 490nm (red points) and for free liquid (black dotted) measured with a Cy5 concentration of 30nM. Inset: Fit residuals $r(\tau) = G_{fit}/G(\tau) - 1$.

Reprinted from Leutenegger et al. [7] with permission by Optics Express.

low residuals. Deviations were mainly observed for $\varnothing \lesssim 200$ nm because the volume inside the aperture becomes comparable to the volume above the aperture. For the 125nm aperture for instance, the fit shows significant residuals and even a bias at large lag times. Nevertheless, the extracted diffusion time τ_d is a good approximation because it accounts only for the diffusion in the xy -plane. In addition, the number of molecules N depends mainly on the correlation amplitude $G(0)$ and the triplet probability and is only slightly affected by the choice of the diffusion model.

It is worth noting that the trans–cis isomerization process of the Cy5 molecule was fitted with the triplet state parameters.¹ Widengren and Schwille [54] studied this process with FCS and found the triplet state population neglectable for excitation intensities $\lesssim 30$ kW/cm², which is also the case here. The isomerization process dominated the shape of the correlation curve for $\tau \lesssim 10\mu$ s, resulting in an apparent triplet state population of $\approx 40\%$.

¹ The isomerization as well as the triplet formation are both described by the same model curve, which easily confuses the attribution of a feature in the measured correlation curve to a particular molecular process.

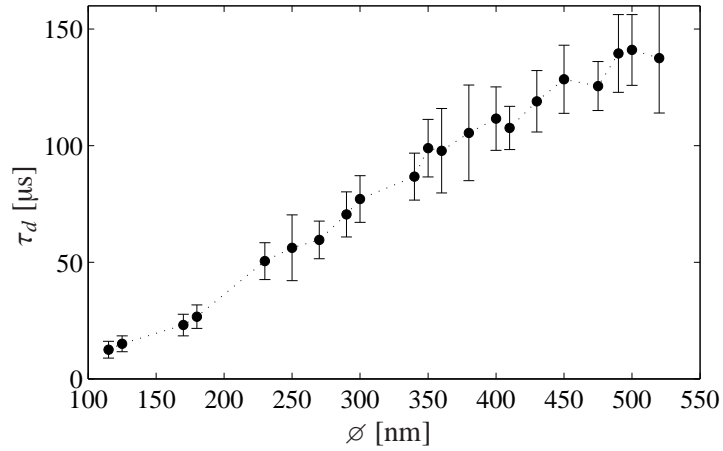


Figure 3.4: Diffusion time assuming a three-dimensional Gaussian PSF.

Figure 3.4 shows the lateral diffusion time τ_d measured on apertures with various diameters. The diffusion time was expected to scale with the aperture area, that is $\tau_d \propto \phi^2$, up to an upper bound of $\approx 250\mu\text{s}$, which is set by the diameter of the focal spot ($\approx 700\text{nm}$). A nearly linear increase was observed for aperture diameters from 125nm to 520nm. Calculations of the excitation volumes showed that the sampling volume V should scale with at least $\tau_d^{3/2}$ because the axial extension of the volume decreases faster than $\sqrt{\phi}$. This leads to a sampling volume of $\approx 30\text{al}$ above 150nm apertures, this is a $16\times$ confinement of the sampling volume compared to the unconstrained confocal sampling volume.

We measured further the average number N of fluorophores in the sampling volume for a Cy5 concentration of 12nM and 30nM. Even though N is a direct measure of V , the measured values scattered in a much broader range due to two major reasons:

1. N is more sensitive to variations in the excitation field profile than τ_d . In fact, without knowledge of the excitation rate and the detection efficiency in the entire sampling volume, N cannot be normalized accurately. The excitation rate was expected to be linearly proportional to the calculated excitation intensity, which was far from the saturation level of the fluorophore. A full theoretical calculation would take account of the detection efficiency and the fluorescence process as well.
2. N is affected by the signal to background ratio (SBR) whereas τ_d is not. Unfortunately, the gold layer added a significant background because of electron-hole pair formation and luminescent recombination. In addition, fabrication irregularities led to randomly distributed gold nano-particles inside the apertures and on the rims. This gold "dust" was particularly luminescent, such that the background rate varied easily an order of magnitude between the different apertures.

Despite these issues, N showed a $6\times$ better confined sampling volume than without the aperture. In summary, back-illumination of apertures with sub-wavelength diameter results in a confined near field above the aperture. This near field excitation is suitable for FFS but suffers from background luminescence depending upon the choice of the excitation wavelength and the metal. Trans-illumination provides an improved sample mobility compared to an epi-illumination scheme, where the diffusion of the sample is much more affected due to the vicinity of surfaces all around the molecules.

The background issue can be better mastered with silver and in particular with aluminum films (Rigneault et al. [30]). However, these metals are not inert when in contact with water, that is corrosion may become a limiting factor. Ultimately, the aperture could be sealed with a dielectric, i.e. filled with glass, which

would completely suppress sample diffusion inside the aperture. Such a sealing would further increase the intensity transmitted through the aperture and would provide a tool for observing the activity of immobilized enzymes for instance.

3.2 Dual-color total internal reflection fluorescence fluctuation spectroscopy

As outlined above, near field excitation with nanoholes provides confined, individually addressable excitation volumes suitable for FFS. These small volumes well below the far field diffraction limit are a matter of choice for investigating samples at micromolar biomolecule concentrations. However, the fabrication and handling needs more improvements before becoming a versatile platform for biological experiments. Nevertheless, the demand for smaller sampling volumes motivated by applications demanding higher concentration persists. Therefore, we investigated a different approach for achieving small sampling volumes with comparably simple sample preparation. Motivated by promising experiments with a novel total internal reflection FCS setup by Hassler et al. [22], a next generation TIR-FCS instrument for dual-color investigations was developed and characterized (c.f. Leutenegger et al. [4] in the annex).

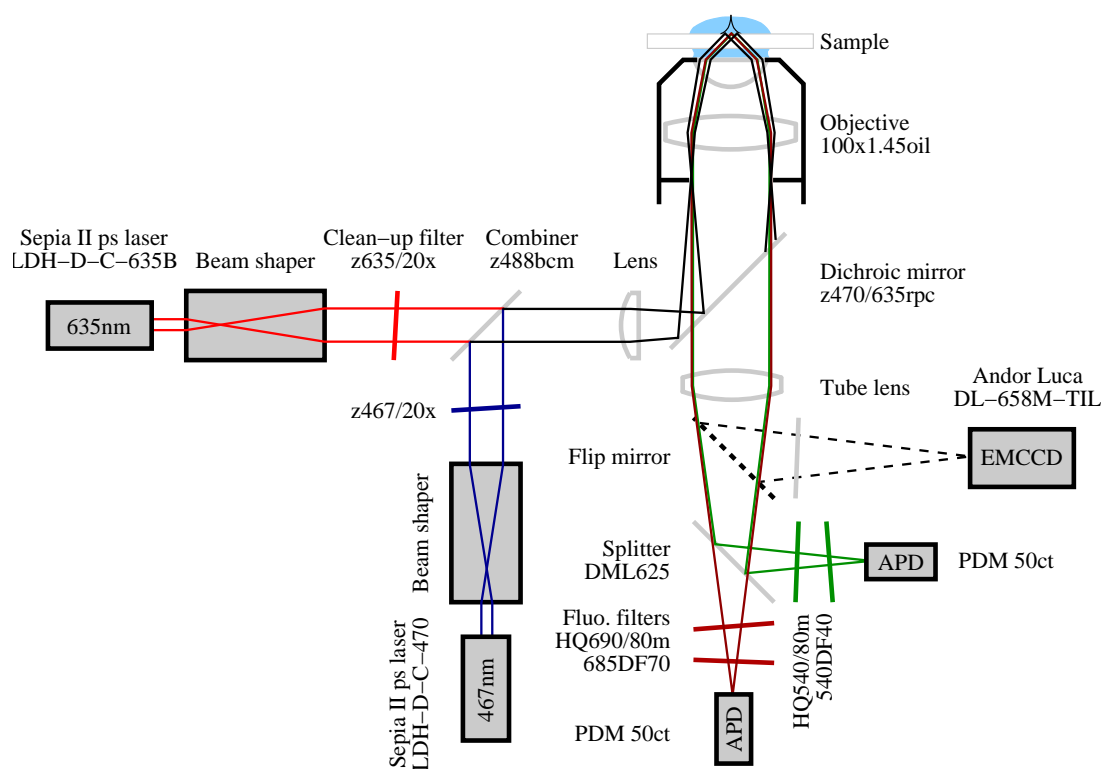


Figure 3.5: Current dual-color TIR-FFS and imaging platform.

Figure 3.5 outlines the current state of this next generation instrument. It is now the platform for dual-color FFS measurements in the evanescent field created by TIR at the coverslip-sample interface. It provides TIR fluorescence microscopy and dual-color confocal FFS measurements as well. Two ps diode lasers (Sepia II PDL 828 system with LDH-D-C-470 and LDH-D-C-635B laser heads, PicoQuant) provide linearly polarized beams with 635nm and 467nm center wavelengths, respectively. The laser powers are controlled by neutral density filters in addition to the control setting of the laser driver. The

beams are passed through polarization maintaining fibers for cleaning up the lateral beam profile. After collimation to an e^{-2} diameter of $\lesssim 2\text{mm}$ (TIRF) or $\approx 10\text{mm}$ (confocal), they are aligned coaxially to the microscope objective using two beam steerers. Laser-line clean-up filters (z467/20x and z635/20x, Chroma) ensure well-defined excitation spectra. A dichroic mirror (z488bcm, Chroma) combines the beams and an achromatic lens ($f = 130\text{mm}$) focuses them into the back-focal plane (BFP) of the high NA oil immersion objective (α -Plan-Fluar 100×1.45 , Carl Zeiss), which results in circular areas with e^{-2} diameters of $\approx 16\mu\text{m}$ (blue) and $\approx 20\mu\text{m}$ (red) at the coverslip–sample interface. In the BFP, a lateral offset of the beam foci of $\approx 2.3\text{mm}$ results in a super-critical angle illumination, i.e. in an evanescent field excitation as outlined in figure 3.6. The sample is mounted on a $150\mu\text{m}$ thick glass coverslip, which is

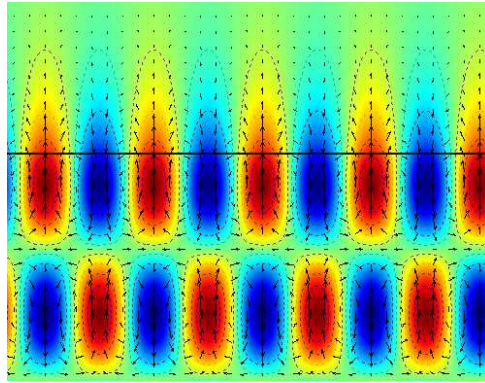


Figure 3.6: Excitation field created with a p-polarized plane wave incident at a super-critical angle. The incident wave is reflected back into the glass. The black line outlines the glass–water interface. In the water above the interface, an evanescent rotating field is induced.

positioned with a xyz -translation stage (ULTRAlign 561D with μ Drive Controller ESA-C, Newport). In this epi-illumination setup, the fluorescent light is collected with the same high NA objective and focused directly onto the active areas of $\varnothing 50\mu\text{m}$ of the single photon detectors (PDM 50ct, MPD). A dichroic mirror (DML625, Omega) splits the green and red fluorescence light, whereas the combination of the main dichroic mirror (z470/635rpc, Chroma) and band-pass filters (Chroma HQ540/80m and Omega 520DF40; Chroma HQ690/80m and Omega 685DF70) block the back-reflected laser light by more than 10 orders of magnitude. The fluorescence signals are recorded with a PicoHarp 300 system (PicoQuant) and simultaneously correlated with a hardware correlator (Flex02-08D, Correlator.com). For TIRF imaging, a flip mirror redirects the fluorescence light on a sensitive electron-multiplying CCD camera (Luca DL-658M-TIL, Andor).

The focusing lens and the main dichroic mirror are laterally moveable for positioning the beam foci off-axis in the BFP of the objective. This allows an independent adjustment of the excitation angle while keeping the beams focused on the BFP of the objective. A confocal configuration is achieved by removing the focusing lens and by centering the collimated beams in the BFP. Due to the chromatic length aberration of the TIRF objective, a common pinhole cannot be inserted.² Therefore, the confocal configuration as well as excitation-independent detection paths is required for aligning the single photon detectors mutually.

A first concept of this next generation instrument was equipped with two cw lasers (c.f. Leuteneg-

² The vendor specifies a chromatic focus drift of 650nm from $\lambda = 540\text{nm}$ to 690nm , which is magnified to 6.5mm in the pinhole plane.

ger et al. [4] in the annex). It was tested for single molecule coincidence analysis. A synthetic binding assay of three fluorescent samples was used for this first performance check. Dilute solutions of free Cy5 and Rhodamine Green (RhG) were used as singly labeled reference samples. A mixture of these two solutions formed then the non-binding two-color reference. A 40 base pair double-stranded DNA labeled with AlexaFluor488 and Cy5 (Carl Zeiss cross-correlation standard) served as binding two-color reference. A NaCl/EDTA/TRIS pH 8.0 buffer prevented denaturation of the DNA sample upon dilution of all samples to about 10nM concentration. The binding reference was then mixed in parts with the non-binding reference. These mixtures were measured and analyzed with two-color global FCS (2CG-FCS, Eggeling et al. [10]) and two-dimensional fluorescence intensity distribution analysis (2D-FIDA, Kask et al. [56]). The FCS analysis was based on the model equation for TIR-FCS recently derived by Hassler et al. [8, 22] and model equations for cross-correlation analysis [57, 10]. The 2D-FIDA analysis was based on the standard confocal analysis with parameters adapted to match the evanescent brightness profile.

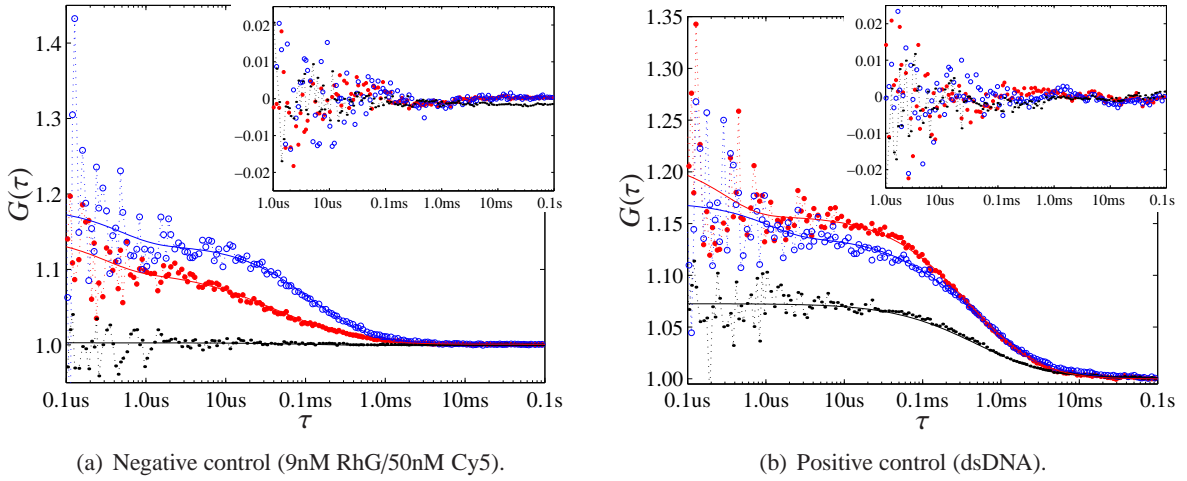


Figure 3.7: Auto- and cross-correlations and fits on the model curves. Circles: green autocorrelation. Bold points: red autocorrelation. Dots: green-red cross-correlation. Inset: fit residuals $G_{fit}/G(\tau) - 1$.

Reprinted from Leutenegger et al. [4] with permission by Journal of Biomedical Optics.

Figure 3.7 shows auto- and cross-correlation curves for (a) the non-binding reference and (b) the binding reference, respectively, both measured during 20s. Because the total count rates were only about 50kHz to 100kHz in each channel, the signal to noise ratio (SNR) was low in particular at short lag times $\tau \lesssim 5\mu$ s. The fit residuals clearly show the resulting scattering of the measured correlation curves. However, this low SNR mainly affected the estimation of the triplet parameters, which were not critical for obtaining the fraction of bound molecules accurately.

For free diffusion, the following model equation was used

$$G_{mn}(\tau) = G_{mn\infty} + \gamma_{mn} \left(1 - \frac{B_m}{I_m}\right) \left(1 - \frac{B_n}{I_n}\right) \frac{\sum Q_{mi} Q_{ni} N_i D_{mni}(\tau)}{\sum Q_{mi} N_i \cdot \sum Q_{ni} N_i} + G_{mnt} \exp\left(-\frac{\tau}{\tau_{mnt}}\right). \quad (3.3)$$

Here, indices m and n represent the green and red detection channels; hence G_{gg} and G_{rr} are the auto-correlations of the signals in the green and red detection channels, respectively, and G_{gr} the cross-correlation of both signals. The index i represents the diffusing species: g for RhG, r for Cy5 and c for the dsDNA. B is the measured background count rate and I the total count rate. Q_{mi} is the count rate per molecule (CPM) in channel m of species i . N_i are the number of molecules in the effective sampling volume. G_{mnt} and τ_{mnt} are the triplet amplitudes and the triplet correlation times respectively.

The first term $G_{m\infty} \approx 1$ is the offset at infinite lag time τ . The shape factor γ_{mn} of the observation volume was assumed to be $1/2$ for all correlations channels. It turned out later that it should be rather $1/4$ as calculated below. However, the following relative concentration measurements were not affected by this change in the shape factors. The next two terms correct the correlation amplitudes for the signal to background ratio (SBR) in each detection channel. The fraction normalizes the correlated intensity fluctuation with the product of the background-free fluorescence signals in the detection channels. $D_{mni}(\tau)$ describes the diffusion and is given by (c.f. Hassler et al. [8])

$$D_{mni}(\tau) = \left(1 + \frac{\tau}{\tau_{ixy}}\right)^{-1} \left\{ \sqrt{\frac{\tau}{\pi\tau_{iz}}} + \left(1 - \frac{\tau}{2\tau_{iz}}\right) \operatorname{erfcx}\left(\sqrt{\frac{\tau}{4\tau_{iz}}}\right) \right\} \quad (3.4)$$

where τ_{iz} and τ_{ixy} are the axial and lateral diffusion times of species i , respectively. The scaled complementary error function is given by $\operatorname{erfcx}(x) = \exp(x^2) \operatorname{erfc}(x)$. Finally, the last term accounts for the triplet blinking at short lag times.

In order to minimize the number of parameters, a perfect overlap of the sampling volumes was assumed, e.g. the diffusion times were assumed to be independent of the auto- and cross-correlations. The brightness of free fluorophores was assumed to be equal to the brightness of the fluorophores linked to the dsDNA. Moreover, the triplet blinking of all fluorophores were fit together for each correlation channel. A multidimensional least-squares Gauss-Newton algorithm was used to fit the experimental data to these model equations.

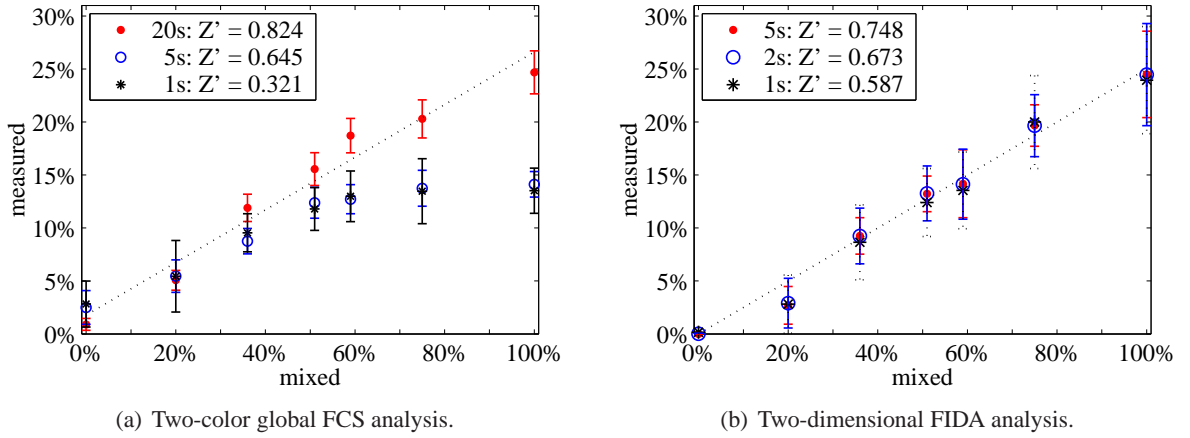


Figure 3.8: Coincidence analysis of a dual-color DNA sample (cross-correlation standard). The legends indicate the measurement times T and the statistical significance Z' of the coincidence analysis. A significance $Z' > 0.5$ is considered sufficient for high-throughput screening.

Reprinted from Leutenegger et al. [4] with permission by Journal of Biomedical Optics.

Figure 3.8 shows the measured fraction of bound sample versus the mixed fraction. The measured fraction of dsDNA scaled linearly with the mixed fraction from 1% (non-binding reference) to 25% (binding reference). The lower measured fraction was attributed to an excess of molecules with a single green label and to non-ideal overlap of the sampling volumes. Photo-bleaching of the red label during the two-color excitation possibly further enhanced the excess of green labels (Eggeling et al. [58]). To reduce its influence, the excitation intensities were lowered to $\leq 10 \mu\text{W}/\mu\text{m}^2$ such that the concentration of Cy5 was no longer diminished during the measurement. The overlap of the sampling volumes was estimated to about 60%.

As figure 3.8 shows, the accuracy of the FCS analysis benefited from increased measurement times whereas FIDA did not. For measurement times $T < 10$ s per run, the FCS analysis did not track mixed fractions $> 50\%$ but saturated at a value of about 13%. However, the statistical significance is still sufficient even for $T = 5$ s due to the lower variance compared with FIDA. In addition, 2CG-FCS provided a net improvement over 2D-FIDA for $T > 10$ s because FCS accounts not only for the intensity distribution but also for the different diffusion properties of the biomolecules.

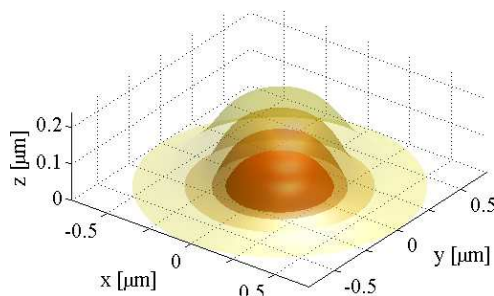


Figure 3.9: Brightness profile $B(\vec{r})$ for TIR-FFS with $\lambda_{ex} = 470$ nm, $\lambda_{fl} = 525$ nm and a projected pinhole of $\varnothing 500$ nm. The sampling volume has a diameter of 700nm and penetrates 120nm into the sample. Note that the z -axis is magnified twice.

Figure 3.9 shows the brightness profile $B(\vec{r})$ obtained with a 1.45 NA oil immersion objective when observing RhG near to the coverslip–sample interface. $B(\vec{r})$ was calculated with the detection efficiency $Q_{fl}(\vec{r})$ shown in section 2.6 and the excitation intensity is $I_{ex}(\vec{r}) = I_{ex} \exp(2ik_z z)$. The excitation source was focused at the edge of the aperture corresponding to $NA_{ex} = 1.42$, which resulted in a super-critical excitation angle and an evanescent field with $k_z = 2\pi \sqrt{n_s^2 - NA_{ex}^2} / \lambda_{ex}$ and the excitation wavelength is $\lambda_{ex} = 470$ nm. According to equations (4–6) by Wohland et al. [55], the sampling volume is $V = 17$ al and the effective sampling volume is $V_{eff} = 68$ al, e.g. the shape factor $\gamma = 1/3.95$ is close to the theoretical value of $1/4$. For an excitation wavelength $\lambda_{ex} = 635$ nm and a fluorescence wavelength of $\lambda_{fl} = 670$ nm, the corresponding values are $V = 24$ al, $V_{eff} = 103$ al and $\gamma = 1/4.27$.

The correlation amplitudes shown in figure 3.7 indicate a background corrected V_{eff} of 870al in the green channel and 170al in the red channel. The sampling volume for the red channel is in good agreement with the calculation. The slight discrepancy is presumably due to a lower excitation angle (i.e. 1.38–1.40 NA).³ In contrast, the measured V_{eff} in the green channel is 12 times larger than expected. Interestingly, the diffusion time of RhG was increased by only 15% compared to Cy5, which suggests a sampling volume of at most 200al. The large discrepancy is probably due to an increased RhG concentration near to the coverslip surface. In contrast to Cy5, transient sticking of RhG was observed even with oxygen plasma cleaned coverslips. In combination with a low sample concentration and negligible photo-bleaching, transiently bound RhG can considerably increase the average number of fluorophores in the sample volume. If the fluorophores are immobilized for seconds or longer, their emission increases the background count rate without leaving a significant trace in the correlation curve. Assuming this worst case, the background would need to be only $3\times$ stronger, which could be caused just by a single immobilized molecule.⁴

³ This is partially due to the chromatic aberration of the microscope objective, which becomes evident when setting the excitation angle close to the critical angle, where the blue beam was already evanescent whilst the red beam was still propagating.

⁴ Here, the fluorescence emission at the surface is taken twice the average emission in the effective sampling volume. These values correspond with binding experiments by Hassler et al. [8], see next footnote.

We conclude this section with an estimation of the achievable count rate in TIR-FFS. Estimating T_{fl} as product of 90% transmission through the dichroic mirror and 85% transmission through the emission filters and blocking 60% of the fluorescence emission (i.e. near IR emission), the filter set transmits only $T_{fl} \approx 30\%$ of the fluorescence emission. The detection efficiency q_d is specified to be 55% in the green range. Overall the peak detection efficiency is estimated at about 4.5%, which would lead to a peak count rate of about 4MHz when saturating RhG (c.f. figure 2.5) and assuming a quantum yield $q_{fl} = 50\%$ only ($> 94\%$ in methanol). However, when measuring Rhodamine derivates, the count rate never exceeded 2MHz, which suggests a quantum yield of 25% or less in water solution!⁵ With a quantum yield close to 100%, a single fluorophore could drive the detectors into saturation.

In summary, the novel dual-color TIR-FFS instrument provides an excellent platform for binding studies and enzyme measurements. We characterized the performance for dual-color binding studies with a synthetic binding assay. The measurements are in good agreement with theoretical predictions outlined in the previous chapter. Major deviations were assigned to chromatic aberrations of the objective and immobilization of RhG, respectively.

The current implementation is able to measure the fluorescence lifetime simultaneously with the correlation curves. Within a few minutes, it can be modified for single or dual-color TIRF microscopy and dual-color or polarization sensitive TIR-FFS or confocal FFS. The sampling volume achieved with TIR-FCS is about $2.5\times$ larger than with the nanoholes. But the simple, cost- and time-efficient sample handling is a major advantage of this TIR-FFS instrument. The background and photo-bleaching issues are

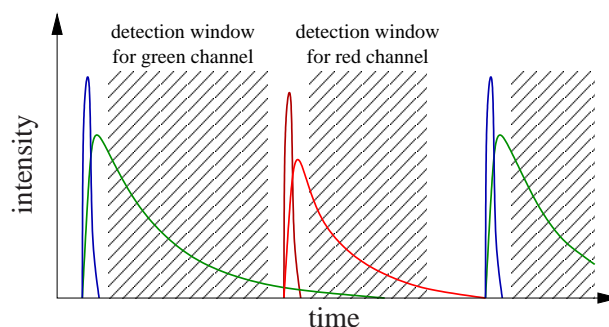


Figure 3.10: Pulsed interleaved excitation and time-resolved detection. The blue and red laser pulses are interleaved to avoid simultaneous exposure of the sample. In addition, corresponding detection windows select photon events within specific delays, such that the fluorescence signal is maximized whereas background events and detector noise are minimized.

now better mastered with pulsed interleaved excitation (PIE, c.f. Muller et al. [59]) and time-correlated single photon counting (TCSPC, c.f. Erdmann et al. [60]) shown in figure 3.10. TCSPC allows to mask Raman scattered light and "ps-delay" luminescence as well as detector noise by using a well-defined detection window, which allows optimizing the signal to noise ratio (SNR). PIE avoids exposing the fluorophores to several wavelengths simultaneously, which is in particular favorable for reducing photo-bleaching of red fluorophores. Despite of PIE, combined dual-color detection with a single detector is no option because of the chromatic length aberration of the objective. Unfortunately, the beam shaping with polarization maintaining single mode fibers introduced a significant astigmatism in the output beam.

⁵ See Hassler et al. [8]. The count rate per molecule was at maximum 1.8MHz including a shape factor of 3.4 due to the sampling volume. But transiently bound Rhodamine molecules were observed with a count rate of 500kHz to 800kHz. Additional confocal measurements confirmed an upper limit between 500kHz and 600kHz of the average count rate.

This issue was diminished by coupling the beam through an index-matched oil–coverslip arrangement at the fiber output. However, some astigmatism is still present, which deteriorates the confocal sampling volume in particular. Fortunately, TIR-FFS is less affected because the excitation volume is defined by the incidence angle alone. Though, the maximum excitation angle was slightly lowered because of the larger beam through the objective.

3.3 Imaging of G protein-coupled receptors in solid-supported planar lipid membranes

Membrane proteins are important in medicine and life science and play a fundamental role in cell signaling and trans-membrane transport. However, membrane proteins such as G protein-coupled receptors (GPCRs) require a lipid bilayer membrane for a correct folding, i.e. a vectorial incorporation for full receptor functioning is mandatory. The common approach of synthesis in a living cell followed by isolation and reincorporation into a model system is complicated, if not impossible, because the functional structure of the protein is likely to be disordered, incomplete or even destroyed. GPCRs are particularly difficult to isolate as a functioning protein, as improper folding already affects their ability of recognizing ligands. Recent advances in synthetic biology by Robelek et al. [61, 62] avoid the isolation issue by an *in vitro* expression process of membrane proteins in the presence of model membranes. Thereby, the proteins are continuously incorporated into the model membranes and correctly folded during their expression.

Robelek et al. [62] observed the vectorial and functional incorporation of OR5 in a solid-supported tethered lipid membrane (tBLM). OR5 is an odorant receptor from *Rattus norvegicus* belonging to the vast GPCR family. The incorporation and orientation of the protein was shown by immunolabeling in combination with surface plasmon enhanced fluorescence spectroscopy (SPFS) and reversible ligand binding was shown by surface-enhanced infrared reflection absorption spectroscopy (SEIRAS). Receptor activation, i.e. upon ligand binding, is of primary interest in cell signaling and signal transduction. In general, the activation event itself and the conformation change of the receptor cannot be measured because this would very likely inhibit the receptor function. But based on induced events in the signaling cascade, a few methods for measuring the activation of GPCRs were developed. For instance, Heyse et al. [63] and Bieri et al. [64] observed the dissociation of the G protein from solid-supported membranes upon photo-activation of incorporated Rhodopsin, which led to a mass change measurable with surface plasmon resonance. In addition, several investigations showed that receptor–ligand binding considerably slows down the diffusion of these receptors, which is in general attributed to an aggregation of GPCRs (homo- or hetero-polymerization) in the cell membrane to launch the signaling cascade. For instance, Lill et al. [65] investigated the signaling kinetics of the neurokinin 1 receptor (NK1R). Initially, this receptor was found to diffuse either fast ($D \approx 0.21\mu\text{m}^2/\text{s}$) in domains of $\varnothing 1.1\mu\text{m}$ or slow ($D \approx 0.011\mu\text{m}^2/\text{s}$) within domains of $\varnothing 180\text{nm}$, but to slow down significantly within 1s after signaling.

In cooperation with R. Robelek and E.-K. Sinner, Max-Planck Institut für Polymerforschung, Mainz, Germany, we quantified the incorporation density and the translational mobility of OR5 using TIRF imaging and confocal FCS measurements. Whereas SPFS and SEIRAS measure the average signal from an area of a few mm^2 , TIRF imaging allows localization and detection of single OR5 receptors in the membrane. The aim of this investigation was to detect receptor–ligand binding by monitoring the lateral mobility of OR5 receptors in these artificial membranes (c.f. the review on FCS studies in model membranes by Kahya and Schwille [66]). The receptor mobility was investigated with FCS and fluorescence

recovery after photo-bleaching (FRAP) showing that the OR5 was well immobilized within the resolution limits of our instrumentation. The incorporation density in the membrane was further analyzed with TIRF microscopy and image analysis, which shows that the OR5 density and aggregation increased steadily with expression time.

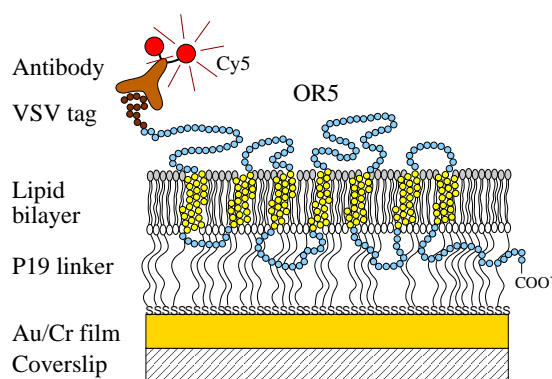


Figure 3.11: Solid-supported planar lipid membrane assembly with incorporated GCPR. The lipid bilayer consists of a first DMPE monolayer and a second lipid layer from spread PC vesicles. The VSV affinity tag was immunolabeled with a fluorescently labeled antibody.

Figure 3.11 outlines the solid-supported tBLM assembly with an incorporated OR5 receptor. The tBLM was prepared on a thin chromium–gold layer of $\lesssim 5.0\text{nm}$ thickness (see section 3.3.1). The receptor was expressed with a vesicular stomatitis virus (VSV) affinity tag at one terminal. This VSV tag served as target for immunolabeling with a fluorescently labeled antibody. This antibody was labeled with two Cy5 fluorophores (average, inferred from FCS of a 5nM antibody solution). In contrast to the SPFS measurements, no secondary antibody was required due to the higher detection sensitivity. To probe the orientation of inserted OR5 proteins, cDNA constructs with alternative positions for the tag sequence were used: one cDNA coded for a C-terminal VSV affinity tag, the other for an N-terminal VSV affinity tag.

All experiments were performed in a flow-through microfluidic cell containing a reaction chamber of about 50 μl volume. This chamber was sealed with the metal-coated coverslip providing a window for TIRF measurements. Two inlets at the extremities of the reaction chamber allowed to push/pull liquids through the chamber.

In first control experiments, the background of the metal-coated coverslips and PBS solution was measured. Without chromium, FCS measurements on 5.0nm gold films suffered from an uncorrelated background count rate of $> 3\text{MHz}$, whereas the chromium–gold sandwich led to $\lesssim 150\text{kHz}$ background at identical conditions. Therefore, all subsequent experiments were carried out on combined chromium–gold films. Compared to bare coverslips, the coating lowered the observed brightness of the Cy5 fluorophores by about 50% at identical excitation conditions. The relevant detection loss was estimated to be about 30%.⁶ The presence of tBLMs lowered the background by as much as 30%, possibly due to the lower amount of surface enhanced Raman scattering from water in contact with the metal coating. The quality of the tBLMs was verified by incubation with the anti-VSV–Cy5 (AV–Cy5) for 10min prior to the OR5 expression. TIRF images showed that the AV–Cy5 associated only at very few nanometric sites,

⁶ The excitation loss could be compensated by increasing the laser power.

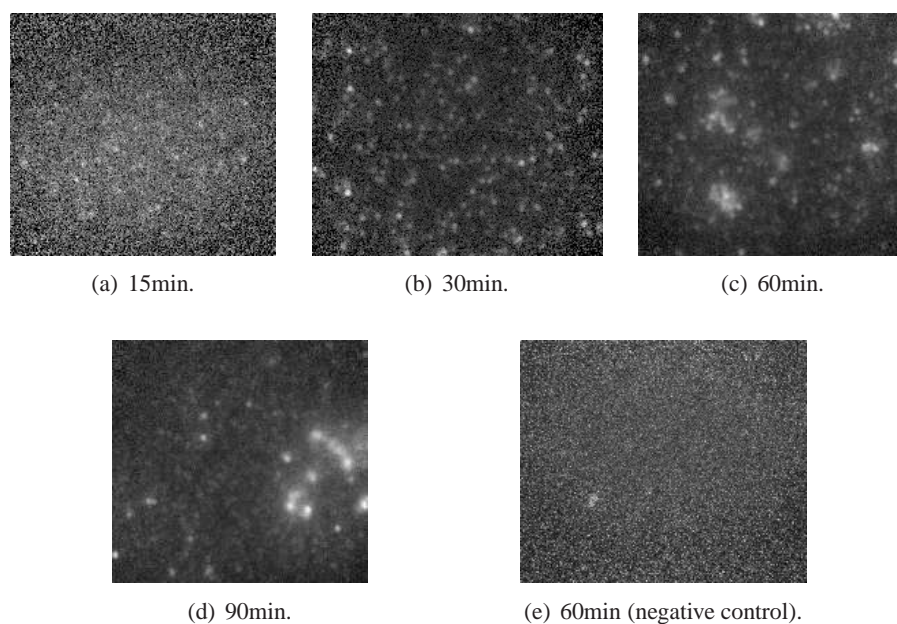


Figure 3.12: Background corrected and normalized membrane images versus expression time. The negative control (e) corresponds to 60min incorporation of OR5 with a VSV tag at the C' terminus.

in average about one site per $20\mu\text{m} \times 20\mu\text{m}$ area. This association was attributed to defects in the tBLM assembly, i.e. a missing top layer (imperfect vesicle spreading) or a small defect in the underlying metal coating. As these defects showed up much brighter than any other feature, they were readily identified and excluded from further analysis. Finally, it was confirmed that the incorporation of the OR5 did not affect the background.

In a next investigation, the vectorial incorporation of OR5 was confirmed. Figure 3.12 shows representative background corrected and normalized membrane images. Image (a) to (d) show the increase in the spot density and brightness with increasing expression time. Image (e) shows the negative control at 60min expression of OR5 with the VSV tag at the C' terminus. If the OR5 is fully incorporated and well oriented, this terminus is buried between the lipid membrane and the metal-coated coverslip as sketched in figure 3.11. This means, the anti-VSV-Cy5 marker should not be able to bind the tag. Indeed, only a few markers were monitored versus about 150 spots in case of the N' terminal tag. These measurements confirm the main results by Robelek et al. [62] as they show

1. the vectorial incorporation and
2. the complete incorporation of OR5,
3. the absence of incompletely fused vesicles, and
4. the excellent quality of the artificial membrane, which is intact and nearly defect-free,

In a first attempt, we tried to measure the receptor mobility with FCS. The dual-color instrument with its possibility to measure in a TIRF or confocal configuration was used in the confocal mode. Thereby, premature bleaching of neighboring OR5-AV-Cy5 complexes was minimized. Figure 3.13a shows the intensity traces of a sequence of $5 \times 20\text{s}$ measurements on incorporated OR5 (90min expression time) and a trace amount of AV-Cy5 still present after flushing the reaction chamber. The total intensity was composed of three components: a fast bleaching component (39%), a slowly bleaching component (35%), and

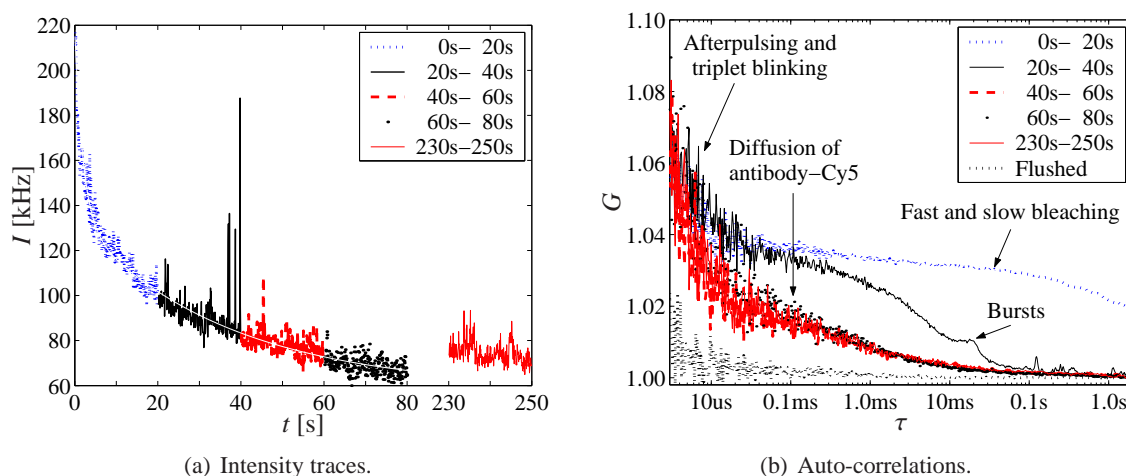


Figure 3.13: Intensity traces and FCS correlation curves, all taken at the same membrane position.

a "non-bleaching" component (26%) consisting of background and diffusing AV-Cy5. The fast bleaching fraction had a characteristic bleaching time of about 2.0s, whereas the slow bleaching occurred at a time scale of about 36s. The fast component was attributed to photo-bleaching close to the excitation focus. The slow component was attributed to photo-bleaching within a larger area of about $1\mu\text{m}$ diameter covered by the first side lobes of the excitation field. A few intensity bursts at $t \approx 40\text{s}$ were presumably due to non-specifically binding AV-Cy5. Figure 3.13b shows the corresponding auto-correlation curves. The strong initial bleaching resulted in a stretched decrease of the correlation amplitude. The second correlation curve represents mainly the intensity bursts with a characteristic time of 5ms to 10ms. The remaining curves are all very similar and represent the diffusion of AV-Cy5 in solution with a diffusion time $\tau_d \approx 0.15\text{ms}$. Before the last measurement, the excitation was interrupted for 150s. We observed an almost perfect on-take of the fluorescence intensity after this interruption. This effect was further investigated as it could stem (a) from diffusing OR5 in the membrane, (b) an exchange of AV-Cy5 complexes or (c) a small focus drift caused by the piezo-electric positioning device. Firstly, the focus position was verified and a small defocus was tracked and corrected. Indeed, the defocus stretched the diffusion curves shown in figure 3.13b. Secondly, remaining or dissociated AV-Cy5 were flushed with 5ml PBS. As a result, except of afterpulsing for lag times $\tau \lesssim 5\mu\text{s}$, no significant correlation amplitude was measured anymore. This result was reproduced on various membrane positions and for several samples. We concluded that if the OR5 diffuses, it must be so slow that it is below the detection limit set by photo-bleaching.

Thirdly, slow diffusion was monitored with fluorescence recovery after photo-bleaching (FRAP). First, the Cy5 was photo-bleached along a few lines and an image was captured. Later, the same area was imaged several times for checking for recovery after bleaching. Figure 3.14 shows the result of these FRAP experiments. Image 3.14a and 3.14b were taken with 6.5min time lapse. The difference image 3.14c shows that the receptors along the single line did not move (up-right corner). The bottom darkened due to a slight focus drift, which moved the excitation area upwards. Inside the "U", a single spot became much brighter, whereas two spots at the right just disappeared. However, the photo-bleached features did not recover nor a "edge" moving of the bleached pattern could be observed. This finding was confirmed with several FRAP measurements on this sample. For an expression time of 90min, we never monitored moving receptors although hundreds of CCD images were taken from several samples. Taking into ac-

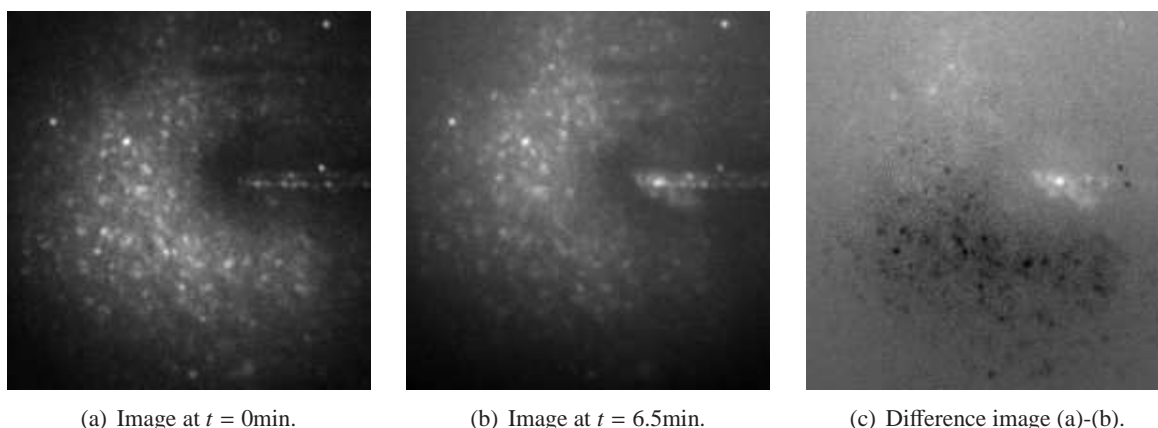


Figure 3.14: FRAP experiment. A line and a "U" were bleached and immediately imaged (a). After 6.5min, a second image was taken (b). The difference picture is shown in (c).

count the densely packed, corkscrew-shaped P19 linker immobilizing the tBLM and winding up with the α -helices of the receptor, it would have been surprising if the OR5 diffused above the resolution limit of our instrumentation. Constrained diffusion within small domains was monitored, in particular at low expression levels favoring OR5 monomers, but the diffusion was typically limited to domains of $\lesssim \varnothing 200\text{nm}$ (data not shown). These findings are supported by recent studies on GPCRs in living cells and in supported membranes. For instance, Jacquier et al. [67] investigated the trafficking of the human odorant receptor OR17-40 in living cells and analyzed their mobility with single particle tracking. The OR17-40 was found to diffuse with a diffusion constant in the order of $0.02\mu\text{m}^2/\text{s}$. About 40% were found immobile or constrained within domains of $\approx \varnothing 190\text{nm}$, 49% were diffusing within domains of $\varnothing 300\text{nm}$ to $\varnothing 550\text{nm}$ and about 11% were freely diffusing. Moreover, Perez et al. [68] showed that GPCRs immobilize upon preparation of supported membranes. These membranes were prepared by detaching the upper part of a cell membrane using a poly-L-lysine substrate. Whereas FRAP experiments performed on living cell membranes showed fast and complete recovery of bleached domains, no recovery was found on supported membranes stating that nearly all GPCRs were immobilized.

We would like to point out that single particle tracking based on TIRF images may be deceptive because the orientation of the observed fluorophore affects the shape of the PSF. When imaging partially immobilized fluorophores as the AV-Cy5, the fluorophore rotation is constrained (just slow and/or limited angular distribution), such that its image appears to wiggle around if the fluorophore changes its orientation. Wiggling was frequently observed at low expression levels, but limited to an area comparable to the PSF size (see section 3.3.4). The mobility of the OR5 requires further investigation, as the preliminary analysis did not differentiate between translational and rotational mobility.

Furthermore, the OR5 incorporation density and aggregation was analyzed. Two methods were applied: image segmentation to calculate the spot density SD or Airy density AD and ICS to retrieve the cluster density CD. These methods are briefly introduced in section 3.3.2 and 3.3.3. In a first approach, image segmentation was applied as outlined in figure 3.15. The Airy density AD (an improved estimate of the spot density) was then readily obtained with equation (3.18). Figure 3.16 shows the AD monitored at different expression levels obtained by varying the expression time in steps from 15min to 90min. The data points fitted in excellent agreement on a second order polynomial function of the form $AD(t) = AD_1(t - t_0) + AD_2(t - t_0)^2$. Whether it should fit to this model curve or not is questionable, but it

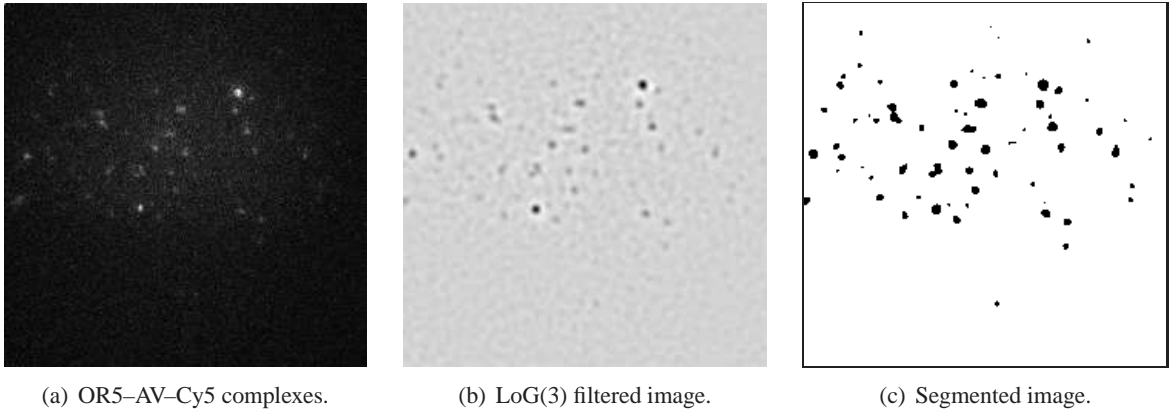


Figure 3.15: Image segmentation analysis.

allowed at least to extract the initial increase and to extrapolate the leadtime. A leadtime t_0 of 8.0min was estimated from the fit, e.g. OR5 were fully expressed and incorporated within about 8min. With increasing expression time, the OR5 density increased linearly with $AD_1 = 0.019\mu\text{m}^{-2}\text{min}^{-1}$ up to about 30min. In the time window of 20min to 30min, the AD variations were particularly low as a result of a homogeneous OR5 distribution in combination with an optimal image contrast and low noise. For even longer expression times, the increase of the AD slowed down with a curvature $AD_2 = -7.6 \cdot 10^{-5}\mu\text{m}^{-2}\text{min}^{-2}$. At $t = 130$ min, the AD would achieve a maximum of about $1.2\mu\text{m}^{-2}$. Taking into account that the evaluation method limits the AD to about $2/3A \approx 2.5\mu\text{m}^{-2}$, a saturating model curve given by

$$AD'(t) = AD'_1 \frac{(t - t_0)t_s}{(t - t_0) + t_s} \quad (3.5)$$

was tested. This model curve matched equally well to the measured AD^7 for $AD'_1 = 0.020\mu\text{m}^{-2}\text{min}^{-1}$ and $t_s = 135$ min. Hence, the upper bound of $AD < 2.7\mu\text{m}^{-2}$ was a pure artifact introduced by the evaluation method.

We concluded that the amount of expressed and incorporated OR5 increased linearly with expression time by about $0.020\mu\text{m}^{-2}\text{min}^{-1}$. The expression and incorporation of a single OR5 lasted about 8.0min, which is in good agreement with our expectations.

In a second approach, the membrane images were evaluated with ICS as described in section 3.3.2. The results are shown in figure 3.17a, whereas figure 3.17b exemplifies a spatial auto-correlation and the corresponding fit on a 2D Gaussian model curve. The measured cluster density CD was about $3\times$ larger than the AD. As the cluster density accounts not only for the number of spots but also for the distribution of the spot brightness, $CD > AD$ was expected. Excluding the data points at 15min and 60min, a linear regression on the data was performed (outlined as thin solid line). The leadtime was estimated to be 7.6min, which is in good agreement with the image segmentation analysis. The CD increased with time by $0.065\mu\text{m}^{-2}\text{min}^{-1}$, that is about $3.2 \times AD'_1$. However, the relative scattering of the CD data is significantly larger than for the AD data. The evaluation at 15min expression time was strongly biased by the low signal to noise ratio (see figure 3.12a). Therefore, the estimation of the CD is about an order of magnitude larger than expected. The evaluation at 22min to 45min expression time was much more reliable due to good image contrast and a low number of bright spots. At 60min, nearly all images showed

⁷ Not shown because hardly discernable from the polynomial fit.

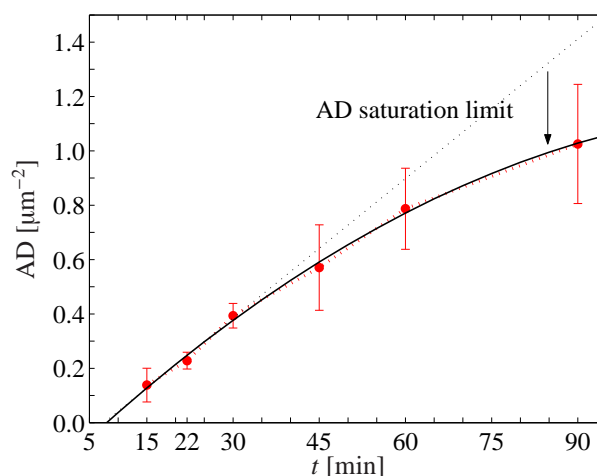


Figure 3.16: Airy density versus expression time t . Thin solid curve: fit on second order polynomial. The black dotted line indicates a linear increase estimated with the first three data points.

large-scale aggregates which led to auto-correlation curves with large waist w . As the contribution to the auto-correlation amplitude is proportional to the square of the feature brightness, these bright large-scale aggregates were the only detectable feature. The resulting CD at 60min represents therefore the density of large-scale aggregates instead of the protein density. At 90min, large aggregates were also monitored but they were organized rather in beads than clouds, which seems to be well mastered with the ICS fits.

Taking into account only well-defined data points at 20min to 45min, a linear increase in CD of $0.11\mu\text{m}^{-2}\text{min}^{-1}$ was monitored. Extrapolation to $\text{CD} = 0$ would indicate a leadtime of 17min, which is clearly disproved by the presence of many spots in images taken after 15min OR5 expression (figure 3.12a). The introduction of a transient up to about 20min and a limited processivity around 60min would correct for the overestimation of the leadtime as well as the overestimation of the CD at 90min. An improved ICS analysis and a more robust estimation of the CD are required to investigate this point further.

In summary, the vectorial and complete insertion of OR5 receptors into an artificial tethered membrane assembly was shown. Fluorescence spectroscopy (FCS and FRAP) showed that the incorporated receptors were immobilized. The incorporation density was monitored with ICS and image segmentation. It was shown that the amount of OR5 increased with expression time up to a few receptors or aggregates per μm^2 within 90min. Moreover, the mean time for expressing and incorporating a single receptor was estimated to about 8min. Comparing OR5 distributions at different expression times revealed that the first OR5 were incorporated at random positions. Thereafter, a tendency of incorporating several OR5 side-by-side was observed, presumably due to Ribosomes staying in contact with the membrane in between two expression cycles.

Image segmentation and spot analysis were very robust but did systematically underestimate the OR5 density. The ICS analysis provides, at least in principle, an unbiased estimation of the receptor density. Despite these first results, a more detailed study is needed in order to get a robust analysis with a relative scatter of 10% or less instead of about 50%. Preliminary FCS measurements were performed in order to monitor receptor–ligand binding. Due to the immobilized receptors, these measurements suffered from rapid photo-bleaching of the Cy5 labels. Future experiments should benefit from the dual-color perfor-

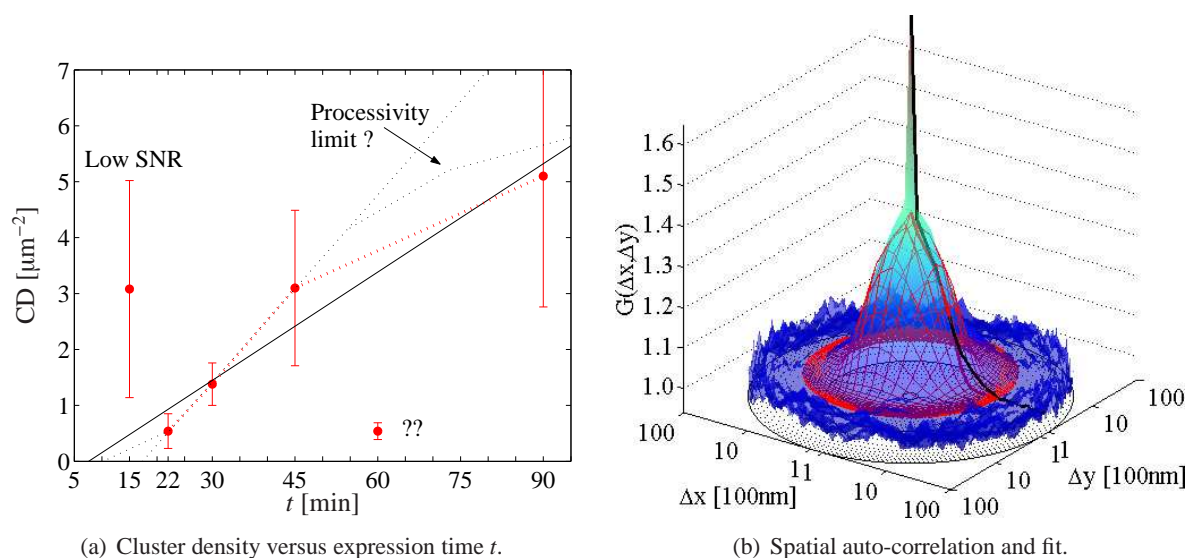


Figure 3.17: Measured cluster density. (a) Thin solid line: linear regression on data points at 22min to 45min and 90min. Thin dotted line: linear regression on data points at 22min to 45min with suggested on-set transition and processivity limit. (b) Mesh: fit on 2D Gaussian model curve.

mance of our TIR-FFS instrument. For instance, Förster resonant energy transfer in combination with dual-color TIRF imaging should enable monitoring the aggregation of receptors or the receptor-G protein interaction upon ligand binding.

In order to achieve translational diffusion of incorporated GPCRs, future investigations are in preparation to render the artificial membrane more fluid. The density and nature of the attachment layer is of particular interest for achieving an optimal compromise between lateral mobility and axial immobility. Using a small amount of fluorescently labeled lipid molecules, the lateral membrane mobility will be monitored with FCS. The axial mobility of the membrane is already subject of investigation with optical coherence tomography (OCT) and spectral interferometry.

3.3.1 Sample preparation

Preparation of chromium-gold layer Standard glass coverslips (150 μ m thick, Menzel-Gläser, Braunschweig, Germany) were cleaned and sonicated for 20min in 2% Hellmanex II (Hellma, Müllheim/Baden, Germany), rinsed with bidistilled water, dried and oxygen plasma cleaned. Planar gold surfaces were prepared by evaporating a 1.5nm thick chromium adhesion layer (99.99%, œrlikon balzers coating, Brügg, Switzerland) and a 3.5nm thick gold layer (> 99.99%, Metalor technologies SA, Neuchâtel, Switzerland) in an Edwards Auto 306 evaporation system at $5 \cdot 10^{-6}$ mbar. The evaporation rate was kept below 0.5nm/min. A thin chromium adhesion layer was required to obtain a hard gold coating (pale gray-brown) instead of porous and granulous gold deposits (brilliant blue appearance). Adding the chromium layer also lowered the background luminescence of the gold film by more than an order of magnitude.

Preparation of tBLM The tBLM were then prepared in a flow cell following the protocol by Robelek et al. [62]. This preparation of the tBLM was recently monitored with surface plasmon resonance spectroscopy by Wiltschi et al. [69].

In vitro expression of OR5-VSV A "T7 TNT Quick *in vitro* expression system" (Promega, USA) was used. The reactions were prepared according to the supplier's instruction. The incubation was performed in a thermoblock at $30.3^\circ\text{C} \pm 0.3^\circ\text{C}$ for 15min to 90min.

Labeling of the OR5-VSV The OR5-VSV was immunolabeled *in situ* by incubating with Cy5 labeled anti-VSV primary antibodies. After 10min, the excess labels were rinsed with PBS solution while monitoring the content of free labels with confocal FCS measurements. The PBS solution was then exchanged against a Gloxy antioxidant/PBS solution, which reduced the photo-bleaching to about 1/3 as compared to PBS.

3.3.2 Image correlation spectroscopy

The random spatial distribution of the incorporated OR5 was analyzed with image correlation spectroscopy (ICS). This method and its limitations were discussed in detail by Petersen et al. in reference [70]. ICS analyzes the spatial auto- or cross-correlation of the images I and J . The spatial cross-correlation C of I and J is defined by

$$C(\Delta x, \Delta y) = I(x, y) \star J(x, y) = \iint_{-\infty}^{+\infty} I(x + \Delta x, y + \Delta y) J(x, y) dx dy \quad (3.6)$$

where Δx and Δy are the lag distances. As usual, the spatial auto-correlation is obtained by setting $J = I$. For digital images, the fast Fourier transform can be used for calculating the correlation as a convolution of $I(-x, -y)$ and $J(x, y)$. Similar to equation (3.1) for FCS, the normalized spatial cross-correlation is given by ($\langle \rangle$ denotes the spatial average)

$$G(\Delta x, \Delta y) = \frac{I \star J}{\langle I \rangle \langle J \rangle} = \frac{\langle I(x + \Delta x, y + \Delta y) J(x, y) \rangle}{\langle I(x + \Delta x, y + \Delta y) \rangle \langle J(x, y) \rangle}. \quad (3.7)$$

With this equation, "infinitely" large images of homogeneously excited samples can be treated as the lateral extent is unbounded. For treating images of finite extensions, a symmetric normalization should be applied. This normalization was introduced in equation (3.1) to deal with short measurements. For ICS, a general mask W can be introduced for defining a weighted average with weight $W(x, y) \in [0, 1]$ at point (x, y) . Equation (3.7) is then generalized for images of finite size and arbitrary shape (defined by $W \neq 0$), e.g.

$$G(\Delta \vec{r}) = (W \star W) \frac{I \star J}{(I \star W)(W \star J)} \quad (3.8)$$

with $\Delta \vec{r} = (\Delta x, \Delta y)$. The prefactor corresponds to the factor $(T - \tau)$ in equation (3.1), as it stands for the cumulated weight at lag distances Δx and Δy , whereas the denominator is the product of the weighted average of the images I and J . The performance of this normalization is outlined in figure 3.18. The correlation amplitude G_0 of about 0.2 is reproduced to less than 5% difference independently of the choice of the mask W . At large lag distances, the difference ΔG is dominated by stochastic noise with zero mean and about 0.01 amplitude.

The correlation amplitude G_0 is defined by

$$G_0 = \lim_{\Delta r \rightarrow 0} (G(\Delta \vec{r})) - \lim_{\Delta r \rightarrow \infty} (G(\Delta \vec{r})) = \lim_{\Delta r \rightarrow 0} (G(\Delta \vec{r})) - G_\infty \quad (3.9)$$

where the offset $G_\infty \approx 1$ is the correlation amplitude at large lag distances. The amplitude G_0 equals the variance of the normalized intensity fluctuations. If the intensity is an accurate representation of the sample density, its variance is also the variance of the density fluctuations, which equals the inverse of the average occupation number N_p :

$$G_0 = \frac{\langle (I - \langle I \rangle)^2 \rangle}{\langle I \rangle^2} = \text{var}(\delta_n I(\vec{r})) = \text{var}(\delta_n c(\vec{r})) = \frac{1}{N_p} \quad (3.10)$$

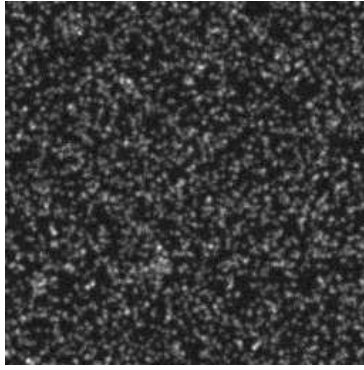
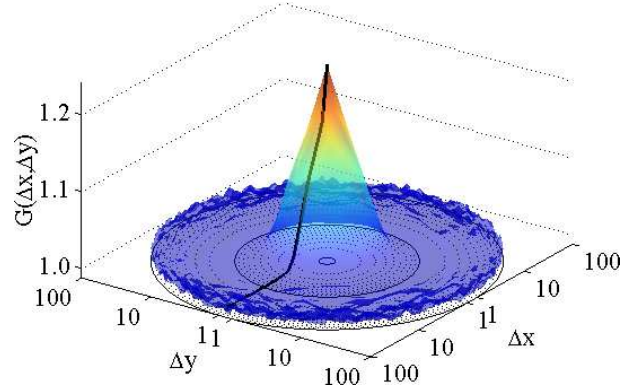
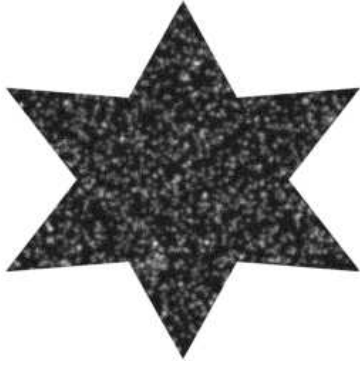
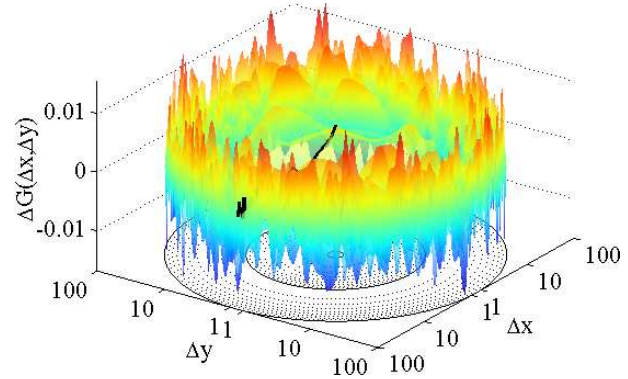
(a) Image intensity I with uniform mask $W = 1$.(b) Auto-correlation $G_{I \times I}(\Delta \vec{r})$.(c) Image intensity J with star-shaped mask W .(d) Difference $\Delta G = G_{I \times I} - G_{J \times J}$.

Figure 3.18: Invariance of the auto-correlation $G(\Delta \vec{r})$ for different masks $W(x, y)$. The images were 256×256 pixels in size. In order to emphasize the correlation amplitude near the coordinate origin, $G(\Delta \vec{r})$ is represented in polar coordinates with logarithmic radius Δr . The correlation is represented for lag distances $\Delta r \leq 100$ pixel. The black curve represents the average amplitude along the radius.

The occupation number N_p gives the number of receptors (particles) in the observation volume, which is defined by the PSF of the TIRF microscope. Considering the EMCCD camera (Andor Luca, monochrome) as an array of square sized pixels ($9 \mu\text{m} \times 9 \mu\text{m}$, 80% fill factor) in a $10 \mu\text{m}$ grid, the PSF for a single active element can be calculated as described in chapter 2. In this study, it is sufficient to calculate a cross-section for a fluorophore 10 nm above the glass interface as this is approximately the glass-(OR5-AV-Cy5) distance. According to Petersen et al. [70], the receptor density is therefore given by the cluster density

$$\text{CD} = \frac{1}{G_0 A} = \frac{N_p}{A} \quad (3.11)$$

where A is the area of this PSF cross-section:

$$A = \frac{1}{\text{PSF}(0)} \int \text{PSF}(\vec{r}) d\vec{r} \quad (3.12)$$

If the cross-section is approximately Gaussian with waist w , the area can be estimated by fitting $G(\Delta \vec{r})$ on a 2D Gaussian centered near the origin. The model function for fitting the spatial image correlation is therefore given by

$$G(\Delta \vec{r}) = G_\infty + G_0 \exp\left(-\frac{|\Delta \vec{r} - \vec{r}_0|^2}{w^2}\right) \quad (3.13)$$

where \vec{r}_0 accounts for small image drifts in cross-correlation measurements. The waist of the fitted Gaussian is defined by the PSF. Hence, the area A can be estimated by $A \approx \pi w^2$.

Fitting Images of single receptors or small receptor aggregates show intensity spots of the size of the PSF. This size can be measured independently for unspecifically binding molecules. If the fitted waist w differs by more than about 30%, the data should be rejected as the image probably contains features similar or larger in size than the PSF. Alternatively, these features can be masked by defining a matching window W . Due to the limited size of the images, the offset G_∞ shows variations in the order of $\sqrt{N_A}/N_A$, where N_A is the number of PSF areas in the window W . It was shown that the fit should include only data in the correlation function $G(\Delta\vec{r})$ for $\Delta r \lesssim 3w$ [71]. Using proper normalization this constraint can be relaxed to $\Delta r \lesssim s/2$, where s is the smallest dimension in the window W .

Corrections In general, the intensity fluctuations are due to several sources, i.e. the sample of interest (s), non-specific fluorescence (ns), auto-fluorescence (a) and background (wn). Except the background, these sources show fluctuations with the characteristic dimension of the PSF. The background has the characteristics of white noise and contributes not to the correlation except at the origin where it can be dominant. Therefore, the amplitude $G(0)$ at the origin was excluded from the fits. Assuming that these sources are independent as they are from different components, the measured correlation is given by

$$g(\Delta\vec{r}) = \sum_i g_i(\Delta\vec{r}) \langle I_i \rangle^2 \quad (3.14)$$

where $g_i(\Delta\vec{r}) = G_i(\Delta\vec{r}) - 1$ is the correlation of $\delta I_i(x, y) = I_i(x, y) - \langle I_i \rangle$, that is $g_{i\infty} \approx 0$ and $g_0 = G_0$. The fitted correlation amplitude G_0 can be corrected according to

$$G_{s0} = \frac{G_0 \langle I \rangle^2 - G_{ns0} \langle I_{ns} \rangle^2 - G_{a0} \langle I_a \rangle^2}{(\langle I \rangle - \langle I_{ns} \rangle - \langle I_a \rangle - \langle I_{wn} \rangle)^2}. \quad (3.15)$$

Analysis The instrument background, the auto-luminescence of the metal-coated coverslip and the auto-fluorescence of the bare tBLM was measured a priori. This combined background $I_{wn}(x, y)$ had white-noise characteristics as the auto-correlation confirmed (see figure 3.19). The slow variation stems from the envelope of the background intensity as outlined in figure 3.20a. Instead of correcting the background contribution with equation (3.15), the background was subtracted from the image intensity a priori. This was required for normalizing the image intensity with the inhomogeneous excitation intensity $I_{ex}(x, y)$. The excitation intensity was estimated by fitting the average background corrected intensity of a large number of images on a model distribution (modulated 2D Gaussian). The correlation was then performed on the homogenized images I_c given by

$$I_c = \frac{I - I_{wn}}{P_{ex}} \quad (3.16)$$

where P_{ex} is the fitted excitation intensity profile but normalized to unit amplitude. Figure 3.20 outlines the applied correction.

The contribution from non-specific fluorescence and auto-fluorescence was estimated by measuring a sample prepared according to the protocol given in section 3.3.1, but with no coding DNA added to the *in vitro* expression Ansatz. Thereby, the membrane was exposed to the expression Ansatz as well as the labeled antibody. However, these contributions turned out to be negligible, such that the OR5 cluster density was estimated directly with equation (3.11).

3.3.3 Image segmentation

If the cluster density CD is lower than about $1/A$, where A is the PSF cross-section (see section 3.3.4), individual spots can be resolved. In this case, image segmentation methods can estimate the CD based on a spot analysis.

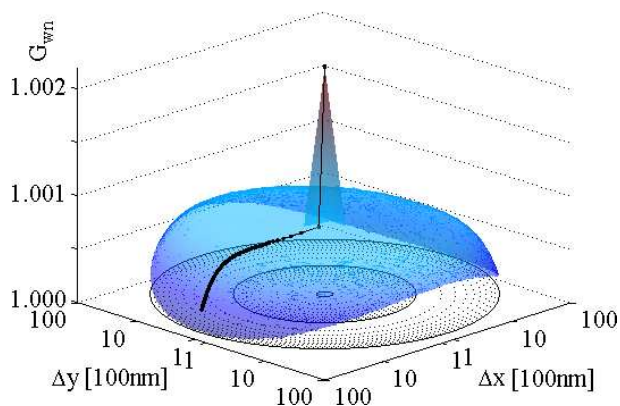


Figure 3.19: Background correlation $G_{wm}(\Delta\vec{r})$. The projected CCD pixel size is 100nm.

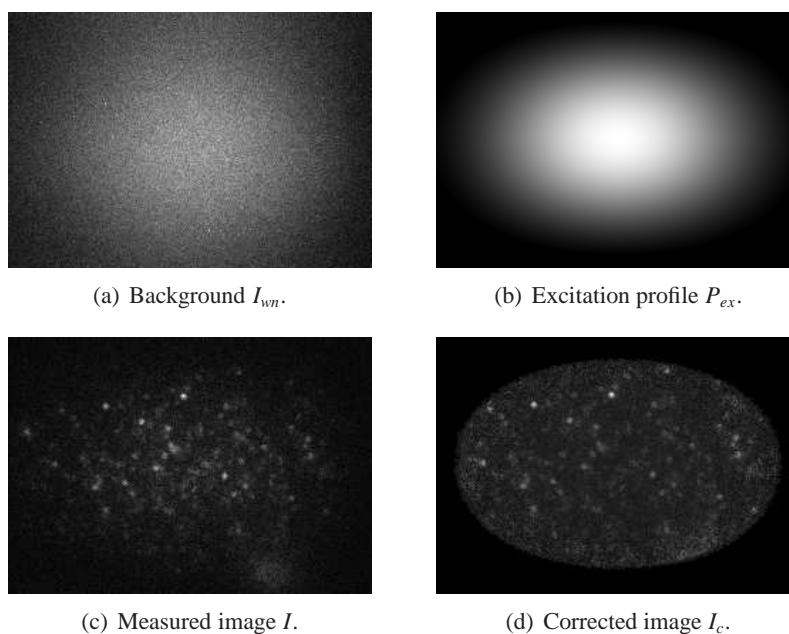


Figure 3.20: Applied image correction. The background (a) was first subtracted from the measured image (c). The result was then divided by the excitation profile (b). The correlation was performed on the corrected image (d), where the window W covers the region where $P_{ex}(x, y) > 0.2$, that is an elliptical area of $23\mu\text{m} \times 15\mu\text{m}$ extension on the membrane.

Spot density For calculating the spot density SD, the images were first filtered with a Laplacian-of-Gaussian filter of width 3 (LoG(3), see figure 3.21) to remove noise and enhance the edges [72]. A threshold was then applied and the resulting segments were analyzed in shape and brightness. The spot density is readily given by

$$SD = \frac{N_s}{A_{ex}} \quad (3.17)$$

where N_s is the number of spots (segments) identified in the excitation area A_{ex} of the image.

As figure 3.15c shows, the applied segmentation method found the majority of spots but with areas proportional to the spot brightness. The spot density yields a lower bound of the OR5 density as it accounts large aggregates

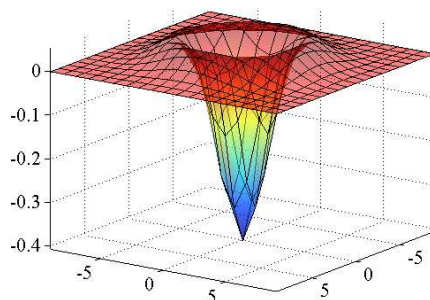


Figure 3.21: Laplacian-of-Gaussian filter of width 3. All units in pixel (100nm).

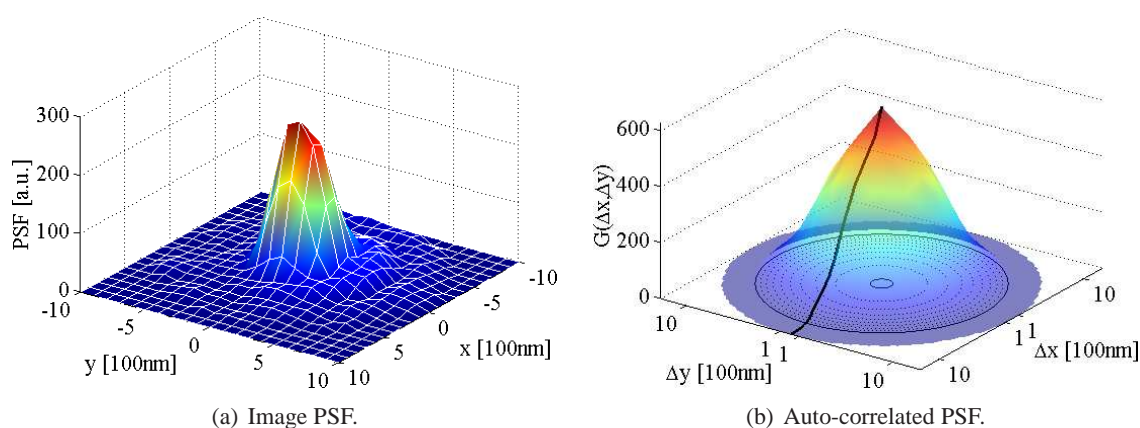


Figure 3.22: Imaging point spread function and its auto-correlation.

exactly like a single receptor. Therefore, at least a first order correction should be applied to account for the area of large aggregates.

Airy density Given the spot area A_s , the number of spots N_s can be estimated with the cumulated spot area normalized by the PSF cross-section A . Therewith, N_s accounts for A_s and would be biased by the spot brightness if no further correction were applied. For instance, dim spots were identified as small spots of a few image pixels only as exemplified in figure 3.15c. This bias can be corrected in first order by taking the maximum brightness I_s of each spot into account. For a given LoG filter and threshold setting, the relation $A_s(I_s)$ can be estimated by calculating the segment area $A_{\text{PSF}}(I_s)$ obtained for the measured PSF image with identical peak brightness I_s . Taking the peak brightness as parameter is justified as it is most likely included in the segmented spot area. Therefore, an improved estimation of the receptor density is given by

$$\text{AD} = \frac{1}{A_{ex}} \sum \frac{A_s}{A_{\text{PSF}}(I_s)} \quad (3.18)$$

which we called area or Airy density as N_s is estimated based on the PSF cross-section. The Airy density removes the bias caused by large-scale aggregation, but removing the bias due to micro-aggregation within an area $\lesssim A$ requires further investigation.

A second order correction would consist in breaking large spots into segments of an area $A_s \approx A$. Thereby, large intensity fluctuations within a spot could be taken into account. This correction was not required as the few very large spots had a quite narrow intensity distribution, such that the correction factors for sub-segments would not scatter much.

3.3.4 Point spread function

The detection PSF was measured by averaging the image of several bright spots. Figure 3.22a shows the measured PSF, which was in good agreement with an Airy pattern except for an asymmetry in the Airy rings. This asymmetry might be due to a partially polarized fluorescence emission. However, the bright spots used for this measurement were attributed to a large number of Cy5, such that the polarization should be neglectable. The PSF cross-section was evaluated with equation (3.12) and $A = 0.26\mu\text{m}^2$ was obtained. This corresponds to a waist $w = 0.29\mu\text{m}$, which is in excellent agreement with the calculated Airy radius of $0.28\mu\text{m}$ for a wavelength of 670nm . The auto-correlation of the measured PSF served as reference for classifying the ICS fits ($w_{\text{PSF}} = 0.47\mu\text{m}$).

Chapter 4

List of articles

The results of this thesis have been partially published as indicated in the author's publication list. Some of the publications are only indirectly related to FFS, but served for several experimental and theoretical details.

Articles [10, 9] In cooperation with B. Karamata, a fast Monte-Carlo simulation for calculating multiple scattering in optical coherence tomography (OCT) was developed. This simulation tool allowed predicting wide-field OCT measurements with high accuracy. Subsequently, a similar Monte-Carlo simulation tool for predicting FFS measurements was developed (unpublished work). This fast FFS simulation integrates the entire FFS process outlined in chapter 2, Brownian diffusion of the sample molecules as well as active/passive transport or flow. The result of a simulated experiment is the raw detected photon trace, which exhibits stochastic fluctuations as real experimental FFS data.

Patent [5] The fast focus field calculation algorithm developed and described in [3] was used for the Bessel beam simulation and analysis.

- L1. R. Robelek, M. Leutenegger, B. Wiltschi, E. S. Lemke, D. Oesterheld, T. Lasser, E. K. Sinner, "In vitro synthesis of GPCRs in a solid supported planar lipid membrane system," *Biophys. J.*, 38A Suppl. S (2007).
- L2. M. Leutenegger, K. Hassler, P. Rigler, A. Bilenca, T. Lasser, "Single molecule detection at surfaces," in K. Kneipp, American Chemical Society, R. Aroca, H. Kneipp (eds.), *New Approaches in Biomedical Spectroscopy*, Am. Chem. Soc. Books, ISBN 0841274371 (2007).
- L3. M. Leutenegger, R. Rao, R. A. Leitgeb, T. Lasser, "Fast focus field calculations," *Opt. Express* **14**, 11277–11291 (2006).
- L4. M. Leutenegger, H. Blom, J. Widengren, C. Eggeling, M. Gösch, R. A. Leitgeb, T. Lasser, "Dual-color total internal reflection fluorescence cross-correlation spectroscopy," *J. Biomed. Opt.* **11**, 040502 (2006).
- L5. R. A. Leitgeb, T. Lasser, M. Leutenegger, L. Steinmann, M. Villiger, "Optical Imaging System with Extended Depth of Focus," PCT/IB 2006/050250, *patent pending* (2006).
- L6. L. C. Hwang, M. Leutenegger, M. Gösch, T. Lasser, P. Rigler, W. Meier, T. Wohland, "Prism-based multicolor fluorescence correlation spectrometer," *Opt. Lett.* **31**, 1310–1312 (2006).
- L7. M. Leutenegger, M. Gösch, A. Perentes, P. Hoffmann, O. J. F. Martin, T. Lasser, "Confining the sampling volume for Fluorescence Correlation Spectroscopy using a sub-wavelength sized aperture," *Opt. Express* **14**, 956–969 (2006).
- L8. K. Hassler, M. Leutenegger, P. Rigler, R. Rao, R. Rigler, M. Gösch, T. Lasser, "Total internal reflection fluorescence correlation spectroscopy (TIR-FCS) with low background and high count-rate per molecule," *Opt. Express* **13**, 7415–7423 (2005).
- L9. B. Karamata, M. Leutenegger, P. Lambelet, M. Laubscher, S. Bourquin, T. Lasser, "Multiple scattering in optical coherence tomography. Part II: Experimental and theoretical investigation of cross-talk in wide-field optical coherence tomography," *J. Opt. Soc. Am. A* **22**, 1380–1388 (2005).

- L10. B. Karamata, P. Lambelet, M. Laubscher, M. Leutenegger, S. Bourquin, T. Lasser, "Multiple scattering in optical coherence tomography. Part I: Investigation and modeling," *J. Opt. Soc. Am. A* **22**, 1369–1379 (2005).
- L11. A. Perentes, I. Utke, B. Dwir, M. Leutenegger, T. Lasser, P. Hoffmann, F. Baida, M. P. Bernal, M. Russey, J. Salvi, D. Van Labeke, "Fabrication of arrays of sub-wavelength nano-apertures in an optically thick gold layer on glass slides for optical studies," *Nanotech.* **16**, S273–S277 (2005).
- L12. R. Rigler, L. Edman, S. Wennmalm, M. Leutenegger, T. Anhut, T. Lasser, "Non equilibrium catalysis of single enzyme molecules," *Abstracts Pap. Am. Chem. Soc.* **228**, U201–U202 7-PHYS Part 2 (2004).
- L13. A. Perentes, A. Bachmann, M. Leutenegger, I. Utke, C. Sandu, P. Hoffmann, "Focused electron beam induced deposition of a periodic transparent nano-optic pattern," *Microel. Eng.* **73–74**, 412–416 Sp. Iss. SI (2004).

Chapter 5

Conference contributions

- M1. H. Blom, M. Leutenegger, C. Eggeling, J. Widengren, T. Lasser, "Dual-color Total Internal Reflection Fluorescence Fluctuation Spectroscopy," Northern Optics 2006, Bergen, Norway (Jun 14–16, 2006).
- M2. M. Leutenegger, H. Blom, J. Widengren, C. Eggeling, M. Gösch, T. Lasser, "Dual-color Total Internal Reflection Fluorescence Fluctuation Spectroscopy," EOS Topical Meeting on Molecular Plasmonic Devices, Engelberg, Switzerland (Apr 27–29, 2006).
- M3. M. Leutenegger, H. Blom, J. Widengren, C. Eggeling, M. Gösch, T. Lasser, "Dual-color Total Internal Reflection Fluorescence Fluctuation Spectroscopy," 8. annual Linz Winter Workshop, Linz, Austria (Feb 3–6, 2006).
- M4. R. A. Leitgeb, L. Steinmann, C. Imboden, M. Villiger, M. Leutenegger, A. H. Bachmann, T. Lasser, "High-resolution Fourier domain optical coherence microscopy," SPIE **6079-33** (Jan 2006).
- M5. R. A. Leitgeb, L. Steinmann, C. Imboden, M. Villiger, M. Leutenegger, A. H. Bachmann, T. Lasser, "Highly confined depth focus for Fourier domain optical coherence microscopy," SPIE **6090-07** (Jan 2006).
- M6. M. Leutenegger, A. Perentes, M. Gösch, T. Lasser, P. Hoffmann, "Fluorescence Correlation Spectroscopy on a Single Aperture," 2005 Annual Meeting of the Swiss Soc. Biomed. Eng., Lausanne (Sep 28, 2005).
- M7. B. Karamata, P. Lambelet, M. Leutenegger, M. Laubscher, S. Bourquin, T. Lasser, "A semi-analytical model accounting for multiple scattering in optical coherence tomography," SPIE **5690**, 386–396 (2005).
- M8. R. Rigler, L. Edman, S. Wennmalm, M. Leutenegger, T. Anhut, T. Lasser, "Non equilibrium catalysis of single enzyme molecules," Am. Chem. Soc. **228** (Aug 2004).
- M9. T. Lasser, T. Anhut, A. Serov, K. Hassler, R. Rao, M. Leutenegger, A. von Mühlänen, R. Chatton, P. Hoffmann, I. Utke, R. Popovic, P. A. Besse, A. Rochas, M. Gösch, R. Rigler, R. Brunner, "A look into life sciences - More than a side step from industrial inspection?" SPIE **5144**, 504–512 (2003).

Chapter 6

Conclusions and outlook

Two novel methods for performing fluorescence fluctuation spectroscopy (FFS) and fluorescence imaging on surfaces were developed. For the first concept, the near fields of sub-wavelength sized nano-apertures were used for exciting fluorophores in strongly confined volumes. For the second method, the evanescent field created by total internal reflection (TIR) at a glass–water interface was used for two-color excitation of fluorophores in the vicinity of the coverslip. These methods were characterized by calculating the observation volumes and by measuring the FFS performance with test samples. Finally, TIR excitation was applied for investigating odorant receptors in solid-supported planar lipid membranes.

Inspired by scanning near field optical microscopy (SNOM), we investigated the confinement of the observation volume in the near field of nano-apertures through an opaque gold film. Back-illumination of these sub-wavelength sized apertures resulted in a strongly confined excitation field near the distal aperture exit. For apertures with a diameter of $1/5$ of the free space wavelength, observation volumes as small as 30nl were achieved, which is less than $1/10$ of state of the art confocal far field observation volumes. These observation volumes had a lateral extent of about $200\text{nm} \times 250\text{nm}$ and an axial extent of less than 100nm . The performance of this excitation method was characterized with fluorescence correlation spectroscopy (FCS). These FCS measurements showed a substantial reduction of the diffusion time τ_d , e.g. the average transit time of fluorophores through the observation volume, which was in good agreement with theory. A significant reduction of the average number N of fluorophores within the observation volume was measured. The reduction of N was less pronounced than the estimation based on τ_d and calculations because N is strongly affected by the signal to background ratio (SBR) whereas τ_d is not. Auto-luminescence of the gold mask as well as Raman scattering added a significant background, which varied up to an order of magnitude due to hole-to-hole fabrication irregularities. Although N is a direct measure of the observation volume, the variation of the SBR significantly lowered the accuracy for the precise determination of N . Nevertheless, a SBR of 5 was achieved for nanoholes with $\varnothing 150\text{nm}$, which is as good as or even better than currently achieved in epi-illumination nanohole experiments by Levene and Rigneault.

Future work should first focus on a further decrease of the background as well as its variation. This can be achieved to a large extent by selecting other materials, i.e. aluminum masks on fused silica substrates as used by Rigneault and Webb. The major advantage of gold is its outstanding corrosion resistance in biological environments and its excellent biocompatibility, which can be of decisive advantage for long-term studies. Combined with microfluidic chips, the aperture masks will allow automated batch investigations of a full sequence of samples per nanohole. In addition, these nanohole masks are a promising platform for monitoring biological processes *in vivo* with unprecedented spatio-temporal resolution as for instance trans-membrane transport or cell signaling. Further, a suitable FCS model curve should be developed for improving the accuracy and persistence of the fitted parameters. The development of this FCS model curve will include the entire FFS process outlined in chapter 2, e.g. the calculation of the excitation field, the absorption and fluorescence re-emission as well as the detection efficiency. Optionally, the apertures could be filled and sealed with a dielectric material to provide a flat surface, which would also completely suppress diffusion inside the apertures and probably simplify the modeling. We

are convinced that a SNOM-type near field excitation is suitable for FFS measurements with solutions of micromolar fluorophore concentration. Currently, sample handling and mask fabrication are still not-so-simple issues for routine application. The choice of biocompatible, non-corrosive, low-background materials will be crucial for a future multi-color multi-spot FFS platform for *in vitro* and *in vivo* studies at natural sample concentrations and with high spatio-temporal resolution.

In the ongoing search for improved confinement of the excitation field, a novel dual-color TIR-FFS setup was developed and characterized. Two cw lasers provided a dual-color TIR excitation at 488nm and 633nm wavelength, respectively. The induced fluorescence was separated into a green channel (500nm to 540nm) and a red channel (650nm to 720nm) for single photon detection. The proposed setup features a common observation volume that is confined to the proximity of the coverslip surface. A theoretical analysis of the complete FFS process including the excitation field, the response of the fluorophore and its interaction with the surface, as well as the collection and detection efficiency was performed. These numerical calculations yielded an observation volume of 71al in the green channel and 103al in the red channel, which penetrate only about 120nm into the sample. Due to the high numerical aperture of the collection optics (1.45 NA), the system provides outstanding detection efficiency close to the coverslip surface. Very high photon count rates up to 650kHz per molecule were achieved for freely diffusing fluorophores. These count rates were approximately two-fold higher than obtained with state of the art confocal FCS instruments.

Dual-color TIR-FFS measurements were performed using a double-stranded doubly labeled DNA strand as dual-color sample and standard fluorophores as single-color samples. A two-color global FCS (2CG-FCS) analysis revealed an excellent performance for coincidence studies, e.g. the measured fraction of a dual-color sample scaled linearly with the fraction that was present in solution. Based on this analysis, the overlap of the observation volume was estimated to be 60%, which is close to the theoretical maximum. However, the measured observation volumes were substantially larger than the theoretical calculations. In the red channel, the measured observation volume was about 60% larger than predicted, which is presumably due to a lower excitation angle resulting in a significantly deeper penetration of the evanescent excitation field. In the green channel, the measured observation volume was 12 \times larger than expected, whereas the diffusion time τ_d was in good agreement with the predictions. This substantial discrepancy was attributed to fluorophores immobilizing at the coverslip and contributing a significant background. This unspecific binding at the coverslip is hardly suppressed completely. Hence, a SBR \lesssim 3 was achieved with 10nM sample concentration as this TIR-FFS instrument was designed for higher concentrations. Indeed, samples with 100nM to 200nM concentration yield an optimal SBR \gtrsim 25, whereas standard far field confocal instrumentation is better suited at nanomolar sample concentration.

In addition, a two-dimensional fluorescence intensity distribution analysis (2D-FIDA) was performed. The 2D-FIDA results confirmed the suitability for coincidence studies and led to equivalent results as the 2CG-FCS analysis. For measurement times of 10s or longer, 2CG-FCS provided a superior statistical significance for coincidence studies. For shorter measurement times however, 2D-FIDA outperformed 2CG-FCS mainly because 2CG-FCS did not track fractions of more than 50% of the dual-color sample in this case.

The dual-color TIR-FFS set-up allows a TIR mode as well as a confocal configuration. This possibility proved to be helpful for specific demands, for instance when the bleaching aspects are of importance. This modification of the excitation mode is relatively simple but still prone to slight misalignments in the excitation paths. Ideally, a simple shutter for selecting confocal or TIR mode could switch the excitation, such that the alignment is no longer affected.

A further extension of this setup was introduced recently. Using ps pulsed laser excitation, time-resolved single photon detection and adding a fast and sensitive CCD array, image correlation microscopy can be performed. The ps pulsed laser excitation and the time-resolved single photon detection provide an excellent tool for lifetime measurements, as well as for circumventing excessive photo-bleaching and background. Photo-bleaching is diminished using pulsed interleaved excitation (PIE) to avoid simultaneous dual-color exposure of fluorophores, which generates bleaching of red fluorophores in particular. The background is better mastered by introducing a time gate retaining only delayed photons (fluorescence). Benefiting from the very high photon count rate, the EMCCD camera is able of imaging single fluorophores at video rate.

With this new instrument, the *in vitro* expression of an odorant receptor (OR5) and its incorporation into a solid-supported planar lipid membrane were investigated. Complete vectorial insertion of OR5 receptors into an artificial tethered membrane assembly was achieved. FCS and FRAP showed that the incorporated receptors were immobilized within the resolution limit of our instrument. Preliminary FCS measurements were performed in order to monitor receptor–ligand binding. Due to the immobilized receptors, these measurements suffered from rapid photo-bleaching of the Cy5 labels. The incorporation density was monitored with ICS and image analysis and found to increase with expression time up to a few receptors or aggregates per μm^2 within 90min. An average time of 8min for expressing and incorporating a single receptor was measured. Comparing OR5 distributions at different expression times revealed that the first OR5 were incorporated at random positions. Thereafter, a tendency of incorporating several OR5 side-by-side was observed, presumably due to Ribosomes staying in contact with the membrane in between two expression cycles.

Image segmentation and spot analysis proved to be robust but led to a systematic underestimation of the OR5 density. Their major advantage is the localization of receptors and aggregates, which allows investigating their mutual organization. On the other hand, the ICS analysis provides in principle an unbiased estimation of the receptor density. Despite first results, a more detailed study is needed in order to achieve a robust ICS analysis with a relative scatter of 10% or better. If performed with confocal laser scanning microscopy (LSM), ICS is yet a robust tool for estimating cluster densities and colocalization probabilities.

To our knowledge, this is the first successful investigation of the *in vitro* expression and incorporation into artificial membranes at the single molecule level. This first achievement relied on our dual-color TIR-FFS and TIRF imaging instrument, which provides a unique platform for detailed membrane studies. In order to achieve translational diffusion of incorporated GPCRs, future investigations are in preparation to render the artificial membrane more fluid. The density and nature of the attachment layer is of particular interest for achieving an optimal compromise between lateral mobility and axial immobility. The axial mobility of the membrane is already subject of investigation with optical coherence tomography (OCT) and spectral interferometry. Future experiments are planned to benefit from the dual-color performance of our TIR-FFS instrument. For instance, Förster resonant energy transfer in combination with dual-color TIRF imaging should enable monitoring the aggregation of receptors or the receptor–G protein interaction upon ligand binding.

In summary, new concepts for confining the observation volume in FFS experiments were developed and characterized. For this purpose, the calculation of the observation volume was outlined and a versatile dual-color TIR-FFS instrument was build. This instrument forms now the base platform for single- or dual-color FFS investigations on surfaces as well as for TIRF microscopy. Finally, this novel platform was successfully applied to study the incorporation of an odorant receptor in a planar lipid membrane.

Acknowledgements

This work was accomplished because so many people believed in me and helped me with their competence.

First of all I would like to thank my doctor father Prof. Theo Lasser for his engagement, his motivation, for the many fruitful discussions around a cup of coffee and, last but not least, his continuous interest in this project.

I would like to thank all people who cooperated with me on different research projects. Thanks go to the Nanostructuring Research Group (NRG) at EPFL for supporting the nano-aperture arrays. In particular, Alexandre Perentes spent countless effort in fabricating the aperture masks to my satisfaction. I would like to thank Benjamin Dwir for electron-beam and nanostructuring assistance and Dr. Patrik Hoffmann for supporting this work. Many thanks go to Prof. Olivier J. F. Martin of the Nanophotonics and Metrology Laboratory (NAM) at EPFL for the calculation of the near field of nano-apertures.

Special thanks go to Michael Gösch for his enthusiasm and the challenge to build and test a dual-color TIR-FFS system in one week. I would like to thank Kai Hassler for his help in preparing "non-sticking" coverslips and Ling Chin Hwang for helping out with first test samples. I thank Aram Mooradian of Novalux for the Protera laser and his continuous interest in our work, Rainer Erdmann of PicoQuant for the 470nm ps pulsed laser and Klaus Weisshart of Carl Zeiss for contributing the cross-correlation sample. I would like to acknowledge Hans Blom and Prof. Jerker Widengren at KTH, Stockholm, for assisting the cross-correlation measurements and for numerous discussions and improvements of this work. Many thanks go to Christian Eggeling at MPI, Göttingen, for analyzing the cross-correlation data and for the effort spent in the 2D-FIDA evaluation. I am grateful to Herbert Gross of Carl Zeiss, Oberkochen, for many valuable comments and discussions on the calculation of optical fields.

I am in dept of Rudolf Robelek and Eva-Kathrin Sinner for generously contributing the membrane protein chemistry and for assisting in preparing the measurements. I would like to thank the Laboratory of Physical Chemistry of Polymers and Membranes (LCPM) at EPFL for their generous support in evaporating the chromium and gold layers. Special thanks go to Samuel Terrettaz and Pedro Pascoal, who received me always with a smile whenever I had questions. I thank André Galliker, Lot-Oriel, for support with the ultra-sensitive EMCCD camera and Carolyn Yong, Laboratory for MechanoBiology and Morphogenesis (LMBM) at EPFL, for the opportunity of "dumping" samples in the -80°C freezer. I would like to express my gratitude to Matthias Geissbühler and Joseph Lasser for putting so much effort in the data analysis.

Many thanks go to all members of the Laboratoire d'Optique Biomédicale (LOB) for the nice time we had in the lab and abroad. Antonio Lopez for organizing "before-sunrise skiing events" and Adrian Bachmann for co-organizing several lab excursions. I would like to thank Prof. Rainer A. Leitgeb and Prof. Rudolf Rigler for many expert discussions on optics and FCS and Iwan Märki and Erica J. Martin-Williams for the proofreading. I am in particular in dept of our secretary Judith Chaubert and Yvette Bernhard, who helped me out with a lot of administrative tasks.

My kindest regards go to Adrian von Mühlénen, Marc and Ursula Lippuner and Matthias Meier, who offered me good opportunities to escape the lab and visit old friends. Last but not least, I would like to thank all my friends, my parents and my relatives for their interest and support.

The support of the Swiss National Science Foundation (SNSF) (contract number 200021-103333) and the European Commission (FuSyMEM project, 6th Framework Programme) is greatly acknowledged.

References

1. J. R. Lakowicz, H. Szymanski, K. Nowaczyk, K. W. Berndt, M. Johnson, "Fluorescence lifetime imaging," *Anal. Biochem.* **202**, 316–330 (1992).
2. T. W. J. Gadella, T. M. Jovin, R. M. Clegg, "Fluorescence lifetime imaging microscopy (FLIM) - Spatial-resolution of microstructures on the nanosecond time-scale," *Biophys. Chem.* **48**, 221–239 (1993).
3. X. S. Xie, R. C. Dunn, "Probing single-molecule dynamics," *Science* **265**, 361–364 (1994).
4. D. Magde, W. W. Webb, E. Elson, "Thermodynamic fluctuations in a reacting system - measurement by fluorescence correlation spectroscopy," *Phys. Rev. Lett.* **29**, 705 (1972).
5. R. Rigler, E. S. Elson, *Fluorescence Correlation Spectroscopy: Theory and Applications*, Springer Ser. Chem. Phys. **65**, Berlin Heidelberg, Germany (2001).
6. Y. Chen, J. D. Müller, P. T. C. So, E. Gratton, "The Photon Counting Histogram in Fluorescence Fluctuation Spectroscopy," *Biophys. J.* **77**, 553–567 (1999).
7. P. Kask, K. Palo, D. Ullmann, K. Gall, "Fluorescence-intensity distribution analysis and its application in biomolecular detection technology," *PNAS* **96**, 13756–13761 (1999).
8. H. P. Kao, J. R. Abney, A. S. Verkman, "Determinants of the translational mobility of a small solute in cell cytoplasm," *J. Cell Biol.* **120**, 175–184 (1993).
9. N. O. Petersen, C. Brown, A. Kaminski, J. Rocheleau, M. Srivastava, P. W. Wiseman, "Analysis of membrane protein cluster densities and sizes *in situ* by image correlation spectroscopy," *Faraday Discuss.* **111**, 289–305 (1998).
10. C. Eggeling, P. Kask, D. Winkler, S. Jäger, "Rapid Analysis of Förster Resonance Energy Transfer by Two-Color Global Fluorescence Correlation Spectroscopy: Trypsin Proteinase Reaction," *Biophys. J.* **89**, 605–618 (2005).
11. C. Eggeling, S. Berger, L. Brand, J. R. Fries, J. Schaffer, A. Volkmer, C. A. M. Seidel, "Data registration and selective single-molecule analysis using multi-parameter fluorescence detection," *J. Biotech.* **86**, 163–180 (2001).
12. E. B. Shera, N. K. Seitzinger, L. M. Davis, R. A. Keller, S. A. Soper, "Detection of single fluorescent molecules," *Chem. Phys. Lett.* **174**, 553–557 (1990).
13. M. Eigen, R. Rigler, "Sorting single molecules - application to diagnostics and evolutionary biotechnology," *PNAS* **91**, 5740–5747 (1994).
14. R. Rigler, Ü. Mets, J. Widengren, P. Kask, "Fluorescence correlation spectroscopy with high count rate and low background - analysis of translational diffusion," *Eur. Biophys. J. Biophys. Lett.* **22**, 169–175 (1993).
15. P. S. Dittrich, B. Müller, P. Schwille, "Studying reaction kinetics by simultaneous FRET and cross-correlation analysis in a miniaturized continuous flow reactor," *Phys. Chem. Chem. Phys.* **6**, 4416–4420 (2004).
16. M. R. Pinto, K. S. Schanze, "Amplified fluorescence sensing of protease activity with conjugated polyelectrolytes," *PNAS* **101**, 7505–7510 (2004).
17. E. J. G. Peterman, H. Sosa, W. E. Moerner, "Single-molecule fluorescence spectroscopy and microscopy of biomolecular motors," *Ann. Rev. Phys. Chem.* **55**, 79–96 (2004).
18. K. Bacia, I. V. Majoul, P. Schwille, "Probing the endocytic pathway in live cells using dual-color fluorescence cross-correlation analysis," *Biophys. J.* **83**, 1184–1193 (2002).
19. S. Weiss, "Fluorescence Spectroscopy of Single Biomolecules," *Science* **283**, 1676–1683 (1999).
20. O. Krichevsky, G. Bonnet, "Fluorescence correlation spectroscopy: the technique and its applications," *Rep. Prog. Phys.* **65**, 251–297 (2002).

21. T. Wazawa, M. Ueda, "Total internal reflection fluorescence microscopy in single molecule nanobioscience," *Microsc. Tech. Adv. Biochem. Eng. / Biotech.* **95**, 77–106 (2005).
22. K. Hassler, T. Anhut, R. Rigler, M. Gösch, T. Lasser, "High Count Rates with Total Internal Reflection Fluorescence Correlation Spectroscopy," *Biophys. J.* **88**, L1–L3 (2005).
23. T. Ruckstuhl, S. Seeger, "Attoliter detection volumes by confocal total-internal-reflection fluorescence microscopy," *Opt. Lett.* **29**, 569–571 (2004).
24. L. Kastrup, H. Blom, C. Eggeling, S. W. Hell, "Fluorescence fluctuation spectroscopy in subdiffraction focal volumes," *Phys. Rev. Lett.* **94**, 178104 (2005).
25. M. J. Levene, J. Korlach, S. W. Turner, M. Foquet, H. G. Craighead, W. W. Webb, "Zero-Mode Waveguides for Single-Molecule Analysis at High Concentrations," *Science* **299**, 682–686 (2003).
26. M. Foquet, J. Korlach, W. R. Zipfel, W. W. Webb, H. G. Craighead, "Focal volume confinement by submicrometer-sized fluidic channels," *Anal. Chem.* **76**, 1618–1626 (2004).
27. K. Hassler, "Single molecule detection and fluorescence correlation spectroscopy on surfaces," EPFL thesis no. 3433 (2005), <http://library.epfl.ch/en/theses/?nr=3433>.
28. A. M. Lieto, R. C. Cush, N. L. Thompson, "Ligand-Receptor Kinetics Measured by Total Internal Reflection with Fluorescence Correlation Spectroscopy," *Biophys. J.* **85**, 3294–3302 (2003).
29. K. Kneipp, H. Kneipp, J. Kneipp, "Surface-enhanced Raman scattering in local optical fields of silver and gold nanoaggregates - From single-molecule Raman spectroscopy to ultrasensitive probing in live cells," *Acc. Chem. Res.* **39**, 443–450 (2006).
30. H. Rigneault, J. Capoulade, J. Dintinger, J. Wenger, N. Bonod, E. Popov, T. W. Ebbesen, P.F. Lenne, "Enhancement of Single-Molecule Fluorescence Detection in Subwavelength Apertures," *Phys. Rev. Lett.* **95**, 117401 (2005).
31. C. Girard, O. J. F. Martin, G. Lévêque, G. Colas des Francs, A. Dereux, "Generalized Bloch equations for optical interactions in confined geometries," *Chem. Phys. Lett.* **404**, 44–48 (2005).
32. J. R. Lakowicz, *Principles of fluorescence spectroscopy*, 3rd ed., Springer, New York, ISBN 978-0-387-31278-1 (2006).
33. H. Gratz, A. Penzkofer, C. Abels, R.-M. Szeimies, M. Landthaler, W. Bäuml, "Photo-isomerisation, triplet formation, and photo-degradation dynamics of indocyanine green solutions," *J. Photochem. Photobiology A: Chem.* **128**, 101–109 (1999).
34. C. Eggeling, J. Widengren, R. Rigler, et al., "Photobleaching of fluorescent dyes under conditions used for single-molecule detection: Evidence of two-step photolysis," *Anal. Chem.* **70**, 2651–2659 (1998).
35. W. Holzer, H. Gratz, T. Schmitt, A. Penzkofer, A. Costela, I. García-Moreno, R. Sastre, F. J. Duarte, "Photophysical characterization of rhodamine 6G in a 2-hydroxyethyl-methacrylate methyl-methacrylate copolymer," *Chem. Phys.* **256**, 125–136 (2000).
36. J. Widengren, A. Chmyrov, C. Eggeling, P. A. Lofdahl, C. A. M. Seidel, "Strategies to improve photostabilities in ultrasensitive fluorescence spectroscopy," *J. Phys. Chem. A* **111**, 429–440 (2007).
37. T. G. Pavlopoulos, D. J. Golich, "Triplet extinction coefficients of some laser dyes I," *J. Appl. Phys.* **64**, 521–527 (1988).
38. T. G. Pavlopoulos, D. J. Golich, "Triplet extinction coefficients of some laser dyes II," *J. Appl. Phys.* **67**, 1203–1209 (1990).
39. H. Gratz, A. Penzkofer, "Triplet–triplet absorption of some organic molecules determined by picosecond laser excitation and time-delayed picosecond light continuum probing," *J. Photochem. Photobiol. A: Chem.* **127**, 21–30 (1999).
40. W. Lukosz, R. E. Kunz, "Light-emission by magnetic and electric dipoles close to a plane interface: 1. Total radiated power," *J. Opt. Soc. Am.* **67**, 1607–1615 (1977).
41. W. Lukosz, "Light-emission by magnetic and electric dipoles close to a plane dielectric interface: 3. Radiation-patterns of dipoles with arbitrary orientation," *J. Opt. Soc. Am.* **69**, 1495–1503 (1979).

42. T. P. Burghardt, N. L. Thompson, "Effect of planar dielectric interfaces on fluorescence emission and detection. Evanescent excitation with high-aperture collection," *Biophys. J.* **46**, 729–737 (1984).
43. E. H. Hellen, D. Axelrod, "Fluorescence emission at dielectric and metal-film interfaces," *J. Opt. Soc. Am. B* **4**, 337–350 (1987).
44. L. Novotny, "Allowed and forbidden light in near-field optics. II. Interacting dipolar particles," *J. Opt. Soc. Am. A* **14**, 105–113 (1997).
45. J. Mertz, "Radiative absorption, fluorescence, and scattering of a classical dipole near a lossless interface: a unified description," *J. Opt. Soc. Am. B* **17**, 1906–1913 (2000).
46. G. W. Ford, W. H. Weber, "Electromagnetic interactions of molecules with metal surfaces," *Phys. Rep.* **113**, 195–287 (1984).
47. K. Vasilev, W. Knoll, M. Kreiter, "Fluorescence intensities of chromophores in front of a thin metal film," *J. Chem. Phys.* **120**, 3439–3445 (2004).
48. F. D. Stefani, K. Vasilev, N. Bocchio, N. Stoyanova, M. Kreiter, "Surface-plasmon-mediated single-molecule fluorescence through a thin metallic film," *Phys. Rev. Lett.* **94**, 023005 (2005).
49. R. J. Potton, "Reciprocity in optics," *Rep. Prog. Phys.* **67**, 717–754 (2004).
50. J.-L. Kaiser, E. Quertemont, R. Chevallier, "Light propagation in the pseudo-paraxial Fresnel approximation," *Opt. Comm.* **233**, 261–269 (2004).
51. A. E. Siegman, *Lasers*, Oxford Univ. Press, ISBN 0-19-855713-2 (1986).
52. D. Mas, J. Garcia, C. Ferreira, L. M. Bernardo, F. Marinho, "Fast algorithms for free-space diffraction patterns calculation," *Opt. Comm.* **164**, 233–245 (1999).
53. J. Widengren, Ü. Mets, R. Rigler, "Fluorescence correlation spectroscopy of triplet states in solution: A theoretical and experimental study," *J. Phys. Chem.* **99**, 13368–13379 (1995).
54. J. Widengren, P. Schwille, "Characterization of Photoinduced Isomerization and Back-Isomerization of the Cyanine Dye Cy5 by Fluorescence Correlation Spectroscopy," *J. Phys. Chem. A* **104**, 6416–6428 (2000).
55. T. Wohland, R. Rigler, H. Vogel, "The standard deviation in fluorescence correlation spectroscopy," *Biophys. J.* **80**, 2987–2999 (2001).
56. P. Kask, K. Palo, N. Fay, L. Brand, Ü. Mets, D. Ullmann, J. Jungmann, J. Pschorr, K. Gall, "Two-Dimensional Fluorescence Intensity Distribution Analysis: Theory and Applications," *Biophys. J.* **78**, 1703–1713 (2000).
57. P. Schwille, F.-J. Meyer-Almes, R. Rigler, "Dual-Color Fluorescence Cross-Correlation Spectroscopy for Multicomponent Diffusional Analysis in Solution," *Biophys. J.* **72**, 1878–1886 (1997).
58. C. Eggeling, J. Widengren, L. Brand, J. Schaffer, S. Felekyan, C. A. M. Seidel, "Analysis of photobleaching in single-molecule multicolor excitation and Förster resonance energy transfer measurements," *J. Phys. Chem. A* **110**, 2979–2995 (2006).
59. B. K. Muller, E. Zaychikov, C. Brauchle, D. C. Lamb, "Pulsed interleaved excitation," *Biophys. J.* **89**, 3508–3522 (2005).
60. R. Erdmann, J. Enderlein, M. Wahl, *Time correlated single-photon counting and fluorescence spectroscopy*, Wiley, ISBN 3-527-40442-2 (2005).
61. R. Robelek, F. D. Stefani, W. Knoll, "Oligonucleotide hybridization monitored by surface plasmon enhanced fluorescence spectroscopy with bio-conjugated core/shell quantum dots. Influence of luminescence blinking," *phys. stat. sol. (a)* **203**, 3468–3475 (2006).
62. R. Robelek, E. S. Lemker, B. Wiltschi, V. Kirste, R. Naumann, D. Oesterheld, E.-K. Sinner, "Incorporation of *In Vitro* Synthesized GPCR into a Tethered Artificial Lipid Membrane System," *Angew. Chem. Int. Ed.* **46**, 605–608 (2007).
63. S. Heyse, O. P. Ernst, Z. Dienes, K. P. Hofmann, H. Vogel, "Incorporation of Rhodopsin in Laterally Structured Supported Membranes: Observation of Transducin Activation with Spatially and Time-Resolved Surface Plasmon Resonance," *Biochem.* **37**, 507–522 (1998).

64. C. Bieri, O. P. Ernst, S. Heyse, K. P. Hofmann, H. Vogel, "Micropatterned immobilization of a G protein-coupled receptor and direct detection of G protein activation," *Nature Biotech.* **17**, 1105–1108 (1999).
65. Y. Lill, K. L. Martinez, M. A. Lill, B. H. Meyer, H. Vogel, B. Hecht, "Kinetics of the initial steps of G protein-coupled receptor-mediated cellular signaling revealed by single-molecule imaging," *ChemPhysChem* **6**, 1633–1640 (2005).
66. N. Kahya, P. Schwille, "Fluorescence correlation studies of lipid domains in model membranes (Review)," *Mol. Membr. Biol.* **23**, 29–39 (2006).
67. V. Jacquier, M. Prummer, J.-M. Segura, H. Pick, H. Vogel, "Visualizing odorant receptor trafficking in living cells down to the single-molecule level," *PNAS* **103**, 14325–14330 (2006).
68. J.-B. Perez, J.-M. Segura, D. Abankwa, J. Piguet, K. L. Martinez, H. Vogel, "Monitoring the diffusion of single heterotrimeric G proteins in supported cell-membrane sheets reveals their partitioning into microdomains," *J. Mol. Biol.* **363**, 918–930 (2006).
69. B. Wiltschi, W. Knoll, E.-K. Sinner, "Binding assays with artificial tethered membranes using surface plasmon resonance," *Methods* **39**, 134–146 (2006).
70. N. O. Petersen, C. Brown, A. Kaminski, J. Rocheleau, M. Srivastava, P. W. Wiseman, "Analysis of membrane protein cluster densities and sizes *in situ* by image correlation spectroscopy," *Faraday Discuss.* **111**, 289–305 (1998).
71. A. G. Benn, R. J. Kulperger, "Statistical inference for a Poisson process model of scanning fluorescence correlation spectroscopy," *Environmetrics* **7**, 167–183 (1996).
72. D. Marr, E. Hildreth, "Theory on edge detection," *Proc. R. Soc. Lond. B* **207**, 187–217 (1980).

Appendix A

Rate equations governing fluorescence

Here, the n -state model is approximated with a three-state model taking into account the ground state S_0 , the excited state S_1 and the triplet state T_1 . P_{ss} denotes the occupation probability of the electronic state ss and $R_{xx} = P_{ss}/\tau_{xx}$ the transition rate per molecule. The following rate equations describe then the evolution of the occupation probabilities.

$$\frac{d}{dt}P_{S_0} = \frac{P_{S_1}}{\tau_{fl}} + \frac{P_{S_1}}{\tau_{nr}} + \frac{P_{T_1}}{\tau_{T_1}} - \frac{P_{S_0}}{\tau_{ex}} \quad (\text{A.1})$$

$$\frac{d}{dt}P_{S_1} = \frac{P_{S_0}}{\tau_{ex}} - \frac{P_{S_1}}{\tau_{S_1}} \quad (\text{A.2})$$

$$\frac{d}{dt}P_{T_1} = \frac{P_{S_1}}{\tau_{isc}} - \frac{P_{T_1}}{\tau_{T_1}} \quad (\text{A.3})$$

$$\sum_{ss} P_{ss} = 1 \quad (\text{A.4})$$

The singlet lifetime τ_{S_1} is

$$\tau_{S_1} = \left(\frac{1}{\tau_{fl}} + \frac{1}{\tau_{nr}} + \frac{1}{\tau_{isc}} \right)^{-1}. \quad (\text{A.5})$$

In a dynamic equilibrium at constant excitation rate, the variations of the occupation probabilities vanish. Solving for the occupation probability P_{S_1} yields the average rate of fluorescence emissions per molecule.

$$R_{fl} = \frac{1}{\tau_{fl}} \left(1 + \frac{\tau_{T_1}}{\tau_{isc}} + \frac{\tau_{ex}}{\tau_{S_1}} \right)^{-1} = \frac{q_{fl}}{\tau_{ex} + \tau_{S_1} + q_{isc}\tau_{T_1}} \quad (\text{A.6})$$

$q_{fl} = \tau_{S_1}/\tau_{fl}$ is the fluorescence quantum yield and $q_{isc} = \tau_{S_1}/\tau_{isc}$ is the intersystem crossing probability. The denominator $\tau_{ex} + \tau_{S_1} + q_{isc}\tau_{T_1}$ corresponds to the average cycle time. The occupation probability of the triplet state is given by

$$P_{T_1} = \left(1 + \frac{\tau_{isc}}{\tau_{T_1}} \left(1 + \frac{\tau_{ex}}{\tau_{S_1}} \right) \right)^{-1} = \frac{q_{isc}\tau_{T_1}}{\tau_{ex} + \tau_{S_1} + q_{isc}\tau_{T_1}}. \quad (\text{A.7})$$

The limits of (A.6) and (A.7) for strong excitation (e.g. $\tau_{ex} \rightarrow 0$) are

$$\lim_{I_{ex} \rightarrow \infty} R_{fl} = R_{fl,max} = \frac{1}{\tau_{fl}} \left(1 + \frac{\tau_{T_1}}{\tau_{isc}} \right)^{-1} \quad \text{and} \quad (\text{A.8})$$

$$\lim_{I_{ex} \rightarrow \infty} P_{T_1} = P_{T_1,max} = \left(1 + \frac{\tau_{isc}}{\tau_{T_1}} \right)^{-1}. \quad (\text{A.9})$$

The saturation limit is defined by $P_{S_0} = 50\%$ where $R_{fl} = R_{fl,max}/2$, which corresponds to $\tau_{ex} = \tau_{S_1} + q_{isc}\tau_{T_1}$ and

$$I_{ex,sat} = \frac{\hbar\omega_{ex}}{\sigma_{ex}\tau_{S_1}} \left(1 + \frac{\tau_{T_1}}{\tau_{isc}} \right)^{-1}, \quad \text{respectively.} \quad (\text{A.10})$$

Part II

Articles

Single Molecule Detection at Surfaces

Dual-color Fluorescence Fluctuation Spectroscopy with Total Internal Reflection Excitation

M. Leutenegger¹, K. Hassler^{1,2}, P. Rigler³, A. Bilenca⁴, T. Lasser¹

¹Laboratoire d'Optique Biomédicale, École Polytechnique Fédérale de Lausanne, Lausanne, Switzerland

²Biomolekylär Fysik, Kungliga Tekniska Högskolan, Stockholm, Sweden

³Department of Chemistry, Universität Basel, Basel, Switzerland

⁴Harvard Medical School and Wellman Center for Photomedicine, Massachusetts General Hospital, Boston, MA 02114

Fluorescence fluctuation spectroscopy based on an evanescent field excitation scheme leads to an alternative concept for single molecule detection with interesting experimental features. This concept is described and analyzed regarding the total fluorescence process including excitation, fluorescence emission and collection close to a dielectric interface. The realized experimental scheme showed superior performance of this concept with substantially enhanced molecular brightness when compared to the classical confocal setup based on water immersion objectives. Selected applications in life sciences including dual-color surface fluorescence correlation spectroscopy, enzyme kinetics and receptor–ligand binding are underlining the interest of this experimental approach.

Introduction

Fluorescence fluctuation spectroscopy (FFS) is a general designation for the observation of the fluorescence process at the single molecule level. A well-known technique for single molecule detection is fluorescence correlation spectroscopy (FCS), which was conceived to study kinetic and dynamic processes through the statistical analysis of fluctuations at thermodynamic equilibrium (*1*). The temporal correlation of the photon emission trace of a molecular system (generally a biomolecule specifically labeled with a fluorophore) allows accessing the characteristic rates and velocities of the underlying molecular system. With an appropriate model of the molecular system, these characteristic rates and velocities can be extracted. For example, fluctuations in the number of few fluorescent particles unravel the diffusion dynamics within a highly confined sampling volume.

The principal concept was already described in the early 70's by the first paper on this topic by Magde et al. (2). A real renaissance arrived in 1993 with the introduction of the confocal illumination scheme for FCS by Rigler et al. (3). Since then FCS has been developed towards probably the most important technique for single molecule detection (SMD). FCS allows measuring rates of binding/unbinding reactions (4, 5), coefficients of translational and rotational diffusion (6, 7, 8, 9), conformational states and a manifold of photophysical parameters (10, 11, 12) of the induced fluorescent process.

For FFS the confocal illumination scheme led to a highly confined excitation and detection volume. Alternative optical schemes for confining the excitation volume, for instance evanescent field excitation, were demonstrated already in the 80's (13, 14). However, they did not show a performance comparable to confocal FFS for single molecule detection.

In this contribution, we summarize and present numerous recent results of total internal reflection FCS, i.e. single molecule detection in the proximity of dielectric surfaces, emphasizing interesting features which overcome the past limitations of evanescent field FCS (15, 16). First, we outline the general aspects of FFS for SMD and describe the essential steps of a FFS measurement. In the following, a novel dual-color setup for SMD at surfaces is presented (17). This setup enables high photon count rates per molecule well beyond count rates known from classical excitation schemes. Finally, we demonstrate this concept on selected biological applications, such as enzymatic catalysis and monitoring of membrane embedded proteins.

The fluorescence fluctuation process

FFS applied to SMD involves recording and analyzing traces of emitted fluorescence photons emanating from a tiny probe volume. Figure 1 outlines the instrumental chain including the molecular fluorescence process as happening in a typical SMD experiment. The excitation light at wavelength λ_{ex} is tightly focused into the sample and generates a highly confined excitation volume as indicated in figure 1d in solid-line ellipse. Fluorescently labeled biomolecules diffusing through this confined light field are excited and emit photons at a wavelength $\lambda_{fl} > \lambda_{ex}$. These fluorescence photons are partly gathered by the collection optics. A dielectric band-pass filter rejects residual excitation light and suppresses Raman scattered light contributions.¹

The fluorescence photons are focused onto the pinhole rejecting stray and out-of-focus light. The pinhole and the collection optics determine the detection volume as indicated in figure 1d in dashed-line ellipse. For optimum FFS measurements, the excitation and detection volume must be perfectly matched, i.e. the pinhole must be in a conjugated position to the excitation volume. The diameter of the pinhole determines the lateral extent of the detection volume and is chosen according to the criteria of diffraction-limited imaging.

The single photon detector – typically an avalanche photo diode (APD) driven in counting mode – detects the arrival of fluorescence photons. The recorded photon trace is finally evaluated according to the chosen FFS method, i.e. the sequence of detection events is numerically processed for yielding information about the investigated sample.

FFS retrieves essential information about biomolecules by analyzing the fluctuations of the fluorescence intensity $I(t)$ during a short time interval T . Typical sources for these fluctuations are particle motions through the sampling volume via diffusion and flow, the stochastic nature of the

¹ Raman scattering of individual particles is many orders of magnitude weaker than fluorescence. However, the high solvent concentration (55M for water) largely compensates this low efficiency, making Raman scattering one of the most important background sources.

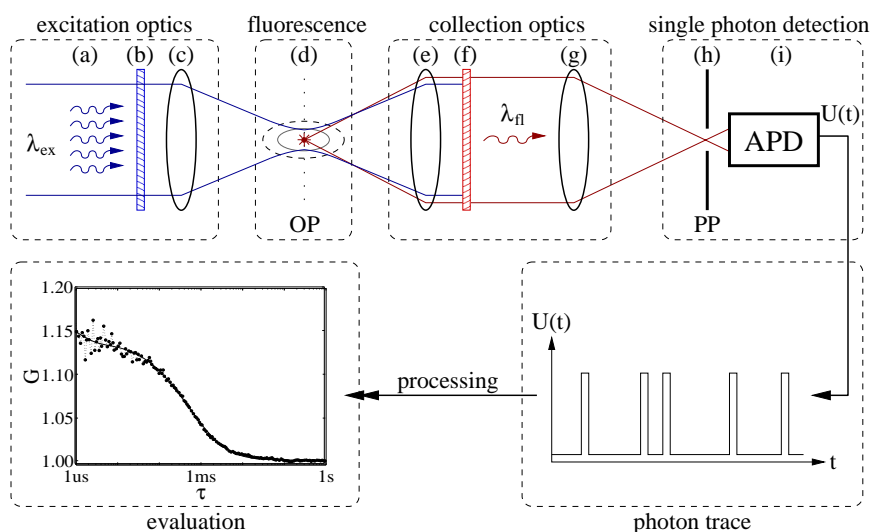


Figure 1: Overview of FFS methods for single molecule detection. OP: object plane, PP: conjugated pinhole plane. (a) Excitation light, (b) excitation band-pass filter, (c) focusing optics, (d) excitation (solid line) and detection (dashed line) volumes, (e) collection optics, (f) emission band-pass filter, (g) tube lens, (h) pinhole, (i) single photon detector.

photophysical response of the fluorophores, for instance singlet or triplet transitions, and variations of the quantum yield with the molecular environment or binding/unbinding reactions.

A low number of particles within the sampling volume causes high relative fluctuations of the fluorescence intensity rendering FFS measurements more robust. Therefore, a very small excitation volume is required, which is normally achieved with a high numerical aperture (NA) objective. Excitation volumes as low as $V_{ex} \approx 0.3\text{fl}$ are not uncommon for measuring particle concentrations in the range up to $\approx 100\text{nM}$.

The fluorescence emission of individual fluorophores is very weak. Consequently, the collection optics should capture as much fluorescence photons as possible, which demands the use of high NA optics. Furthermore, since the fluorescence intensity is typically 8 to 10 orders of magnitude weaker than the excitation intensity, dichroic filters must block the excitation light by at least 9 to 11 orders of magnitude for obtaining a good signal to noise ratio (SNR). An excitation band-pass filter is used in front of the focusing optics for achieving a spectrally pure excitation, which is subsequently blocked efficiently by a complementary emission band-pass filter.

In summary, FFS relies on instrumental features, such as the generation of a confined sampling volume, the high collection efficiency of the observation system, the detection of single photons, the processing of these photon events as well as the stochastic characteristics of the investigated molecular system.

In the following sub-section, we describe, compare and analyze in detail the sampling volume, in particular for an evanescent field excitation. The dipole response and its interaction with a dielectric substrate within the framework of the molecule detection efficiency will be considered in detail as a relevant model for the overall FFS process. Finally, fluorescence correlation spectroscopy (FCS) as a prominent member of FFS techniques will be described in the context of SMD.

Molecule detection efficiency and confined sampling volume

The analysis and interpretation of the fluctuation statistics obtained with FFS measurements requires knowledge of the excitation and detection volume and the detected fluorescence brightness profile, i.e. the molecule detection efficiency (MDE) of the fluorescent particle at position \vec{r} . The brightness $Q(\vec{r})$ of a single fluorophore is determined by its photophysical properties, the excitation intensity $\Phi(\vec{r})hc/\lambda_{ex}$ (where $\Phi(\vec{r})$ is the excitation photon flux, h Planck's constant, c the speed of light and λ_{ex} the excitation wavelength), the collection efficiency $C(\vec{r})$ and the pinhole transmission efficiency $T(\vec{r})$.²

The fluorophore's brightness is given by

$$Q(\vec{r}) = q_d R_{fl}(\vec{r}) C(\vec{r}) T(\vec{r}) \quad (1)$$

with q_d being the detection quantum yield.³ $R_{fl}(\vec{r})$ describes the average fluorescence emission rate and is expressed as

$$R_{fl}(\vec{r}) = \frac{q_{fl}(\vec{r})}{\tau_{ex}(\vec{r}) + \tau_S(\vec{r}) + q_{isc}(\vec{r})\tau_T(\vec{r})} \quad (2)$$

where q_{fl} is the fluorescence quantum yield, τ_{ex} the average excitation time, τ_S the excited state lifetime, q_{isc} the transition probability of the singlet-triplet intersystem crossing, and τ_T the triplet state lifetime. Assuming fast rotation of the fluorophore, the absorption at λ_{ex} is isotropic and the excitation rate reads $\tau_{ex}^{-1} = \sigma_{abs}\Phi(\vec{r})$, with σ_{abs} representing the absorption cross-section at wavelength λ_{ex} . It is worth mentioning that the fluorophore's brightness $Q(\vec{r})$ saturates for high excitation intensities. Usually, the excitation intensity is kept in the linear regime (well below saturation); otherwise, saturation effects would introduce artifacts in the recorded photon traces.

In general, the fluorophore's brightness $Q(\vec{r})$ varies with position. Particularly, the fluorophore's photophysical parameters become distance-dependent near a surface, as the presence of the surface modifies the local density of states, and consequently also the transition rates between the fluorophore's electronic states (18, 19). Additionally, the proximity of the fluorophore to the dielectric surface, modeled as a dipole emitter close to a dielectric substrate (20, 21, 22), results in a deformation of the angular power density of the dipole emission, thus altering essentially the collection efficiency $CEF(\vec{r})$.

Figure 2 depicts the calculated radiation profile of a fluorophore at the coverslip-sample interface $z = 0$. The fluorophore is located at the origin of the coordinate system with a dipole moment $\vec{\mu}_0 \parallel (1, 0, 1)$. The polar plot indicates the anisotropic and asymmetric angular power density. Thin straight lines represent the critical angle of refraction in the coverslip ($z < 0$) and thick lines show the radiated power density in the $x = 0$ and $y = 0$ planes. For comparison, the power density of an identical dipole $\vec{\mu}_0$ in an isotropic environment is shown in thin lines.

In close vicinity to the coverslip, the dipole "senses" the higher refraction index of the coverslip and radiates power into the coverslip not only at sub-critical angles but also at super-critical angles. This effect stems from the evanescent coupling of the dipole's near field to propagating waves in the coverslip. The power radiated at super-critical angles significantly enhances the total power radiated into the coverslip. However, wave propagation in the sample space is diminished due to destructive interference between the direct radiation and the back-reflection at the interface.

² The pinhole transmission efficiency is frequently approximated by convolving the projected pinhole with the point-spread function of the collection optics. However, a complete wave-optical calculation has to account for the anisotropic emission of fluorophores close to a surface.

³ The product $C(\vec{r})T(\vec{r})$ is the so-called collection efficiency function $CEF(\vec{r})$.

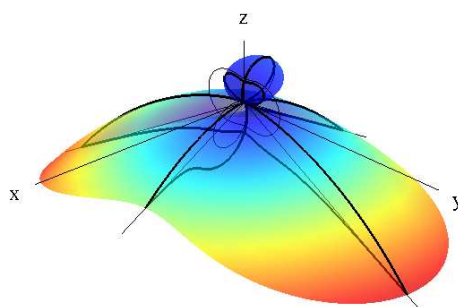


Figure 2: Anisotropic dipole radiation profile modeling a fluorophore at a glass–water interface. The critical angle is indicated by straight lines. Depending on distance and dipole orientation, this radiation profile shows a pronounced anisotropy and asymmetry.

Figure 3 compares the power collection efficiency of two optical collection schemes, system I, a trans-illumination scheme and system II, an epi-illumination scheme. The power collection

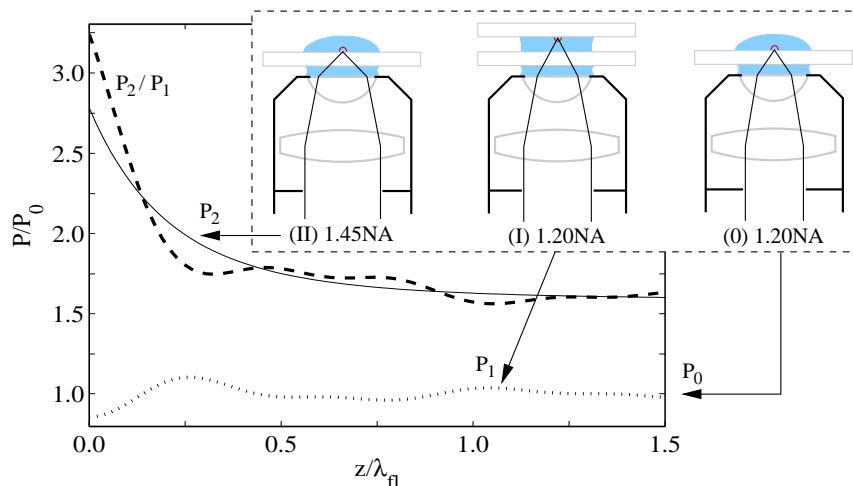


Figure 3: Collected power versus fluorophore position. The glass coverslip ($z < 0$) has a refraction index of 1.520 and the water sample 1.335, respectively. In the region of an evanescent excitation field ($z < \lambda_{ex}/3$), the trans-illumination setup I with a NA of 1.20 collects less power (dotted curve) than the epi-illumination reference system ($P_0 \equiv 1$), whereas the epi-illumination setup II with a NA of 1.45 collects two times more power (solid curve). The enhanced power collection of system II compared to system I is represented by the dashed curve.

efficiency is computed with respect to system 0 gathering the power P_0 from a randomly oriented fluorophore located at a distance $z > 0$ from a glass–water interface using a 1.20NA water immersion objective positioned at $z < 0$. The dotted line describes the fluorescence power P_1 collected by system I, consisting of a 1.20NA water immersion objective positioned at $z > 0$. The observed undulation stems from interference of direct and reflected fluorescence radiation at the interface. Note that this optical collection configuration is commonly employed in prism-based evanescent

field excitation setups (23). The solid curve shows the fluorescence power P_2 collected by system II comprising a 1.45NA oil immersion objective positioned at $z < 0$. The exponential decrease (up to $z \approx \lambda_{fl}$) results from the reduced coupling of the fluorophore emission located far from the interface. Finally, the enhancement factor P_2/P_1 is plotted in dashed line. It is notable that for $z < \lambda_{ex}/3$, the epi-illumination setup II achieves a two-fold increase in power collection efficiency compared to the trans-illumination setup I. This difference is caused by the increased radiation towards the coverslip and the high collection efficiency of the high NA objective collecting the substantial light contribution beyond the critical angle.

Figure 4 depicts brightness profiles $Q(\vec{r})$ of an evanescent field epi-illumination scheme employing a 1.45NA oil immersion objective focused at the glass–water interface at $z = 0$ (system II). Using Equation (1), the brightness calculations were performed assuming excitation and aver-

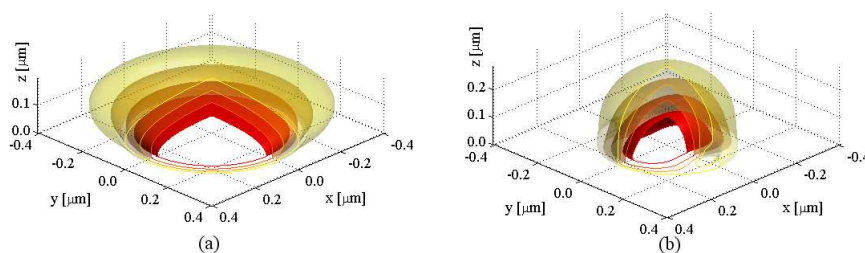


Figure 4: Brightness profiles $Q(\vec{r})$ at the coverslip–sample interface. The iso-surfaces $Q(\vec{r})$ equal e^{-1} , e^{-2} , e^{-3} and e^{-4} of the maximum brightness.

age emission wavelengths of $\lambda_{ex} = 488\text{nm}$ and $\bar{\lambda}_{fl} = 525\text{nm}$, respectively, and a projected pinhole diameter of $0.5\mu\text{m}$ at the glass–water interface. Figure 4a is computed for an evanescent field excitation on a circular area of $16\mu\text{m}$ diameter (c.f. figure 5a). This results in a cylindrical sampling volume of approximately $\pi(0.3\mu\text{m})^2 \cdot 0.1\mu\text{m}$. Figure 4b shows the calculations for a linearly polarized field focused to a diffraction-limited spot at the glass–water interface (c.f. figure 5b), resulting in a hemi-ellipsoidal sampling volume of $0.4\mu\text{m}$ and $0.3\mu\text{m}$ semi-axes and a z -axis dimension of $0.2\mu\text{m}$, respectively.

The effective sampling volume V_{eff} is determined by integrating $Q(\vec{r})$ over the entire volume (24, 25), that is

$$V_{eff} = \left(\iiint Q(\vec{r}) d\vec{r} \right)^2 / \iiint (Q(\vec{r}))^2 d\vec{r} \quad (3)$$

yielding 39al for total internal reflection (TIR) excitation and 22al for confocal excitation (26, 27, 28). For comparison, confocal excitation with a 1.20NA water immersion objective yields a sampling volume $V_{eff} \approx 250\text{al}$ in liquid. Therefore, FFS at the surface measures particle concentrations in the range up to $\approx 1\mu\text{M}$ instead of $\approx 100\text{nM}$ in liquid with state-of-the-art instrumentation.

Fluorescence correlation spectroscopy

In this sub-section, we introduce an important member of FFS, namely fluorescence correlation spectroscopy (FCS). FCS is based on the temporal intensity auto- or cross-correlation analyses of the photon traces (I). Whereas auto-correlations obtained from single photon traces yield information about particle mobility, particle concentration, as well as kinetics of other fluorescence fluctuation sources, cross-correlations computed using two photon traces provide information mainly

about correlated particle motions and binding kinetics. In coincidence studies, the auto- and cross-correlations are simultaneously measured, enabling, for example, the evaluation of the fraction of bound particles in binding/unbinding experiments. The temporal correlation function $G_{m \times n}(\tau)$ is given by

$$G_{m \times n}(\tau) = \frac{\langle I_m(t)I_n(t+\tau) \rangle}{\langle I_m(t) \rangle \langle I_n(t) \rangle} = (T - \tau) \frac{\int_0^{T-\tau} I_m(t)I_n(t+\tau) dt}{\int_0^{T-\tau} I_m(t) dt \cdot \int_{\tau}^T I_n(t) dt} \quad (4)$$

with τ being the lag time, T the measurement interval, and I_m and I_n the count rates (intensities) in the detection channels m and n , respectively. For example, $G_{A \times A}$ is the temporal auto-correlation of a single channel A, and $G_{A \times B}$ is the temporal cross-correlation between channels A and B.

It is important to point out that FFS methods assume that the observed process is stationary in time and position, i.e. at steady state.⁴ However, FFS experiments are usually carried out assuming that the process is *sufficiently* stationary in time that is the sample does not alter significantly during the measurement. Position stationarity is requested primarily if the observation point is scanned during the measurement.

Typically, parameterized model equations are used for describing the temporal correlations $G_{m \times n}(\tau)$. For instance, model equations of temporal auto-correlations are usually given by

$$G(\tau) = G_{\infty} + G_0 D(\tau) K(\tau) \left(1 + \frac{P_t}{1 - P_t} \exp\left(-\frac{\tau}{\tau_t}\right) \right) \quad (5)$$

where $G_{\infty} \approx 1$ is the correlation amplitude at infinite lag time and G_0 the amplitude of the particle motion. $D(\tau)$ represents diffusion/flow processes and $K(\tau)$ reads for kinetic processes (e.g. chemical reactions). Finally, P_t and τ_t are the triplet probability and the correlation time of the triplet state, respectively.

Dual-color total internal reflection FCS setup

Total internal reflection FCS proved to be a versatile tool for studying particle motion and photophysics on a single molecule level near a substrate. Its outstanding performance due to the fluorophore-substrate interaction makes epi-illumination TIR-FCS a method of choice for biologically driven applications at the surface, for instance, membrane studies and enzymatic reactions. Very recently, we proposed a new setup for dual-color TIR-FCS (16, 17).

Figure 5 outlines the dual-color epi-fluorescence setup allowing both TIR and confocal excitation. A 18mW HeNe laser (633nm: LHRP-1701, Laser 2000, Weßling, Germany) and a 22mW solid-state laser (488nm: Protera™ 488-15, Novalux, Sunnyvale, CA) provided two linearly polarized beams with 633nm and 488nm wavelength, respectively. These beams were expanded to an e^{-2} diameter of ≈ 2 mm and collinearly aligned to the microscope objective (BE & BS: 2.5 \times beam expanders & periscope beam steerers). The laser powers were controlled by neutral density filters. Laser-line clean-up filters (CF: Chroma⁵ Z488/10x (blue); Chroma Z633/10x (red)) assured spectrally pure excitations, which were combined by a dichroic mirror (BC: Chroma Z488bcm). An

⁴ It is assumed that the investigated sample is ergodic, i.e. the temporal average equals the ensemble (spatial) average.

⁵ Chroma Technology Corp., Brattleboro, VT

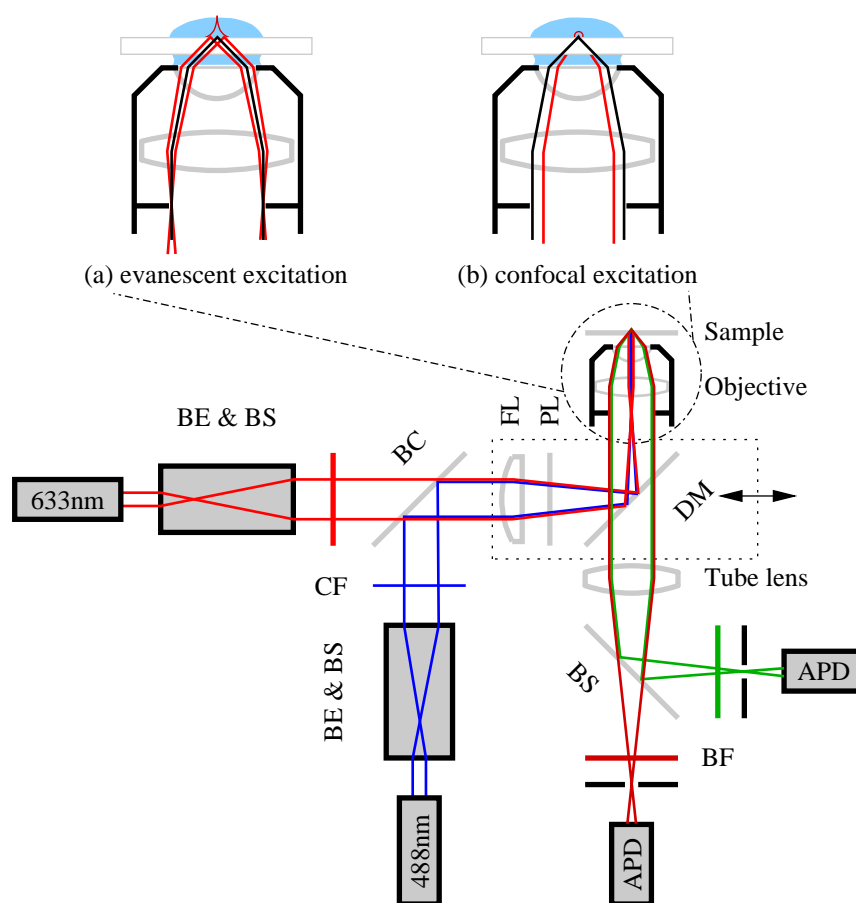


Figure 5: Dual-color TIR-FFS setup with confocal and evanescent epi-illumination at the coverslip-sample surface.

achromatic lens (FC: $f = 130\text{mm}$) focused the beams into the back-focal plane (BFP) of the high NA oil immersion objective (α -Plan-Fluar 100×1.45 with ImmersolTM 518F, Carl Zeiss Jena, Jena, Germany), which resulted in circular areas with e^{-2} diameters of $\approx 16\mu\text{m}$ (blue) and $\approx 20\mu\text{m}$ (red) at the coverslip-sample interface, respectively. In the BFP, a lateral beam focus offset of $\approx 2.3\text{mm}$ resulted in a super-critical angle illumination, i.e. in an evanescent field excitation. The sample was a droplet (containing biomolecules in low concentration) on a $150\mu\text{m}$ thick glass coverslip mounted on a xyz -translation stage (ULTRAlign 561D with μDrive Controller ESA-C, Newport Corp., Darmstadt, Germany).

In this epi-illumination setup, the fluorescent light was collected with the same high NA objective, focused onto the pinholes and detected via the single photon detectors. The pinholes were realized by two multimode fibers with a core diameter of $50\mu\text{m}$ (ASY50/105 silica fibers, Thorlabs Inc., Grünberg, Germany). A dichroic mirror (BS: Omega⁶ DML625) separated the green and red fluorescence light, whereas the combination of the main dichroic mirror and band-pass filters (BF: Chroma HQ540/80m and Omega 520DF40 (green); Chroma HQ690/80m and Omega 685DF70

⁶ Omega Optical Inc., Brattleboro, V

(red)) blocked the back-reflected laser light by more than 10 orders of magnitude. The fluorescence light was detected by fiber-coupled single photon counting modules (APD: SPCM-AQR-14-FC, PerkinElmer Optoelectronics, Wiesbaden, Germany), whose signals were recorded and correlated with a USB hardware correlator (Flex02-08D, Correlator.com, Bridgewater, NJ) linked to a standard PC. Within this setup, the focusing lens, the $\lambda/4$ plate (PL: OWIS, Staufen, Germany) and the main dichroic mirror (DM: Omega DM488/633) combination was laterally shifted by a linear translator, thereby positioning the beam foci off-axis in the BFP of the objective. This allows an independent excitation angle adjustment while keeping the beams focused on the BFP of the objective. As already mentioned, the configuration can easily be changed to a confocal epi-illumination by removing the focusing lens and by centering the collimated beams in the BFP.

Applications from photophysics to life sciences

Single molecule coincidence assay measured with dual-color TIR-FCS

A synthetic binding assay based on free Rhodamine Green (RhG), Cyanine5 (Cy5) fluorophores and a 40mer double-stranded desoxyribonucleic acid (dsDNA) labeled with Alexa488 and Cy5 (Zeiss cross-correlation standard) was investigated using the dual-color TIR-FCS system (17). The laser settings were optimized with the dsDNA sample, whereas the background was measured using a NaCl/EDTA/TRIS pH 8.0 buffer. Different mixtures of the double-labeled dsDNA solution with a solution of 9nM RhG / 50nM Cy5 were investigated and measured during 20s. Plasma cleaning of the coverslips was found to be a necessary processing step and improved the SNR due to a strong suppression of unspecific binding at the glass surface.

The amplitudes of the experimental auto-correlation curves were corrected for afterpulsing and for background to avoid systematic biases (28). The following model equation was used for the FCS analysis of these three diffusing species:

$$G_{mn}(\tau) = G_{mn\infty} + \frac{1}{2} \left(1 - \frac{B_m}{I_m}\right) \left(1 - \frac{B_n}{I_n}\right) \frac{\sum Q_{mi} Q_{ni} N_i D_{mni}(\tau)}{\sum Q_{mi} N_i \cdot \sum Q_{ni} N_i} + G_{mni} \exp\left(-\frac{\tau}{\tau_{mni}}\right) \quad (6)$$

Here, indices m and n represent the green and red detection channels; hence, G_{gg} and G_{rr} are the auto-correlations and G_{gr} the cross-correlation. B is the average background count rate and I the average total count rate. B and I were used for background correction of the diffusion amplitude. The index i represents the diffusing species: g for RhG, r for Cy5 and c for the dsDNA. Q_{mi} is the average brightness in channel m of species i , N_i are the average number of molecules in the sampling volumes. $Q_{mi} Q_{ni} N_i$ is the joint count rate of species i in both detection channels, whereas $Q_{mi} N_i$ and $Q_{ni} N_i$ are the count rates in either channel. G_{mni} and τ_{mni} are the amplitudes and the correlation times of photophysical relaxations, such as triplet state population or isomerization. It was assumed that τ_{mni} is much shorter than the diffusion times, which allows writing the triplet contribution as an additional term, thus simplifying the model. D_{mni} describes the diffusion and is given by

$$D_{mni}(\tau) = \left(1 + \frac{\tau}{\tau_{ixy}}\right)^{-1} \left(\sqrt{\frac{\tau}{\pi\tau_{iz}}} + \left(1 - \frac{\tau}{2\tau_{iz}}\right) \operatorname{erfcx}\left(\sqrt{\frac{\tau}{4\tau_{iz}}}\right)\right) \quad (7)$$

where τ_{iz} and τ_{ixy} are the axial and lateral diffusion times of species i , respectively, and the scaled complementary error function reads as $\text{erfcx}(x) = \exp(x^2)\text{erfc}(x)$. A multidimensional least-squares Gauss-Newton algorithm was used to fit the experimental data to the above model equations.

Figure 6 demonstrates the auto- and cross-correlation curves obtained for the dsDNA sample. With a mixture of free fluorophores, the cross-correlation amplitude ($G_{br} \approx 1$) was very small com-

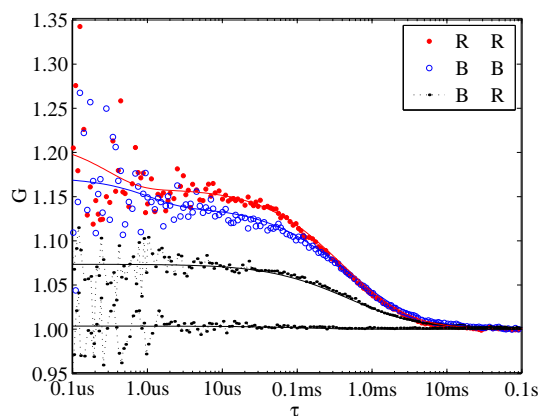


Figure 6: 2C-TIR-FCCS correlation curves and fits. G_{rr} , G_{bb} and $G_{br} > 1$ were measured with doubly labeled dsDNA. $G_{br} \approx 1$ was measured with a solution of RhG and Cy5 fluorophores.

pared to the auto-correlation amplitudes. Thin solid lines show the fits with the model equations (6).

For $\tau > 10\mu\text{s}$, the fit residuals were lower than 10^{-2} . For smaller lag times, shot noise and afterpulsing reduced the signal to noise ratio. The measured fraction of dsDNA scaled linearly with the mixed fraction from $\approx 1\%$ (no dsDNA) to $\approx 28\%$ (only dsDNA) with a relative scatter of $\approx \pm 15\%$. The measured fraction was at best one third of the mixed fraction due to an excess of molecules with a single green label, possibly further enhanced by photobleaching of the red label during the two-color excitation (29). The overlap of the sampling volumes was estimated to be $\approx 60\%$, which is close to the theoretical maximum. To reduce the influence of photobleaching, we used excitation intensities of $\approx 10\mu\text{W}/\text{mm}^2$. The molecular brightness was about two times higher compared to a confocal epi-illumination employing a 1.20NA water immersion objective at identical excitation intensities (16). The diffusion times of the dsDNA were $\tau_z \approx 51\mu\text{s}$ axially and $\tau_{xy} \approx 2.3\text{ms}$ laterally. With an evanescent field depth of 160nm and a waist radius of 370nm, the diffusion constant was calculated to be $D \approx 1.5 \cdot 10^{-7}\text{cm}^2/\text{s}$, which is about 22% of the estimated diffusion constant $D_{DNA} \approx 6.8 \cdot 10^{-7}\text{cm}^2/\text{s}$ for a rod-like molecule with 24Å diameter and 140Å length. We attribute the differences mainly to an increased hydrodynamic drag near the interface and unspecific binding (ionic interaction between DNA and coverslip).

This study demonstrated dual-color single molecule FCCS measurements based on epi-illumination TIR. This TIR-FCCS concept offers distinct advantages to confocal FCCS for coincidence assays at solid/liquid surfaces, in particular by virtue of the much higher fluorescence collection efficiency and the high confinement of the excitation field at the surface.

Single enzyme reaction kinetics measured with TIR-FFS

We investigated the kinetics of the catalytic cycle of single horseradish peroxidase enzymes when hydrogen peroxide (H_2O_2) as an electron donor is processed for oxidizing (dihydro)Rhodamine 123, thereby generating Rhodamine 123 (Rh123) (30 and references therein).

Horseradish peroxidase is a 44kDa heme protein, which efficiently catalyses the decomposition of H_2O_2 in the presence of hydrogen donors. For these experiments, we used the fluorogenic substrate (dihydro)Rh123 as hydrogen donor. After oxidation, it yields the highly fluorescing Rh123. The enzyme, the substrate and the enzyme-substrate complex are non-fluorescent. However, the product and the enzyme-product complex are fluorescent. For each catalytic cycle, two (dihydro)Rh123 are bound to the horseradish peroxidase and turned over into Rh123, which finally dissociate from the enzyme. Edman and Rigler (30) suggested that the enzyme retains some conformation memory resulting in a fluctuating enzyme activity, which is non-Markovian by nature. In a simplified model, the enzyme processes the substrate at a very high rate if it runs along a preconditioned reaction pathway, which is supposed to correspond to an "active conformation". In contrast, the enzyme processes the substrate at a very low rate if following a sub-optimal reaction pathway i.e. the "inactive conformation". It is supposed that once a pathway is adopted it favors the substrate processing due to some persistent structural information (conformation memory) retained between consecutive catalytic cycles. Overall, this leads to a fluctuating processing rate whenever the enzyme is changing the pathway i.e. the catalytic cycle. The production rate of a single enzyme can be observed by detecting the Rh123 emission at the single enzyme-single molecule level. As the evanescent excitation confines the excitation to the surface-immobilized enzyme, the background is efficiently reduced, which translates in an increased SNR when measuring the enzyme activity. For illustration, figure 7 shows a typical photon trace during a short interval. Fluorescence bursts

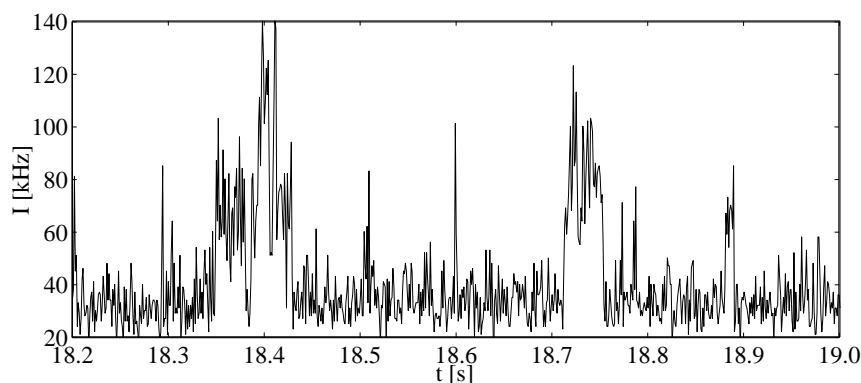


Figure 7: Photon trace of a single horseradish peroxidase producing Rh123.

indicate periods of high enzyme activity. Interruptions are due to inactive periods (31, 32).

Membrane protein detection by image correlation microscopy

Sinner et al. recently published a novel method for in vitro synthesis of complex mammalian membrane proteins into artificial planar lipid membrane structures. The cellular extract of rabbit reticulocytes contains the protein synthesis machinery for de novo synthesis of an olfactory receptor species

starting from the mere DNA from the receptor. We are investigating the density of the inserted receptor proteins by image correlation microscopy (33) using evanescent excitation at the surface. For instance, figure 8 shows the fluorescently labeled antibodies tagging affinity labels of the individual membrane proteins. The excitation area has a diameter of about 20 μ m. High-resolution image

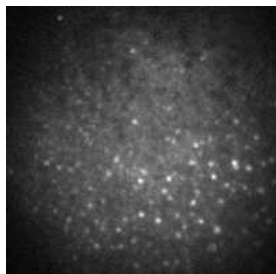


Figure 8: Image of labeled membrane proteins inserted into an artificial planar membrane surface.

correlation microscopy, i.e. the spatio-temporal auto-correlation of the membrane proteins, yields information about the spatial protein distribution (incorporation density) as well as the protein mobility (diffusion in the membrane) (34).

Conclusions

Dual-color total internal reflection fluorescence fluctuation spectroscopy provides substantial improvements compared to other existing confocal or evanescent illumination FFS setups used for single molecule studies at surfaces. Evanescent field excitation by total internal reflection at the coverslip-sample interface and the enhanced fluorescence detection efficiency within the evanescent field are major benefits for investigating biological processes and materials immobilized on glass slides. Fluorescent labeling of molecules in combination with very efficient fluorescence detection features a high signal to noise ratio for single molecule detection and imaging. In addition, dual-color excitation and detection improve the selectivity in coincidence measurements.

Acknowledgements

We would like to thank Eva-Kathrin Sinner and Rudolf Robelek for generously contributing the membrane protein application example, Hans Blom for assisting the cross-correlation measurements, and Jerker Widengren for numerous discussions and improvements of this work.

References

1. *Fluorescence Correlation Spectroscopy: Theory and Applications*; Rigler, R.; Elson, E. S., Eds.; Springer Series in Chemical Physics: Berlin Heidelberg, Germany, 2001; Vol. 65.
2. Magde, D.; Webb, W. W.; Elson, E. Thermodynamic Fluctuations in a Reacting System – Measurement by Fluorescence Correlation Spectroscopy. *Phys. Rev. Lett.* **1972**, *29*, 705–708.

3. Rigler, R.; Mets, Ü.; Widengren, J.; et al. Fluorescence Correlation Spectroscopy with high Count Rate and low Background – Analysis of Translational Diffusion. *Eur. Biophys. J. Biophys. Lett.* **1993**, *22*, 169–175.
4. Bacia, K.; Majoul, I. V.; Schwille, P. Probing the endocytic pathway in live cells using dual-color fluorescence cross-correlation analysis. *Biophys. J.* **2002**, *83*, 1184–1193.
5. Weidemann, T.; Wachsmuth, M.; Tewes, M.; Rippe, K.; Langowski, J. Analysis of Ligand Binding by Two-Colour Fluorescence Cross-Correlation Spectroscopy. *Single Mol.* **2002**, *3*, 49–61.
6. Schwille, P.; Korlach, J.; Webb, W. W. Fluorescence Correlation Spectroscopy With Single-Molecule Sensitivity on Cell and Model Membranes. *Cytometry* **1999**, *36*, 176–182.
7. Delon, A.; Usson, Y.; Derouard, J.; Biben, T.; Souchier C. Photobleaching, Mobility, and Compartmentalisation: Inferences in Fluorescence Correlation Spectroscopy. *J. Fluorescence* **2004**, *14*, 255–267.
8. Aragón, S. R.; Pecora, R. Fluorescence correlations spectroscopy as a probe of molecular dynamics. *J. Chem. Phys.* **1976**, *64*, 1791–1803.
9. Ehrenberg, M.; Rigler, R. Rotational Brownian motion and fluorescence intensity fluctuations. *Chem. Phys.* **1974**, *4*, 390–401.
10. Widengren, J.; Schwille, P. Characterization of Photoinduced Isomerization and Back-Isomerization of the Cyanine Dye Cy5 by Fluorescence Correlation Spectroscopy. *J. Phys. Chem. A* **2000**, *104*, 6416–6428.
11. Widengren, J.; Rigler, R. Mechanisms of photobleaching investigated by fluorescence correlation spectroscopy. *Bioimaging* **1996**, *4*, 149–157.
12. Widengren, J.; Mets, Ü.; Rigler, R. Fluorescence correlation spectroscopy of triplet states in solution: A theoretical and experimental study. *J. Phys. Chem.* **1995**, *99*, 13368–13379.
13. Thompson, N. L.; Burghardt, T. P.; Axelrod, D. Measuring Surface Dynamics of Biomolecules by Total Internal-Reflection Fluorescence with Photobleaching Recovery or Correlation Spectroscopy. *Biophys. J.* **1981**, *33*, 435–454.
14. Thompson, N. L.; Axelrod, D. Immunoglobulin Surface-Binding Kinetics studied by Total Internal-Reflection with Fluorescence Correlation Spectroscopy. *Biophys. J.* **1983**, *43*, 103–114.
15. Hassler, K.; Anhut, T.; Rigler, R.; Gösch, M.; Lasser, T. High Count Rates with Total Internal Reflection Fluorescence Correlation Spectroscopy. *Biophys. J.* **2005**, *88*, L1–L3.
16. Hassler, K.; Leutenegger, M.; Rigler, P.; Rao, R.; Rigler, R.; Gösch, M.; Lasser, T. Total internal reflection fluorescence correlation spectroscopy (TIR-FCS) with low background and high count-rate per molecule. *Opt. Express* **2005**, *13*, 7415–7423.
17. Leutenegger, M.; Blom, H.; Widengren, J.; Eggeling, C.; Gösch, M.; Leitgeb, R. A.; Lasser T. Dual-color Total Internal Reflection Fluorescence cross-Correlation Spectroscopy. *J. Biomed. Opt.* **2006**, *11*, 040502.
18. Paulus, M.; Martin, O. J. F. Light propagation and scattering in stratified media: a Green's tensor approach. *J. Opt. Soc. Am. A* **2001**, *18*, 854–861.
19. Ruppin, R.; Martin, O. J. F. Lifetime of an emitting dipole near various types of interfaces including magnetic and negative refractive materials. *J. Chem. Phys.* **2004**, *121*, 11358–11361.
20. Hellen, E. H.; Axelrod, D. Fluorescence emission at dielectric and metal-film interfaces. *J. Opt. Soc. Am. B* **1987**, *4*, 337–350.
21. Novotny, L. Allowed and forbidden light in near-field optics. I. A single dipolar light source. *J. Opt. Soc. Am. A* **1997**, *14*, 91–104.
22. Mertz, J. Radiative absorption, fluorescence, and scattering of a classical dipole near a lossless interface: a unified description. *J. Opt. Soc. Am. B* **2000**, *17*, 1906–1913.
23. Pero, J. K.; Haas, E. M.; Thompson, N. L. Size Dependence of Protein Diffusion Very Close to Membrane Surfaces: Measurement by Total Internal Reflection with Fluorescence Correlation

- Spectroscopy. *J. Phys. Chem. B* **2006**, *110*, 10910–10918.
24. Schwille, P. In *Fluorescence Correlation Spectroscopy: Theory and Applications*; Rigler, R.; Elson, E. S., Eds.; Springer Series in Chemical Physics: Berlin Heidelberg, Germany, 2001; Vol. 65, pp 364–366.
 25. Wohland, T.; Rigler, R.; Vogel, H. The standard deviation in fluorescence correlation spectroscopy. *Biophys. J.* **2001**, *80*, 2987–2999.
 26. Ruckstuhl, T.; Seeger, S. Attoliter detection volumes by confocal total-internal-reflection fluorescence microscopy. *Opt. Lett.* **2004**, *29*, 569–571.
 27. Levene, M. J.; Korlach, J.; Turner, S. W.; Foquet, M.; Craighead, H. G.; Webb, W. W. Zero-Mode Waveguides for Single-Molecule Analysis at High Concentrations. *Science* **2003**, *299*, 682–686.
 28. Leutenegger, M.; Gösch, M.; Perentes, A.; Hoffmann, P.; Martin, O. J. F.; Lasser, T. Confining the sampling volume for Fluorescence Correlation Spectroscopy using a sub-wavelength sized aperture. *Opt. Express* **2006**, *14*, 956–969.
 29. Eggeling, C.; Widengren, J.; Brand, L.; Schaffer, J.; Felekyan, S.; Seidel, C. A. M. Analysis of Photobleaching in Single-Molecule Multicolor Excitation and Förster Resonance Energy Transfer Measurements. *J. Phys. Chem. A* **2006**, *110*, 2979–2995.
 30. Edman, L.; Rigler, R. Memory landscapes of single-enzyme molecules. *PNAS* **2000**, *97*, 8266–8271.
 31. Hassler, K. Ph.D. thesis, École Polytechnique Fédérale de Lausanne, Lausanne, Switzerland, 2005.
 32. Hassler, K.; Rigler, P.; et al. to be published.
 33. Petersen, N. O.; Brown, C.; Kaminski, A.; Rocheleau, J.; Srivastava, M.; Wiseman, P. W. Analysis of membrane protein cluster densities and sizes in situ by image correlation spectroscopy. *Faraday Discuss.* **1998**, *111*, 289–305.
 34. Leutenegger, M.; Sinner, E. K.; Robelek, R.; Lasser, T.; et al. to be published.

Fast focus field calculations

Marcel Leutenegger, Ramachandra Rao, Rainer A. Leitgeb,
Theo Lasser

Laboratoire d'Optique Biomédicale, École Polytechnique Fédérale de Lausanne,
1015 Lausanne, Switzerland

<http://lob.epfl.ch/>

Abstract: We present a fast calculation of the electromagnetic field near the focus of an objective with a high numerical aperture (NA). Instead of direct integration, the vectorial Debye diffraction integral is evaluated with the fast Fourier transform for calculating the electromagnetic field in the entire focal region. We generalize this concept with the chirp z transform for obtaining a flexible sampling grid and an additional gain in computation speed. Under the conditions for the validity of the Debye integral representation, our method yields the amplitude, phase and polarization of the focus field for an arbitrary paraxial input field on the objective. We present two case studies by calculating the focus fields of a 40×1.20 NA water immersion objective for different amplitude distributions of the input field, and a 100×1.45 NA oil immersion objective containing evanescent field contributions for both linearly and radially polarized input fields.

© 2006 Optical Society of America

OCIS codes: (220.2560) Optical design and fabrication, focus; (260.1960) Physical optics, diffraction theory; (070.2580) Fourier optics and optical signal processing, Fourier optics; (180.0180) Microscopy.

References and links

1. P. Debye, "Das Verhalten von Lichtwellen in der Nähe eines Brennpunktes oder einer Brennpunktlinie," *Ann. Phys.* **30**, 755–776 (1909).
2. E. Wolf, "Electromagnetic diffraction in optical systems, I. An integral representation of the image field," *Proc. R. Soc. London Ser. A* **253**, 349–357 (1959).
3. B. Richards, E. Wolf, "Electromagnetic diffraction in optical systems, II. Structure of the image field in an aplanatic system," *Proc. R. Soc. London Ser. A* **253**, 358–379 (1959).
4. Typically, a good accuracy is achieved for $M \geq 50$ and $N \geq 200$ sampling points.
5. P. Török, P. Varga, "Electromagnetic diffraction of light focused through a stratified medium," *Appl. Opt.* **36**, 2305–2312 (1997).
6. J.J. Stamnes, *Waves in Focal Regions: propagation, diffraction and focusing of light, sound and water waves*, Hilger, Bristol UK (1986).
7. G. Mikula, A. Kolodziejczyk, M. Makowski, C. Prokopowicz, M. Sypek, "Diffractive elements for imaging with extended depth of focus," *Opt. Eng.* **44**, 058001 (2005).
8. N. Huse, A. Schönle, S.W. Hell, "Z-polarized confocal microscopy," *J. Biomed. Opt.* **6**, 480–484 (2001).
9. J. Enderlein, I. Gregor, D. Patra, T. Dertinger, U.B. Kaupp, "Performance of Fluorescence Correlation Spectroscopy for Measuring Diffusion and Concentration," *Chem. PhysChem.* **6**, 2324–2336 (2005).
10. For simplification, the sample indices kl and mn will be omitted further on.
11. M. Mansuripur, "Certain computational aspects of vector diffraction problems," *J. Opt. Soc. Am. A* **6**, 786–805 (1989).
12. M. Sypek, "Light propagation in the Fresnel region. New numerical approach," *Opt. Comm.* **116**, 43–48 (1995).
13. P. Luchini, "Two-dimensional numerical integration using a square mesh," *Comp. Phys. Comm.* **31**, 303–310 (1984).
14. J. L. Bakx, "Efficient computation of optical disk readout by use of the chirp z transform," *Appl. Opt.* **41**, 4897–4903 (2002).

15. Y. Li, E. Wolf, "Three-dimensional intensity distribution near the focus in systems of different Fresnel numbers," *J. Opt. Soc. Am. A* **1**, 801–808 (1984).
 16. W. Hsu, R. Barakat, "Stratton-Chu vectorial diffraction of electromagnetic fields by apertures with application to small-Fresnel-number systems," *J. Opt. Soc. Am. A* **11**, 623–629 (1994).
 17. E. Wolf, Y. Li, "Conditions for the validity of the Debye integral representation of focused fields," *Opt. Comm.* **39**, 205–210 (1981).
 18. P. Török, "Focusing of electromagnetic waves through a dielectric interface by lenses of finite Fresnel number," *J. Opt. Soc. Am. A* **15**, 3009–3015 (1998).
-

1. Introduction

The plane wave spectrum (PWS) method is a well-known and efficient technique for calculating the propagation and diffraction of electromagnetic (EM) fields. Its efficiency lies in the ability to propagate EM fields from one plane to another using the fast Fourier transform (FFT).

In microscopy this concept is the essence of the Debye approximation and is often used for the calculation of the EM field [1, 2, 3] near the focus of high numerical aperture (NA) objectives. Török et al. considerably expanded this concept for studying the focal field distribution and its distortions in stratified media commonly encountered in optical microscopy [5]. For a general and historical review on diffraction theory the reader is referred to Stamnes [6].

However, for focal field calculations in microscopy, in particular for optical systems with high NA, this classical problem turns into a computational challenge due to the highly oscillatory behavior of the involved functions. In addition, polarization effects cannot be neglected rendering this calculation long and tedious. Recent techniques in microscopy and tomography such as the extended focus field [7], microscopy beyond the Abbe resolution limit and point-spread function engineering as advanced by S. Hell and his group [8], or rigorous *ab initio* calculations for fluorescence fluctuation spectroscopy [9] amplify the demand for fast focal field calculations.

In this paper we revisit the Debye approximation and propose a novel and flexible implementation of the Debye integral incorporating the effects of amplitude, phase and polarization in an overall manner. This new implementation is particularly suited for rapid numerical evaluation and requires substantially less effort for calculating the amplitude, phase and polarization of an EM field distribution generated by a high NA microscope objective.

The organization of this paper is as follows: Section 2 introduces the Debye approximation, i.e. the general framework and formulae used in the remainder of this work. Section 3 outlines the implementation based on the fast Fourier transform (FFT) and establishes the sampling and border conditions for obtaining accurate numerical results. Finally, section 4 presents selected examples, firstly the calculation of the EM field for a 40×1.20 NA water immersion microscope objective, and secondly, for a 100×1.45 NA oil immersion objective taking into account the evanescent field contribution.

2. The Debye diffraction integral as Fourier transform

This section establishes the basic formalism based on the Debye diffraction integral and the formulation of this integral as a Fourier transform. The basic optical layout and the respective coordinate systems are shown in Fig. 1. We assume that this optical setup, i.e. the imaging system obeys Abbe's sine condition (as usually fulfilled for microscope objectives).

A coherent, monochromatic wave field parallel to the optical axis crosses the aperture stop \mathbb{A} , propagates towards the principal plane \mathbb{P}_1 and is transferred to the principal plane \mathbb{P}_2 . At \mathbb{P}_2 , the wave field is refracted and focused towards the focal point \mathbb{F}_2 . The point \mathbb{P} lies on the principal plane \mathbb{P}_2 and illustrates the focusing of a ray at \mathbb{P}_2 towards the focal point \mathbb{F}_2 . The

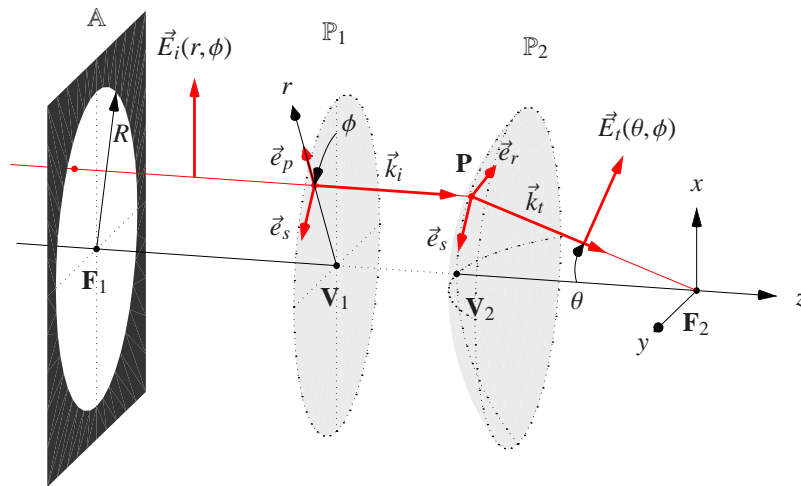


Fig. 1. Optical setup. The objective is represented by the aperture stop \mathbb{A} with radius R , the principal planes \mathbb{P}_1 and \mathbb{P}_2 with vertex points \mathbf{V}_1 and \mathbf{V}_2 , and the foci \mathbf{F}_1 and \mathbf{F}_2 . The focal length f is given as $f = \overline{\mathbf{F}_1\mathbf{V}_1}$. The point \mathbf{P} is the intersection point of a ray with \mathbb{P}_2 and shows the relation of the position r at \mathbb{P}_1 of the incident wave \vec{E}_i to the propagation angle θ at \mathbb{P}_2 of the transmitted wave \vec{E}_t .

spherical surface \mathbb{P}_2 is centered at \mathbf{F}_2 and the deflection angle θ at the position \mathbf{P} is given by

$$\sin \theta = \frac{r}{R} \frac{NA}{n_t} \quad (1)$$

where r is the off-axis coordinate of the incident wave, R the aperture stop radius, NA the numerical aperture of the objective and n_t the index of refraction behind the \mathbb{P}_2 surface. In our setup, the aperture \mathbb{A} is placed in the back focal plane, which results in a telecentric imaging system.

Instead of the principal planes, pupils are frequently used for modeling the wave propagation through the objective. However, diffraction at the aperture stop *inside the objective* is not obvious if the incident wave is transferred directly from the entrance pupil to the exit pupil. Within our representation, the wave propagation from the aperture plane \mathbb{A} to the principal plane \mathbb{P}_1 is easily calculated with the PWS method or in most cases based on classical Fourier optics principles.

The incident field $\vec{E}_i(r, \phi)$ at \mathbb{P}_1 is decomposed into a radial component (p-polarized) and a tangential component (s-polarized). The unit vectors for p- and s-polarization are

$$\vec{e}_p = \begin{pmatrix} \cos \phi \\ \sin \phi \\ 0 \end{pmatrix} \quad \text{and} \quad \vec{e}_s = \begin{pmatrix} -\sin \phi \\ \cos \phi \\ 0 \end{pmatrix} \quad (2)$$

where ϕ is the azimuth angle around the z -axis. Upon transmission, the unit vector \vec{e}_p is deflected by θ and becomes

$$\vec{e}_r = \begin{pmatrix} \cos \phi \cos \theta \\ \sin \phi \cos \theta \\ \sin \theta \end{pmatrix}. \quad (3)$$

Hence, the amplitude, phase and polarization of the transmitted field at \mathbb{P}_2 is

$$\vec{E}_t(\theta, \phi) = t_p(\vec{E}_i \cdot \vec{e}_p) \vec{e}_r + t_s(\vec{E}_i \cdot \vec{e}_s) \vec{e}_s \quad (4)$$

where $t_p(\theta, \phi)$ and $t_s(\theta, \phi)$ are the transmission coefficients (viz pupil function, apodization) for p- and s-polarization, respectively. Accumulated phase distortions, i.e. aberrations at \mathbb{P}_2 , as well as attenuations, i.e. amplitude factors, are integrated in the complex parameters t_p and t_s . As we assume the incident field to be paraxial, the axial component E_{iz} is small against the lateral components $E_{ix,y}$ and can be neglected even if the incident phase is not constant. In the Debye approximation, the transmitted field \vec{E}_t is the *plane wave spectrum* of the focus field \vec{E} near \mathbf{F}_2 . Hence, the electric field \vec{E} at a point (x, y, z) is obtained by integrating the propagated plane waves, viz

$$\begin{aligned} \vec{E}(x, y, z) &= -\frac{if}{\lambda_0} \iint_{\Omega} \vec{E}_t(\theta, \phi) e^{i(k_z z - k_x x - k_y y)} d\Omega \\ &= -\frac{if}{\lambda_0} \int_0^{\Theta} \sin \theta \int_0^{2\pi} \vec{E}_t(\theta, \phi) e^{i(k_z z - k_x x - k_y y)} d\phi d\theta. \end{aligned} \quad (5)$$

The phase factor $e^{ik_z z}$ accounts for the phase accumulation when propagating along the z -axis, whereas the term $e^{-i(k_x x + k_y y)}$ represents the phase difference of the wave front at off-axis points (x, y, z) with respect to the on-axis point $(0, 0, z)$. The integration extends over the solid angle Ω under which \mathbb{P}_2 is observed at \mathbf{F}_2 , i.e. $\sin \Theta = NA/n_t$. The wave vector \vec{k}_t is given in spherical coordinates θ and ϕ by

$$\vec{k}_t(\theta, \phi) = k_0 n_t \begin{pmatrix} -\cos \phi \sin \theta \\ -\sin \phi \sin \theta \\ \cos \theta \end{pmatrix} \quad \text{where} \quad k_0 = \frac{2\pi}{\lambda_0}. \quad (6)$$

The evaluation of Eq. (5) is usually performed with a direct numerical integration taking into account the coordinate transformations, which results in the Richard-Wolf integral representation [2, 3]. Instead of the common ansatz, a (θ, ϕ) -sampling keeping $d\Omega = \sin \theta d\theta d\phi$ constant is obtained by using $\cos \theta_m = 1 - m\Delta\Theta$ with $m \in \mathbb{N}$. For $m \in \{1 \dots M\}$ and $n \in \{1 \dots N\}$, the sampling grid is defined by

$$\theta_m = \arccos \left(1 - m \frac{1 - \sqrt{1 - NA^2/n_t^2}}{M} \right) \quad \text{and} \quad \phi_n = \left(n - \frac{1}{2} \right) \frac{2\pi}{N}. \quad (7)$$

At $\theta = 0$, a sampling point with a weight of $d\Omega = \pi\theta_1^2/4$ is added. Besides minimizing the number of sampling points along θ , the calculation of the integrand and its integration can be merged in a single matrix product resulting in a further reduction of the computation time [4].

The outlined evaluation of the Debye diffraction integral (5) is quite fast, but still much slower than the conventional computation of a Fraunhofer diffraction integral. However, Eq. (5) can be easily rewritten as a Fourier transform by splitting the phase factor into a lateral and an axial term, and by performing the integration over \mathbb{P}_1 instead of \mathbb{P}_2 . Using Eq. (1) and (6), the integration step $d\Omega$ for a sampling over \mathbb{P}_2 is projected onto \mathbb{P}_1 , which yields

$$d\Omega = \left(\frac{NA}{Rn_t} \right)^2 \frac{r dr d\phi}{\cos \theta} = \left(\frac{NA}{Rn_t} \right)^2 \frac{dx dy}{\cos \theta} = \frac{1}{k_t^2} \frac{dk_x dk_y}{\cos \theta}. \quad (8)$$

Insertion of this sampling step into Eq. (5) results in

$$\vec{E}(x, y, z) = -\frac{if}{\lambda_0 k_t^2} \iint_{r < R} (\vec{E}_t(\theta, \phi) e^{ik_z z} / \cos \theta) e^{-i(k_x x + k_y y)} dk_x dk_y. \quad (9)$$

Extending now the integration over $(k_x, k_y) \in \mathbb{R}^2$ by setting $|\vec{E}_t| = 0$ for $r > R$ allows to rewrite the Debye diffraction integral as a Fourier transform of the weighted field \vec{E}_t , which finally results in

$$\vec{E}(x, y, z) = -\frac{if}{\lambda_0 k_t^2} \mathcal{F}(\vec{E}_t(\theta, \phi) e^{ik_z z} / \cos \theta). \quad (10)$$

This is the main result of this work. The Debye integral is now expressed as a Fourier transform of the field distribution in the aperture \mathbb{A} . The similarity of this expression with the conventional Fraunhofer diffraction integral is obvious. For a low NA imaging system, the weighting factor is approximated by $1/\cos \theta \approx 1$ and Eq. (10) is equivalent to the Fraunhofer diffraction integral.

3. Numerical implementation

The numerical implementation is straightforward. A fast Fourier transform (FFT) of the weighted field at \mathbb{P}_2 is used for the numerical evaluation of Eq. (10). For an equidistant sampling $k_x = m\Delta K$ and $k_y = n\Delta K$ with $\Delta K = k_0 NA/M$, viz M sampling points over the aperture radius, the sampling points on \mathbb{P}_2 are

$$\theta_{mn} = \arcsin\left(\frac{\Delta K}{k_t} \sqrt{m^2 + n^2}\right) \quad \text{and} \quad \phi_{mn} = \arctan\left(\frac{n}{m}\right) \quad \text{for } |m|, |n| \leq M. \quad (11)$$

Multiplication of the integration step $(\Delta K)^2$ with the prefactor of Eq. (10) yields the numerical implementation of Eq. (10) as

$$\vec{E}(x_{kl}, y_{kl}, z) = -\frac{iR^2}{\lambda_0 f M^2} \text{FFT}\left(e^{ik_z z} \vec{E}_t(\theta_{mn}, \phi_{mn}) / \cos \theta_{mn}\right). \quad (12)$$

Typically, the FFT is more than $100\times$ faster than the direct integration of Eq. (5) with matrix multiplication. A good accuracy is achieved for $4M^2 \gtrsim 100 \times 100$ sampling points over Ω , but care has to be taken in order to avoid artifacts due to sampling and aliasing. Subsequently, the necessary conditions for obtaining accurate results are investigated [10].

3.1. Sampling condition

The propagation factor $e^{ik_z z}$ in Eq. (10) has to be calculated with high resolution for accurate results [11]. This imposes a condition on the phase discretization, i.e. the phase $k_z z$ must not change by more than π between neighboring sampling points in the aperture plane \mathbb{A} . With $k_z = \sqrt{k_t^2 - k_{xy}^2}$, the sampling condition can be expressed as

$$\max \left| \frac{d(k_z z)}{dk_{xy}} \right| = \max \left| z \frac{k_{xy}}{k_z} \right| = \max |z \tan \theta| < \frac{\pi}{\Delta K} \quad (13)$$

where $\Delta K = k_0 NA/M$ and $\max |\tan \theta| = NA / \sqrt{n_t^2 - NA^2}$. This immediately leads to a condition for the minimum number of sampling points

$$M > \frac{2NA^2}{\sqrt{n_t^2 - NA^2}} \frac{|z|}{\lambda_0}, \quad (14)$$

solely determined by the system parameters. For the numerical evaluation, an oversampling of about $3\times$ is sufficient for improving the accuracy of the result. In addition, a lower limit of $M \gtrsim 50$ reveals necessary for an accurate sampling of ϕ . Deviations from these sampling conditions result in granular artifacts as seen in Fig. 3(a). As a typical value for M , we have chosen $M = 125$ for the focus field calculation of a 1.20 NA water immersion objective (see the example 4.1). A high accuracy is obtained for $|z| \lesssim 25\lambda_0$, corresponding to $\approx 12 \mu\text{m}$ at a wavelength of 488 nm.

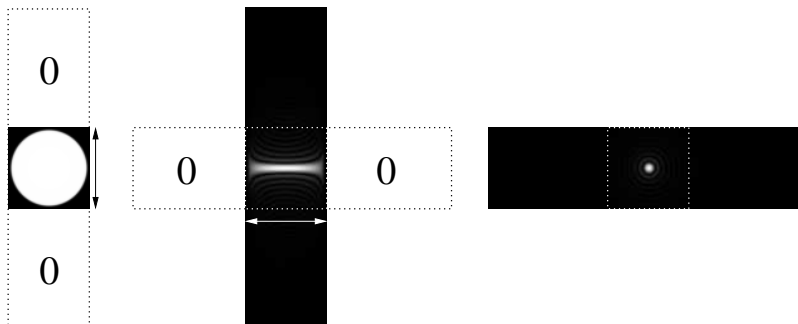


Fig. 2. Two-dimensional fast Fourier transform $\text{FFT}(\vec{E}_t/\cos\theta) = \vec{E}(x,y,0)$ limited to the region of interest (dotted square). Left: Field \vec{E}_t , aperture matrix padded with zeros (dotted rectangle). Center: FFT along the first dimension, cropped and padded with zeros. Right: FFT along the second dimension. The arrows indicate the transformed dimension.

3.2. Sampling step

The focus field \vec{E} is obtained for the sampling positions $(m\Delta x, n\Delta y, z)$. With $\Delta k = 2\pi/N\Delta r$ and $\Delta r = f\Delta K/k_t$, the sampling step in the xy -plane is

$$\Delta x = \Delta y = f \frac{\Delta k}{k_t} = \frac{M}{N} \frac{\lambda_0}{NA} \quad (15)$$

where $N > 4M$ is the number of FFT sampling points per transformed dimension (see also Fig. 2, where the arrows span over $2M+1$ samples and the padded dimension over N samples). For optimal FFT performance, it is best to set $N = 2^s$ with $s \in \mathbb{N}$. Respecting the condition (14), M can be adjusted to fit Δx and Δy . Along the z -direction, the sampling can be chosen arbitrarily by respecting the limits given above.

3.3. Aliasing suppression

Due to the Debye diffraction integral expressed in Eq. (10), the field \vec{E}_t is the plane wave spectrum of the focus field \vec{E} . Usually, the smallest area (aperture matrix) containing $\vec{E}_t \neq 0$ is transformed (see Fig. 2). The spectral product $e^{ik_z z} \times \vec{E}_t/\cos\theta$ in Eq. (10) represents a spatial convolution $\vec{E} = \mathcal{F}(e^{ik_z z}) * \mathcal{F}(\vec{E}_t/\cos\theta)$. In general, the result of the convolution is non-zero on an area larger than the aperture size, which may cause aliasing [12]. Therefore, the aperture matrix is enlarged by zero padding to at least twice its dimensions before performing the transform. In a final step, simple cropping of the transform output removes the padding.

Because we are only interested in the field near the focus, typically over a range of several wavelengths, we limit the computation of the FFT to this region of interest (Fig. 2). The transmitted field \vec{E}_t is padded with zeros along the first dimension. In this dimension, the FFT is calculated and the result cropped. Along the second dimension, the same procedure is applied

on the intermediate result. Zero padding simultaneously suppresses aliasing and refines the sampling grid for the focus field. Using two one-dimensional FFTs with intermediate cropping and zero padding minimizes the numerical processing cost.

3.4. Aperture rim smoothing

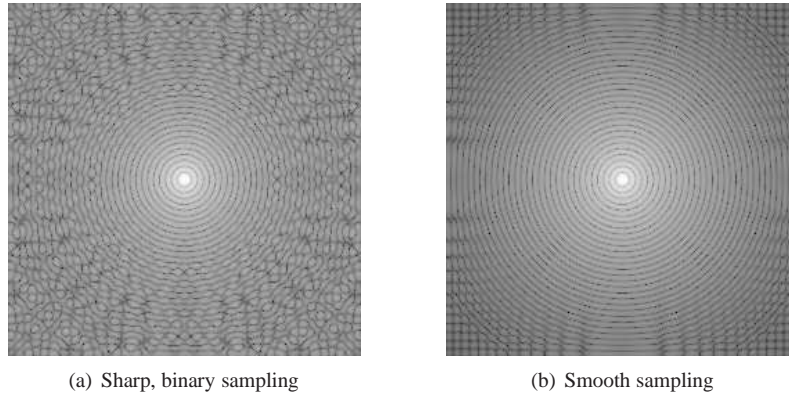


Fig. 3. Spectrum (logarithmic scale) with binary sampling of the aperture rim (a), respectively with smoothing as given by Eq. (16) (b). Binary sampling leads to discretization errors at the aperture rim, which results in granular artifacts at high frequencies. Therefore, (a) is only accurate at low frequencies over $\lesssim 20\%$ of the focal field. In (b) these artifacts are almost suppressed for $\gtrsim 70\%$ of the focal field.

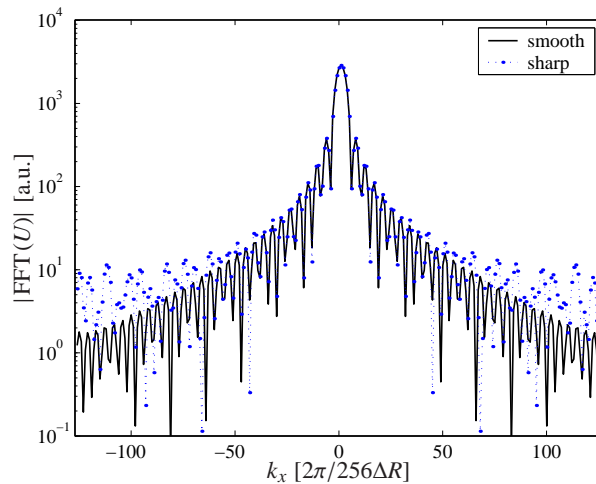


Fig. 4. Comparison of cross-sections through the 'sharp' and 'smooth' focal fields.

Figure 3 shows the spectra $\log|\text{FFT}(U)|$ for a circular aperture with radius R . As already stated, the field U vanishes outside the aperture for $r > R$, whereas inside the aperture for $r < R$, the field is given as $U = U_0$. This discretization leads to a serrated aperture rim inducing granular artifacts at higher frequencies. Hence, the expected Airy function is only seen at low frequencies (central region in Fig. 3(a), please note the logarithmic scale). A smooth sampling

of the aperture rim improves the accuracy of the spectrum [13]. In Fig. (Fig. 3(b)) the rim was sampled with the hyperbolic tangent as

$$U(r) = \frac{1}{2} \left(1 + \tanh \left(\frac{1.5}{\Delta R} (R - r) \right) \right) U_0 \quad (16)$$

where $\Delta R = R/30$ was the sampling step. The granular artifacts are efficiently reduced and the FFT approximates the Airy function with a good accuracy over a much larger area. Figure 4 shows a comparison of cross-sections of the spectra on the meridian $k_y = 0$. Overall, for values $|k_x| > 60 \times 2\pi / 256\Delta R$, the 'sharp' spectrum shows granular artifacts, whereas the 'smooth' spectrum approximates well the Airy function.

3.5. Generalization based on the chirp z transform

We demonstrated the importance of zero padding while respecting the sampling condition (14). These constraints led to a minimal number of sampling points $N = 2^s$ for the FFT ($s \in \mathbb{N}$). The corresponding number of sampling points M over the aperture radius often exceeds the initial guess based Eq. (14). In such cases, the chirp z transform (CZT) is computationally faster than the FFT. In summary, the CZT (a) allows breaking the relationship between M and N , (b) allows an implicit frequency offset, and (c) internalizes the zero padding. Applying this generalization, we adapted the sampling step in the focus field independently of the sampling step in the input field, introduced an additional shift of the region of interest, and finally improved the computational efficiency.

Let $z_m \forall m \in [0, M-1]$ be a discrete representation of a spatial signal $z(r = m\Delta r)$. The discrete Fourier transform (DFT) at a frequency $k = n\Delta k \forall n \in [0, N-1]$ is then obtained with

$$F_n = \sum_{m=0}^{M-1} z_m e^{-imn\Delta k}. \quad (17)$$

The FFT is a particular case of the DFT with $\Delta k = 2\pi/M\Delta r$ and $N = M$. For $\Delta k < 2\pi/M\Delta r$, a zero padding is implicitly contained in Eq. (17). Comparing the DFT with the CZT defined by

$$Z_n = \sum_{m=0}^{M-1} z_m a^{-m} w^{mn} \quad (18)$$

yields $a = 1$ and $w = e^{-i\Delta k}$ for obtaining the DFT as a particular case of the general CZT. Setting $a = e^{ik_0}$ shifts the frequency domain by k_0 (see above). Furthermore, Eq. (18) can be rewritten as a convolution

$$Z_n = w^{n^2/2} \sum_{m=0}^{M-1} z_m a^{-m} w^{m^2/2} \cdot w^{-(n-m)^2/2} = \left(\left(z_m a^{-m} w^{m^2/2} \right) * \left(w^{-m^2/2} \right) \right) w^{n^2/2} \quad (19)$$

that can be evaluated using two $(M+N-1)$ point FFTs (a third one can be precomputed) [14].

$$Z = \text{CZT}_{a,w}(z) = w^{n^2/2} \text{FFT}^{-1} \left(\text{FFT} \left(z_m a^{-m} w^{m^2/2} \right) \cdot \text{FFT} \left(w^{-m^2/2} \right) \right) \quad (20)$$

Based on the CZT, our computation method can be extended for low NA systems or for focus fields with a large axial span. In such cases, the sampling grid becomes distorted over the focus depth [15, 16]. But within the framework of the CZT, this distortion can be compensated by a non-linear scaling proportional to the effective NA under which the aperture \mathbb{A} is observed at \mathbb{P}_2 from a point $(0, 0, z)$ on the axis. As a result, the sampling Δk depends upon the axial position z , i.e. $\Delta k(z) = \Delta k(0) f / (f + z)$ with $\Delta k(0) = \Delta k$ as defined before. Using the CZT, the additional calculations remain restricted to the repeated computation of $\text{FFT}(w^{-m^2/2})$ because w varies now with z .

4. Selected examples

This section presents example calculations for two high NA microscope objectives. In the first example of a 1.20 NA water immersion objective, the variation of different amplitude distributions (apodization) in the aperture \mathbb{A} are discussed. For the second example, a 1.45 NA oil immersion objective was chosen as used in total internal reflection microscopy. The refraction at a cover glass-water interface at the focus is added and the effect of different polarization distributions in the aperture plane \mathbb{A} are discussed.

Before presenting these specific examples, the transmission coefficients t_p and t_s between the principal planes \mathbb{P}_1 and \mathbb{P}_2 need to be defined. We present the microscope objective as an optical system of only 2 optical interfaces and a convex interface into the immersion medium n_t . To this end, the three interfaces provide a physical model for deflection angles $\theta \in [0, \pi/2)$. The amplitude transmission efficiency, i.e. apodization, and the polarization are obtained based on the Fresnel equations.

If the glass lens has an index of refraction n_g and the immersion medium n_t , the Fresnel transmission coefficients are calculated for the succession of the air(n_a)–glass(n_g)–air(n_a)–immersion(n_t) interfaces. The corresponding deflection angle θ_{ij} at each interface was chosen proportional to the difference of the index of refraction, viz $\theta_{ij} \propto |n_i - n_j|$. With $n_a = 1$, the Fresnel transmission coefficients are then

$$t_p = \frac{1}{n_t} \left(1 - \left(\frac{2n_g - (n_g^2 + 1) \cos \theta_{ag}}{(n_g^2 - 1) \cos \theta_{ag}} \right)^2 \right) \frac{2 - 2n_t \cos \theta_{at}}{2n_t - (n_t^2 + 1) \cos \theta_{at}} \quad (21)$$

for p-polarization and

$$t_s = \left(1 - \left(\frac{n_g^2 - 2n_g \cos \theta_{ag} + 1}{n_g^2 - 1} \right)^2 \right) \frac{2 - 2n_t \cos \theta_{at}}{n_t^2 - 2n_t \cos \theta_{at} + 1} \quad (22)$$

for s-polarization, respectively.

4.1. 1.20 NA water immersion objective

Figure 5 shows the focus intensity for a nearly uniform and a Gaussian illumination in the back aperture of a 1.20 NA water immersion objective. For $\Delta x = \Delta y = 20$ nm, $\Delta z = 50$ nm and $M = 100$, a 2.0 GHz Pentium 4 processor computed the field within a volume of $3 \mu\text{m} \times 3 \mu\text{m} \times 5 \mu\text{m}$ i.e. $150 \times 150 \times 100$ sampling points in less than 40 seconds. Taking the symmetry into account, the volume was further extended to $6 \mu\text{m} \times 6 \mu\text{m} \times 10 \mu\text{m}$.

In Fig. 5(a), the aperture was overfilled and the resulting focus field shows the well-known symmetry break of vectorial focus fields, for comparison the Airy profile was added. In Fig. 5(b), the aperture was underfilled to about 60% and the field becomes approximately gaussian. Figure 6 shows the electric fields along two major axes through the focus. For an overfilled aperture, the Airy profile (based on a scalar, paraxial approximation) is a good estimation of the electric field along the y-axis. For an underfilled aperture, the diameter of the central lobe is $\approx 25\%$ larger but the side lobes vanish quickly. In both cases, the polarization leads to a larger x-extension compared to the y-extension.

Figure 7 and 8 show the intensity on the major planes through the focus. The polarization dependent extensions of the lobes along the major axes x and y creates a transition zone where the fringe contrast is diminished.

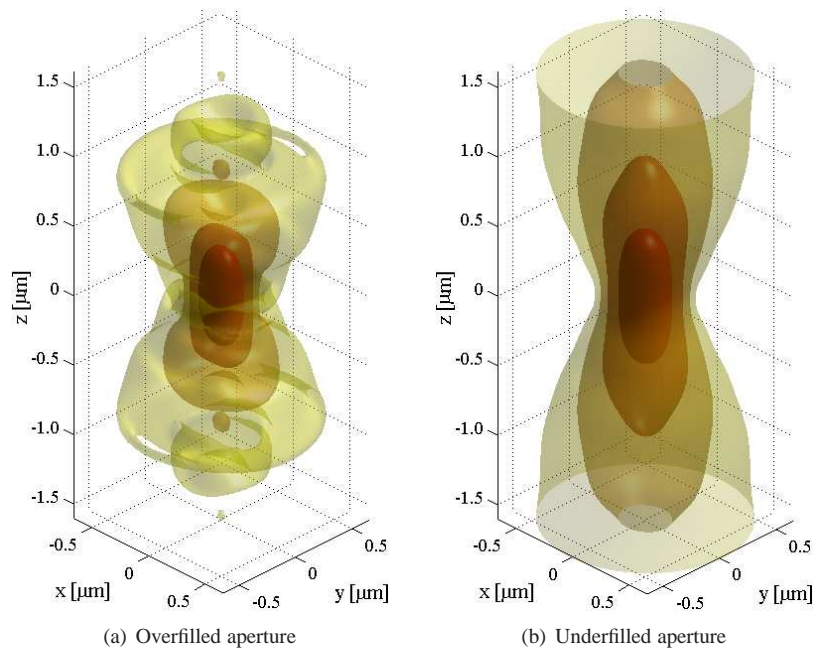


Fig. 5. Intensity distribution at the focus of a 1.20 NA water immersion objective for a x -polarized laser beam with a wavelength of $\lambda_0 = 488$ nm. The aperture had a diameter of 6.5 mm and the e^{-2} beam diameter was 10 mm (a) and 4 mm (b), respectively. The iso-intensity surfaces show the surfaces $I_{(x,y,z)} = e^{-1 \dots -4} \max(I)$.

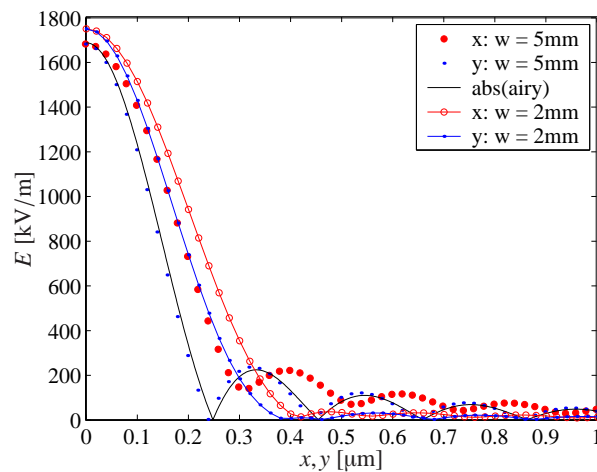


Fig. 6. Electric field profiles along the x - and y -axes, respectively, for the 40×1.20 NA water immersion objective with overfilled and underfilled aperture. The full laser beam power was 1 mW. The Airy profile is given for comparison.

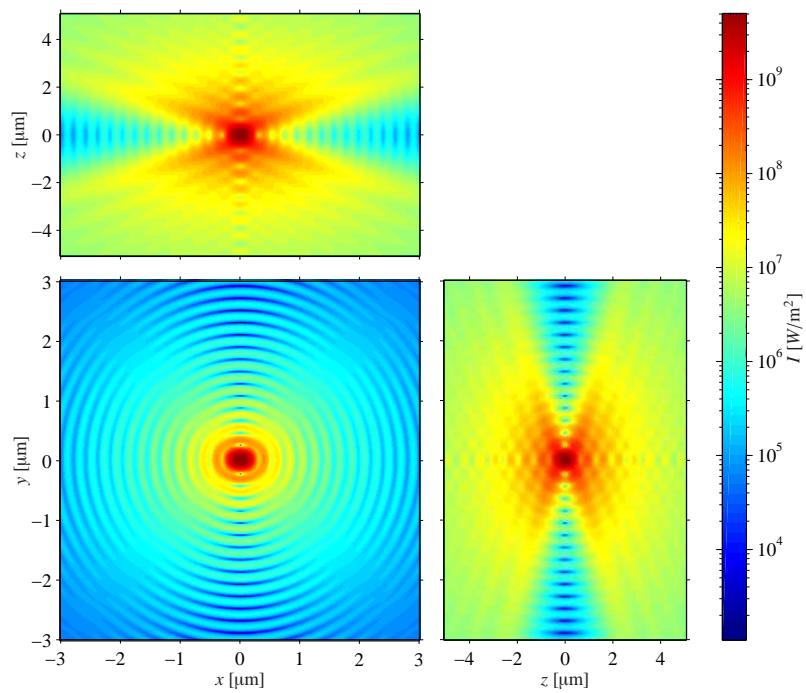


Fig. 7. Cross-sections through the focus intensity distribution of Fig. 5(a). The full laser beam power was 1 mW.

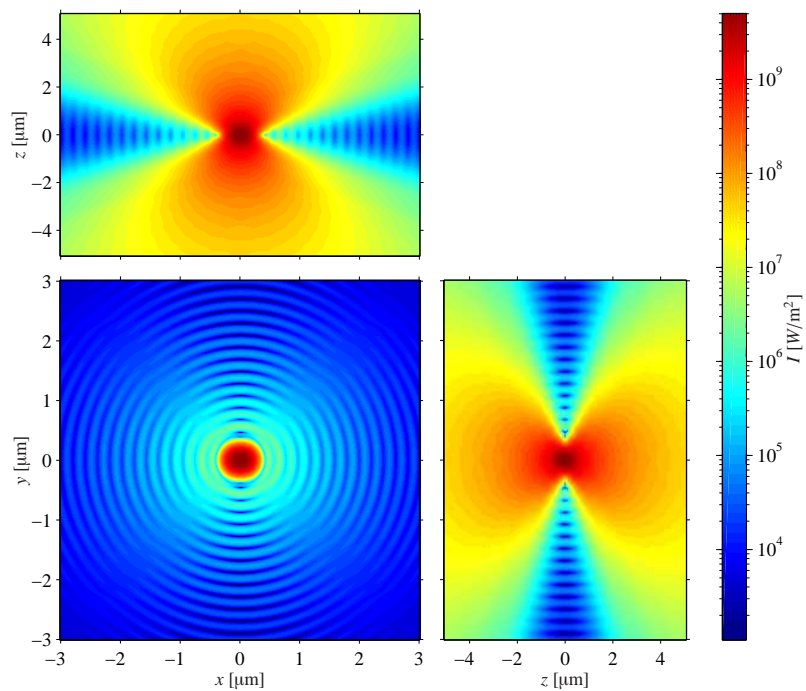


Fig. 8. Cross-sections through the focus intensity distribution of Fig. 5(b). The full laser beam power was 1 mW.

4.2. 1.45 NA oil immersion objective

As a second example, we calculate the focus field of an objective designed for total internal reflection fluorescence (TIRF). The objective uses immersion oil with an index of refraction matching the cover slip. Its NA of 1.45 is higher than the index of refraction of the sample ($n_s = 1.33$, aqueous solution). This generates a partially evanescent focus field at the cover slip–sample interface. Depending upon the illumination of the aperture, the focus field can be fully propagating or fully evanescent. A fully propagating field can be calculated easily with the procedure outlined above. However, the evanescent field contribution needs an additional consideration for obtaining the total focus field.

First we determine the plane wave spectrum \vec{E}_t at the immersion oil–cover slip interface. Next, the refraction at this interface and the cover slip–sample interface is calculated in order to obtain the plane wave spectrum \vec{E}_s in the sample (water). Finally, applying the Fourier transform on the weighted and propagated spectrum $e^{ik_z z} \vec{E}_s / \cos \theta$ yields the focus field. As before, the angle θ and the weighting factor $1/\cos \theta$ are calculated in the immersion oil. But concerning the sampling condition, a specific issue related to the cover slip–sample interface (14) needs to be considered. The highest angles θ result in total internal reflection at the cover slip–sample interface. At the critical angle $\theta_c = \arcsin(n_s/n_t)$, k_z vanishes. For higher angles, k_z takes an imaginary value and the sampling condition (14) is relaxed because $e^{ik_z z}$ becomes just an amplitude factor. The problem arises at θ_c where the sampling condition (13) results in a singularity. Let M' be the number of sampling points over $\theta < \theta_c$. For avoiding this singularity at θ_c , the sampling is chosen such that $(M' + 1/2)\Delta K = k_s$, i.e. θ_c falls between two sampling points. Inserting $M = (M' + 1/2)NA/n_s$,

$$k_{xy} = k_s \frac{M'}{M' + 1/2} \quad \text{and} \quad k_z = k_s \frac{\sqrt{M' + 1/4}}{M' + 1/2} \quad (23)$$

into Eq. (13) then yields a generalized sampling condition

$$M \gtrsim 4n_s NA \frac{z^2}{\lambda_0^2}. \quad (24)$$

A $7\times$ oversampling is used for improving the accuracy of the result, in particular at off-axis points. In addition, a lower limit of $M \gtrsim 100$ was used for $|z| \rightarrow 0$.

Because the field is calculated in the sample space, \vec{k}_t is replaced by

$$\vec{k}_s(\theta, \phi) = k_0 n_s \begin{pmatrix} \cos \phi \sin \theta' \\ \sin \phi \sin \theta' \\ \cos \theta' \end{pmatrix} = k_0 n_t \begin{pmatrix} \cos \phi \sin \theta \\ \sin \phi \sin \theta \\ \sqrt{n_s^2/n_t^2 - \sin^2 \theta} \end{pmatrix} \quad (25)$$

where $n_s \sin \theta' = n_t \sin \theta$. The unit vector \vec{e}_r for p-polarization becomes

$$\vec{e}_r = \begin{pmatrix} \cos \phi \cos \theta' \\ \sin \phi \cos \theta' \\ \sin \theta' \end{pmatrix}. \quad (26)$$

Figure 9 shows the focus field of a 100×1.45 NA oil immersion objective. The aperture of the objective was overfilled, resulting in a partially evanescent field at the focus, where the cover slip–sample (water) interface was placed. As for the former example, the central lobe extends less in the y - than the x -direction for linear polarization (Fig. 9(a)). The focal volume is reduced to about $1/8$ compared to the former water immersion objective. Selecting a radially polarized

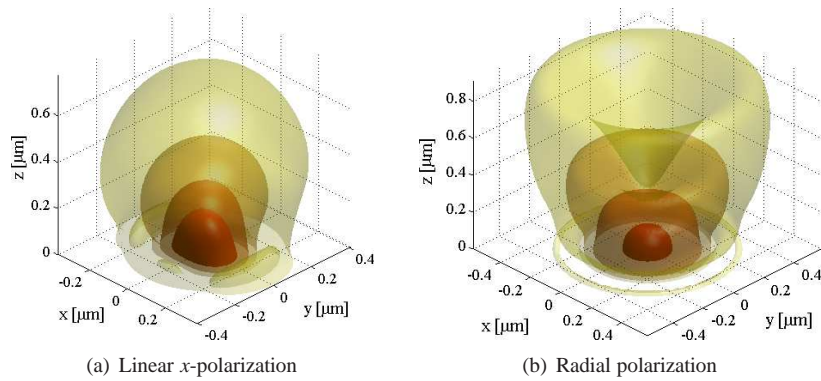


Fig. 9. Intensity distribution near the focus of a 1.45 NA oil immersion objective for a laser beam with a wavelength of $\lambda_0 = 488$ nm. The aperture had a diameter of 5.5 mm and the e^{-2} beam diameter was 10 mm. The iso-intensity surfaces show the surfaces $I_{(x,y,z)} = e^{-1 \dots -4} I_{(0)}$ in the sample space.

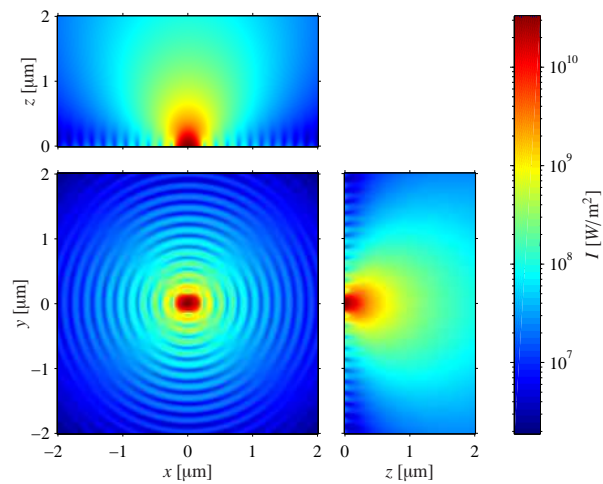


Fig. 10. Cross-sections through the focus intensity distribution of Fig. 9(a). The full laser beam power was 1 mW.

input field results in a rotationally symmetric focus field as shown in Fig. 9(b). On the optical axis, the electric field becomes purely z -polarized. For a distance $z \lesssim 0.3 \mu\text{m}$, this z -component is dominant. Further away from the cover slip–sample interface, the xy -components prevail, which results in an annular field distribution.

The fine structure at the interface is due to the evanescent wave contribution with incidence angles above the critical angle. For instance, Fig. 12 shows the weighted field $E_s / \cos \theta$ for the linear polarization. At the critical angle ($NA = 1.33$), the field amplitude approximately doubles, hence marking the abrupt transition from propagating to evanescent fields.

5. Conclusions

We showed a fast and simple implementation of the vectorial Debye integral for calculating the focus field of high NA objectives for arbitrary amplitude, phase and polarization distributions

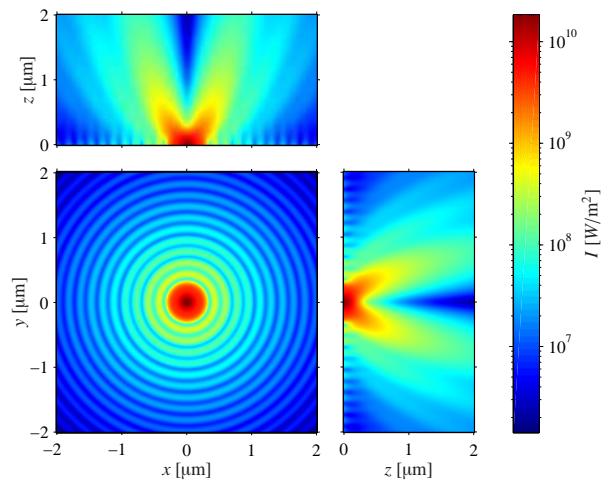


Fig. 11. Cross-sections through the focus intensity distribution of Fig. 9(b). The full laser beam power was 1 mW.

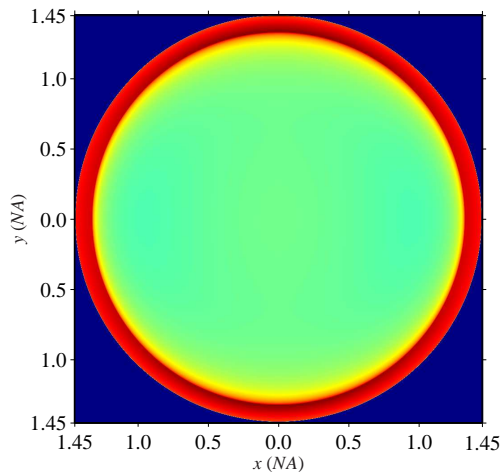


Fig. 12. Field $E_s / \cos \theta$ of Fig. 9(a). For $NA < 1.33$, the field corresponds to a free propagation in the sample space, whereas for $NA > 1.33$ an evanescent field is induced.

of the input field. The numerical evaluation with the fast Fourier transform is extremely fast and allows a high flexibility of the input field. The result is accurate under the conditions for the validity of the Debye integral representation of focused fields [17, 18] and the given sampling conditions. For low NA, it converges quite naturally to a focus field given by the Fraunhofer approximation. With the chirp z transform, we extended our calculations to low NA focus fields requesting a non-linear scaling as shown by Li and Hsu [15, 16]. Table 1 summarizes the performance of the different calculation methods on a personal computer.

In addition, we used a generalized pupil function (apodization) of high NA objectives taking into account amplitude and polarization distributions. The pupil function incorporates wave front aberrations as contained in real objectives as well as Fresnel transmission coefficients. Based on these Fresnel coefficients, it is straightforward to include wave propagation through

Method	Input fields, constraints	Integration	Output	Computation time (for 100^3 points)
Classic	Analytic functions (rotational symmetry)	Quadrature of Bessel functions	Points	20 min to hours
Direct	Any, high NA (polar sampling)	Matrix product	Lines	≈ 30 min
FFT	Any, high NA (cartesian sampling)	FFT	xy planes	≈ 1 min
CZT	Any (cartesian sampling)	CZT	xy planes	≈ 30 s

Table 1. Performance of different calculation methods.

stratified media.

In summary, our method allows fast and accurate calculations of the focus field in the entire focal region, which opens the path to fast simulations for point spread function engineering and image deconvolution in three-dimensional light microscopy.

Acknowledgements

We are grateful to Herbert Gross, Carl Zeiss Oberkochen for many valuable comments and discussions. The support of the Swiss National Science Foundation (SNSF) (contract number 200021-103333) is greatly acknowledged.

Dual-color total internal reflection fluorescence cross-correlation spectroscopy

Marcel Leutenegger,^{a,*} Hans Blom,^b Jerker Widengren,^b Christian Eggeling,^c Michael Gösch,^a Rainer A. Leitgeb,^a and Theo Lasser^a

^aLaboratoire d'Optique Biomédicale
École Polytechnique Fédérale de Lausanne
1015 Lausanne, Switzerland

^bBiomolekylär Fysik
Kungliga Tekniska Högskolan
10691 Stockholm, Sweden

^cMax-Planck-Institut für Biophysikalische Chemie
37077 Göttingen, Germany

Abstract. We present the development and first application of a novel dual-color total internal reflection (TIR) fluorescence system for single-molecule coincidence analysis and fluorescence cross-correlation spectroscopy (FCCS). As a performance analysis, we measured a synthetic DNA-binding assay, demonstrating this dual-color TIR-FCCS approach to be a suitable method for measuring coincidence assays such as biochemical binding, fusion, or signal transduction at solid/liquid interfaces. Due to the very high numerical aperture of the epi-illumination configuration, our setup provides a very high fluorescence collection efficiency resulting in a two- to three-fold increase in molecular brightness compared to conventional confocal FCCS. Further improvements have been achieved through global analysis of the spectroscopic data. © 2006 Society of Photo-Optical Instrumentation Engineers. [DOI: 10.1117/1.2221714]

Keywords: fluorescence spectroscopy; laser-induced fluorescence; correlation.

Paper 06008LR received Jan. 17, 2006; revised manuscript received Apr. 12, 2006; accepted for publication May 26, 2006; published online Jul. 11, 2006.

Total internal reflection fluorescence microscopy (TIR-FM) is an important tool in life science. Taking advantage of a very thin (<100 nm) optical excitation depth formed by an evanescent wave above a glass substrate, TIR fluorescence detection achieves an exceptional axial resolution and allows for the study of important cellular processes, in particular at or near the cellular membrane.¹ Prominent biological applications of TIR-FM include real-time *in vivo* observations of dynamics of molecular motors,^{2,3} or of various membrane trafficking events, such as vesicle fusion or signal transduction after receptor binding.^{4,5} To extend the sensitivity and observation of such cellular assays, it is important to combine TIR-FM with fluorescence measurement and single-molecule fluctuation analysis. Fluorescence correlation spectroscopy enables to expose biological reactivity such as binding events on the basis of temporal fluctuations in the fluorescence emission of single molecules.^{6,7} Dual-color fluorescence cross-

correlation spectroscopy (FCCS) represents a further development of fluctuation spectroscopy, which achieves a significantly improved selectivity and applicability.⁸ FCCS substitutes two differently colored labels and realizes the distinction between coinciding and separated occurrence of these labels. It thus introduces a useful tool to monitor various biological assays including molecular binding between two differently labeled binding partners. Typically, FCCS is based on a confocal epi-illumination microscope with multicolor laser excitation and single-photon detection. Nonetheless, for several applications, TIR illumination can provide further benefits, for instance when ligands interacting with receptors immobilized onto a surface are to be studied.^{9–12} First, in TIR-FCCS the molecules are only excited near the glass-sample interface, which simplifies the discrimination between freely diffusing and immobilized particles. Second, the most important prerequisite for efficient single-molecule detection is a high fluorescence count rate per molecule (CPM). Using TIR excitation and exploiting the anisotropic emission of the fluorescence generated at the glass-sample interface, much higher CPM can be extracted from the investigated molecules.¹³

In this work, we present for the first time a dual-color excitation scheme for TIR single-molecule detection, which enables us to perform FCCS at glass-sample interfaces with high sensitivity. The improved performance of TIR-FCCS was verified on a synthetic binding assay, including dual-labeled double-stranded DNA molecules in aqueous solution, demonstrating its potential for biological and cellular applications.

Figure 1 shows our dual-color TIR-FCCS setup. Two linear polarized laser beams were expanded to an e^{-2} diameter of ≈ 2 mm and collinearly aligned to the microscope objective (BE & BS; beam expansion $2.5\times$). The laser powers were controlled by neutral density filters. An achromatic lens focused the beams into the back-focal plane (BFP) of the high numerical aperture (NA) oil immersion objective (α -Plan-Fluar 100×1.45 with Immersoil™ 518F, Carl Zeiss Jena, Jena, Germany), which resulted in circular spots with e^{-2} diameters at the cover slide-sample interface of ≈ 16 μm (blue) and ≈ 20 μm (red), respectively. In the BFP, a beam foci offset of ≈ 2.3 mm from the optical axis resulted in a super-critical angle illumination, i.e., a z -confinement below 100 nm resulting from the evanescent field excitation.

Due to the epi-illumination, the fluorescent light was collected with the same high NA objective toward the pinholes and the single-photon detectors. The pinholes were realized by two multimode fibers with a core diameter of 50 μm . Dichroic mirrors and bandpass filters blocked the back-reflected laser light by more than OD10 and provided an excellent filtering of the green and red fluorescence. The fluorescence photons were detected by fiber-coupled single photon counting modules (SPCM-AQR-14-FC, PerkinElmer Optoelectronics, Wiesbaden, Germany; ASY50/105 silica fibers, Thorlabs Inc., Grünberg, Germany), whose signals (number of photons over time) were recorded and correlated with a USB hardware correlator (Flex02-08D, Correlator.com, Bridgewater, New Jersey). A focusing lens, a $\lambda/4$ plate, and a dichroic mirror were moved in one block by a linear translator for adjusting the position of the beam foci in the BFP of the objective. In this way, the excitation angle could be adjusted without alter-

*Tel: +41 21 693 78 21; E-mail: marcel.leutenegger@epfl.ch

1083-3668/2006/11(4)/040502/3/\$22.00 © 2006 SPIE

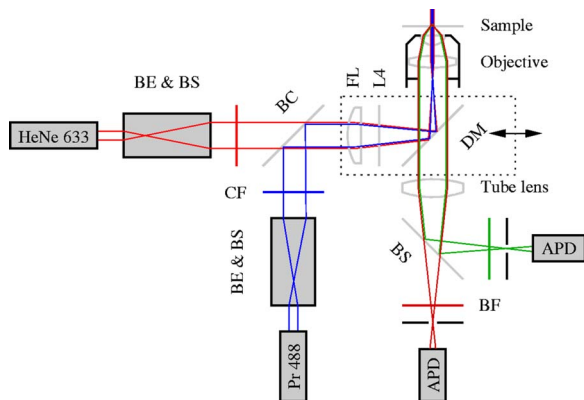


Fig. 1 Dual-color TIR-FCCS setup. HeNe 633: 18-mW HeNe gas laser (LHRP-1701, Laser 2000, Weßling, Germany). Pr 488: 22-mW solid-state laser (Protera™ 488-15, Novalux, Sunnyvale, CA). BE & BS: 2.5× beam expanders and beam steerers. CF: laser-line cleanup filters [Chroma Z488/10x (blue); Chroma Z633/10x (red); Chroma Technology Corp., Brattleboro, VT]. BC: dichroic beam combiner (Chroma Z488bcm). FL: focusing lens (achromat $f=130$ mm). L4: $\lambda/4$ plate oriented for maximum fluorescence (OWIS, Staufen, Germany). DM: dual-band dichroic mirror (Omega DM488/633, Omega Optical Inc., Brattleboro, VT). Sample: droplet on a 150- μ m-thick glass cover slide mounted on a xyz-translation stage (ULTRAlign 561D with μ Drive Controller ESA-C, Newport Corp., Darmstadt, Germany). BS: dichroic beam splitter (Omega DML625). BF: emission band-pass filters [Chroma HQ540/80m and Omega 520DF40 (green); Chroma HQ690/80m and Omega 685DF70 (red)]. APD: detectors (Color online).

ing the optical path length between the focusing lens and the objective. The configuration can easily be changed to a conventional confocal epi-illumination by removing the focusing lens and by centering the collimated beams in the BFP.

As a synthetic binding assay, we used free rhodamine green (RhG) and Cy5 fluophores, and a 40 base pair double-stranded DNA labeled with Alexa488 and Cy5 (Zeiss cross-correlation standard). The laser powers were optimized with the dsDNA sample and the background was measured with a NaCl/EDTA/TRIS pH 8.0 buffer. The cross talk between the detection channels was calibrated with free 10-nM RhG and 50-nM Cy5, respectively. For cross-correlation measurements, different mixtures of the double-labeled dsDNA

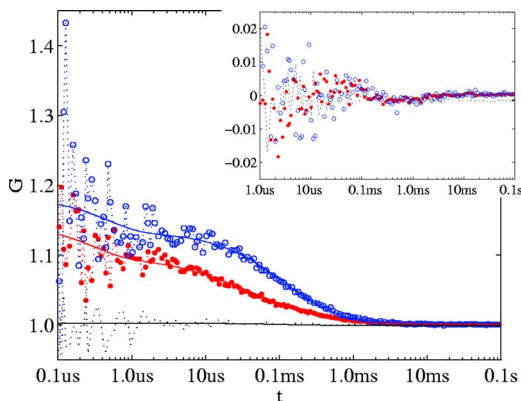


Fig. 2 Negative control (9-nM RhG/50-nM Cy5). Circles: green auto-correlation. Bold points: red auto-correlation. Dots: green-red cross-correlation. Inset: fit residuals $G_{fit}/G(t) - 1$ (Color online).

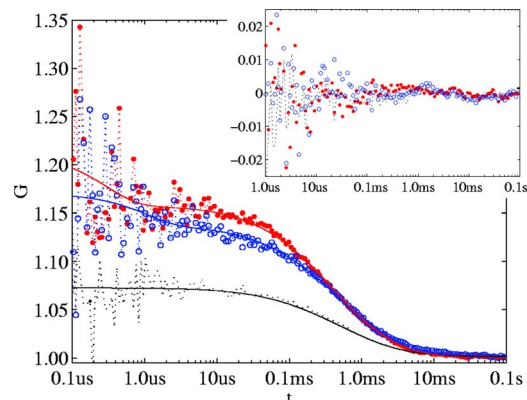


Fig. 3 Positive control (dsDNA). Circles: green auto-correlation. Bold points: red auto-correlation. Dots: green-red cross-correlation. Inset: fit residuals (Color online).

sample and free 9-nM RhG/50-nM Cy5 solutions were used and investigated with identical laser powers during a time interval of 20 s. Plasma cleaning of the cover slides improved the results due to a strong suppression of unspecific binding at the glass surface.

For free diffusion the following model equation was used:¹³

$$G_{mn}(\tau) = G_{mn\infty} + \frac{1}{2} \left(1 - \frac{B_m}{I_m}\right) \left(1 - \frac{B_n}{I_n}\right) \frac{\sum Q_{mi} Q_{ni} N_i D_{mni}(\tau)}{\sum Q_{mi} N_i \sum Q_{ni} N_i} + G_{mnt} \exp\left(-\frac{\tau}{\tau_{mnt}}\right).$$

Here, indices m and n represent the green and red detection channels; hence G_{gg} and G_{rr} are the autocorrelations of the signals in the green and red detection channels, respectively, and G_{gr} is the cross-correlation of both signals. The index i represents the diffusing species: g for RhG, r for Cy5, and c for the dsDNA. Also, B is the measured background count rate, I is the total count rate, Q_{mi} is the CPM in channel m of species i , N_i are the number of molecules in the effective sampling volume, G_{mnt} and τ_{mnt} are the triplet amplitudes and the triplet correlation times, respectively, $G_{mn\infty} \approx 1$ are the offsets at infinite lag time τ , and D_{mni} describes the diffusion and is given by¹³

$$D_{mni}(\tau) = \left(1 + \frac{\tau}{\tau_{ixy}}\right)^{-1} \left[\sqrt{\frac{\tau}{\pi\tau_{iz}}} + \left(1 - \frac{\tau}{2\tau_{iz}}\right) \operatorname{erfcx}\left(\sqrt{\frac{\tau}{4\tau_{iz}}}\right) \right]$$

where τ_{iz} and τ_{ixy} are the axial and lateral diffusion times of species i , respectively, and the scaled complementary error function is $\operatorname{erfcx}(x) = \exp(x^2) \times \operatorname{erfc}(x)$. A multidimensional least-squares Gaussian-Newtonian algorithm was used to fit the experimental data to these model equations.

For these first experiments, only relative concentrations of the species were of interest. Therefore, a unique diffusion time was used, neglecting channel differences due to an imperfect overlap of the excitation and detection volumes. The triplet term accounts for the triplet contribution in the initial correlation amplitude $G_{(0)}$.

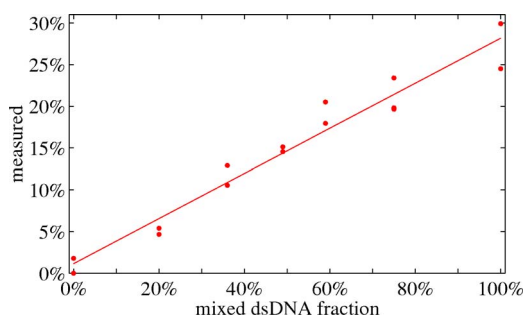


Fig. 4 Measured fraction of dsDNA versus mixed fraction

The measured background signals were $B_g=7.54$ kHz and $B_r=19.6$ kHz, respectively. Typically, autofluorescence from the immersion oil as well as from the glass slide were the main contributions to B_g and B_r , respectively. The crosstalk CPM of RhG in the red channel was found to be $Q_{rg}=0.032 \times Q_{gg}$ and assumed constant during the following evaluations. Cy5 did not show any crosstalk in the green channel, hence $Q_{gr}=0$. Therefore, the CPM were replaced by the crosstalk factor $Q_{rg}/Q_{gg}=0.032$ for simplification.

Figure 2 shows the correlation results for a mixture of the free fluorophores (negative control). The count rates of this control sample were $I_g=40.2$ kHz and $I_r=66.0$ kHz. The CPMs were $Q_{gg}=(I_g-B_g)/N_g=13.1$ kHz and $Q_{rr}=[I_r-B_r-0.032 \times (I_g-B_g)]/N_r=18.9$ kHz, respectively. Figure 3 shows the results for the Cy5 and Alexa488 labeled dsDNA correlation (positive control). We measured $I_g=39.3$ kHz and $I_r=44.2$ kHz, from which $Q_{gc}=13.3$ kHz and $Q_{rc}=27.0$ kHz were extracted. The increased count rate for bound Cy5 is attributed to a reduction of conformational changes leading to higher fluorescence emission.^{14,15} For $\tau > 10 \mu s$, the fit residuals were lower than 10^{-2} . For smaller lag times, shot noise and afterpulsing reduced the signal-to-noise ratio.

Figure 4 summarizes the TIR-FCCS measurements on a titration series of double-labeled dsDNA in a mixture of free 9-nM RhG/50-nM Cy5, such that the total fluorophore concentration was approximately constant. The measured fraction of dsDNA scaled linearly with the mixed fraction from $\approx 1\%$ (negative control) to $\approx 28\%$ (positive control). The measurements showed a relative scatter of $\approx \pm 15\%$. The measured fraction was at best one-third of the mixed fraction. This can be explained by an excess of molecules with a single green label, possibly further enhanced by photobleaching of the red label during the two-color excitation.¹⁵ The overlap of the sampling volumes was estimated to $\approx 60\%$, which is close to the theoretical maximum. To reduce the influence of photobleaching, we used excitation intensities of $\approx 10 \mu W/\mu m^2$. The measured CPM were about two times higher than with a confocal epi-illumination and a 1.20 NA water immersion objective at identical excitation intensities.^{13,16}

The diffusion times of the dsDNA were $\tau_z=51 \mu s$ axially and $\tau_{xy}=2.3$ ms laterally, respectively. Given a penetration depth of 80 nm and a waist radius of 370 nm, the diffusion constant was calculated to $D \approx 1.5 \times 10^{-7} \text{ cm}^2/\text{s}$, which is about 22% of the estimation $D_{\text{DNA}} \approx 6.8 \times 10^{-7} \text{ cm}^2/\text{s}$ for a rodlike molecule with a diameter of 24 Å and a length of

140 Å. We attribute this to an increased hydrodynamic drag near the interface and weak unspecific binding, respectively.

This study demonstrates for the first time single-molecule FCCS measurements based on an epi-illumination TIR concept. This TIR-FCCS concept offers distinct advantages to confocal FCCS for coincidence assays at solid/liquid surfaces, in particular by virtue of the much higher fluorescence collection efficiencies and the confinement of the excitation field to the surface of interest.

Acknowledgments

We thank Aram Mooradian of Novalux for the Protera laser and his continuous interest in our work, Klaus Weisshart of Carl Zeiss for contributing the cross-correlation sample, and Kai Hassler and Rudolf Rigler for many expert discussions. This work was supported by the Swiss National Science Foundation (SNSF) Grant No. 200021-103333. Jerker Widengren acknowledges support from the Swedish Strategic Research Foundation (SSF, BioX).

References

1. D. Axelrod, "Total internal reflection fluorescence microscopy in cell biology," *Traffic (Oxford, U. K.)* **2**, 764–774 (2001).
2. Y. Sako and T. Uyemura, "Fluorescence correlation spectroscopy with single-molecule sensitivity on cell and model membranes," *Cell Struct. Funct.* **27**, 357–365 (2002).
3. Y. Sako and T. Yanagida, "Single-molecule visualization in cell biology," *Nat. Rev. Mol. Cell Biol.* **4**, SS1–SS5 (2003).
4. D. Toomre and D. J. Manstein, "Lighting up the cell surface with evanescent wave microscopy," *Trends Cell Biol.* **11**, 298–303 (2001).
5. V. Beaumont, "Visualizing membrane trafficking using total internal reflection fluorescence microscopy," *Biochem. Soc. Trans.* **31**, 819–823 (2003).
6. R. Rigler, Ü. Mets, J. Widengren, and P. Kask, "Fluorescence correlation spectroscopy with high count rate and low background - Analysis of translational diffusion," *Eur. Biophys. J.* **22**, 169–175 (1993).
7. S. Weiss, "Fluorescence spectroscopy of single biomolecules," *Science* **283**, 1676–1683 (1999).
8. K. Bacia, I. V. Majoul, and P. Schwill, "Probing the endocytic pathway in live cells using dual-color fluorescence cross-correlation analysis," *Biophys. J.* **83**, 1184–1193 (2002).
9. A. M. Lieto, R. C. Cush, and N. L. Thompson, "Ligand-receptor kinetics measured by total internal reflection with fluorescence correlation spectroscopy," *Biophys. J.* **85**, 3294–3302 (2003).
10. P. Schwill, J. Korlach, and W. W. Webb, "Fluorescence correlation spectroscopy with single-molecule sensitivity on cell and model membranes," *Cytometry* **36**, 176–182 (1999).
11. R. L. Hansen and J. M. Harris, "Measuring reversible adsorption kinetics of small molecules at solid/liquid interfaces by total internal reflection fluorescence correlation spectroscopy," *Anal. Chem.* **70**, 4247–4256 (1998).
12. N. L. Thompson, T. P. Burghardt, and D. Axelrod, "Measuring surface dynamics of biomolecules by total internal-reflection fluorescence with photobleaching recovery or correlation spectroscopy," *Biophys. J.* **33**, 435–454 (1981).
13. K. Hassler, M. Leutenegger, P. Rigler, R. Rao, R. Rigler, M. Gösch, and T. Lasser, "Total internal reflection fluorescence correlation spectroscopy (TIR-FCS) with low background and high count-rate per molecule," *Opt. Express* **13**, 7415–7423 (2005).
14. J. Widengren and P. Schwill, "Characterization of photoinduced isomerization and back-isomerization of the cyanine dye Cy5 by fluorescence correlation spectroscopy," *J. Phys. Chem. A* **104**, 6416–6428 (2000).
15. C. Eggeling, J. Widengren, L. Brand, J. Schaffer, S. Felekyan, and C. A. M. Seidel, "Analysis of photobleaching in single-molecule multi-color excitation and Förster resonance energy transfer measurements," *J. Phys. Chem. A* **110**, 2979–2995 (2006).
16. J. Mertz, "Radiative absorption, fluorescence, and scattering of a classical dipole near a lossless interface: a unified description," *J. Opt. Soc. Am. B* **17**, 1906–1913 (2000).

Confining the sampling volume for Fluorescence Correlation Spectroscopy using a sub-wavelength sized aperture

Marcel Leutenegger¹, Michael Gösch¹, Alexandre Perentes²,
Patrik Hoffmann², Olivier J.F. Martin³, Theo Lasser¹

¹ Laboratoire d'Optique Biomédicale, École Polytechnique Fédérale de Lausanne, 1015
Lausanne, Switzerland

<http://lob.epfl.ch/>

² Laboratoire d'Optique Appliquée, École Polytechnique Fédérale de Lausanne, 1015
Lausanne, Switzerland

<http://apl.epfl.ch/>

³ Laboratoire de nanophotonique et métrologie, École Polytechnique Fédérale de Lausanne,
1015 Lausanne, Switzerland

<http://www.nanophotonics.ch/>

Abstract: For the observation of single molecule dynamics with fluorescence fluctuation spectroscopy (FFS) very low fluorophore concentrations are necessary. For in vitro measurements, this requirement is easy to fulfill. In biology however, micromolar concentrations are often encountered and may pose a real challenge to conventional FFS methods based on confocal instrumentation. We show a higher confinement of the sampling volume in the near-field of sub-wavelength sized apertures in a thin gold film. The gold apertures have been measured and characterized with fluorescence correlation spectroscopy (FCS), indicating light confinement beyond the far-field diffraction limit. We measured a reduction of the effective sampling volume by an order of magnitude compared to confocal instrumentation.

© 2006 Optical Society of America

OCIS codes: (050.1220) Apertures; (160.3900) Metals; (170.6280) Spectroscopy, fluorescence and luminescence; (240.6490) Spectroscopy, surface; (300.2530) Fluorescence, laser induced.

References and links

1. R. Rigler et al., "Fluorescence Correlation Spectroscopy with high Count Rate and low Background - Analysis of Translational Diffusion," *Eur. Biophys. J. Biophys. Lett.* **22**, 169–175 (1993).
2. S. Weiss, "Fluorescence Spectroscopy of Single Biomolecules," *Science* **283**, 1676–1683 (1999).
3. P. Kask, K. Palo, D. Ullmann, K. Gall, "Fluorescence-intensity distribution analysis and its application in biomolecular detection technology," *PNAS* **96**, 13756–13761 (1999).
4. Y. Chen, J.D. Müller, P.T.C. So, E. Gratton, "The Photon Counting Histogram in Fluorescence Fluctuation Spectroscopy," *Biophys. J.* **77**, 553–567 (1999).
5. L.N. Hillesheim, J.D. Müller, "The Photon Counting Histogram in Fluorescence Fluctuation Spectroscopy with Non-Ideal Photodetectors," *Biophys. J.* **85**, 1948–1958 (2003).
6. T.A. Laurence, A.N. Kapanidis, X. Kong, D.S. Chemla, S. Weiss, "Photon Arrival-Time Interval Distribution (PAID): A Novel Tool for Analyzing Molecular Interactions," *J. Phys. Chem. B* **108**, 3051–3067 (2004).

7. K. Starchev, J. Ricka, J. Buffle, "Noise on Fluorescence Correlation Spectroscopy," *J. Coll. Interf. Science* **233**, 50–55 (2001).
8. D.E. Koppel, "Statistical accuracy in fluorescence correlation spectroscopy," *Phys. Rev. A* **10**, 1938–1945 (1974).
9. M.J. Levene, J. Korlach, S.W. Turner, M. Foquet, H.G. Craighead, W.W. Webb, "Zero-Mode Waveguides for Single-Molecule Analysis at High Concentrations," *Science* **299**, 682–686 (2003).
10. M. Foquet, J. Korlach, W.R. Zipfel, W.W. Webb, H.G. Craighead, "Focal Volume Confinement by Submicrometer-Sized Fluidic Channels," *Anal. Chem.* **76**, 1618–1626 (2004).
11. T. Ruckstuhl, S. Seeger, "Attoliter detection volumes by confocal total-internal-reflection fluorescence microscopy," *Opt. Lett.* **29**, 569–571 (2004).
12. K. Hassler, T. Anhut, R. Rigler, M. Gösch, T. Lasser, "High Count Rates with Total Internal Reflection Fluorescence Correlation Spectroscopy," *Biophys. J.* **88**, L1–L3 (2005).
13. K. Hassler, M. Leutenegger, P. Rigler, R. Rao, R. Rigler, M. Gösch, T. Lasser, "Total internal reflection fluorescence correlation spectroscopy (TIR-FCS) with low background and high count-rate per molecule," *Opt. Express* **13**, 7415–7423 (2005).
14. M. Paulus, O.J.F. Martin, "Light propagation and scattering in stratified media: a Green's tensor approach," *J. Opt. Soc. Am. A* **18**, 854–861 (2001).
15. H. Rigneault, J. Capoulade, J. Dintinger, J. Wenger, N. Bonod, E. Popov, T.W. Ebbesen, P.-F. Lenne, "Enhancement of Single-Molecule Fluorescence Detection in Subwavelength Apertures," *Phys. Rev. Lett.* **95**, 117401 (2005).
16. J. Wenger, P.-F. Lenne, E. Popov, H. Rigneault, J. Dintinger, T.W. Ebbesen, "Single molecule fluorescence in rectangular nano-apertures," *Opt. Express* **13**, 7035–7044 (2005).
17. D. Amarie, N.D. Rawlinson, W.L. Schaich, B. Dragnea, S.C. Jacobson, "Three-Dimensional Mapping of the Light Intensity Transmitted through Nanoapertures," *Nanolett.* **5**, 1227–1230 (2005).
18. A. Perentes, I. Utke, B. Dwir, M. Leutenegger, T. Lasser, P. Hoffmann, F. Baida, M.P. Bernal, M. Russey, J. Salvi, D. Van Labeke, "Fabrication of arrays of sub-wavelength nano-apertures in an optically thick gold layer on glass slides for optical studies," *Nanotech.* **16**, S273–S277 (2005).
19. O. Krichevsky, G. Bonnet, "Fluorescence correlation spectroscopy: the technique and its applications," *Rep. Prog. Phys.* **65**, 251–297 (2002).
20. K. Bacia, I.V. Majoul, P. Schwillie, "Probing the endocytic pathway in live cells using dual-color fluorescence cross-correlation analysis," *Biophys. J.* **83**, 1184–1193 (2002).
21. J. Widengren, Ü. Mets, R. Rigler, "Fluorescence correlation spectroscopy of triplet states in solution: A theoretical and experimental study," *J. Phys. Chem.* **99**, 13368–13379 (1995).
22. T. Wohland, R. Rigler, H. Vogel, "The Standard Deviation in Fluorescence Correlation Spectroscopy," *Biophys. J.* **80**, 2987–2999 (2001).
23. E. Bismuto, E. Gratton, D.C. Lamb, "Dynamics of ANS Binding to Tuna Apomyoglobin Measured with Fluorescence Correlation Spectroscopy," *Biophys. J.* **81**, 3510–3521 (2001).
24. J. Enderlein, I. Gregor, D. Patra, J. Fitter, "Art and artefacts of fluorescence correlation spectroscopy," *Curr. Pharmaceut. Biotech.* **5**, 155–161 (2004).
25. G.T. Boyd, Z.H. Yu, Y.R. Shen, "Photoinduced luminescence from the noble metals and its enhancement on roughened surfaces," *Phys. Rev. B* **33**, 7923–7936 (1986).
26. K. Kneipp, H. Kneipp, I. Itzkan, R.R. Dasari, M.S. Feld, "Surface-enhanced Raman scattering and biophysics," *J. Phys. Condens. Matter* **14**, R597–R624 (2002).

1. Introduction

In the last decade, fluorescence fluctuation spectroscopy (FFS) emerged as a powerful screening tool in pharmaceutical industry and in biomedical research. For FFS, a high numerical aperture objective focuses a laser beam into a sample containing labeled molecules at low concentration. The fluorescence is collected by the same objective and filtered by a dielectric band-pass filter to suppress reflected excitation and Raman scattered light. The fluorescence is focused onto a pinhole rejecting stray and out of focus light and keeping the Raman scattered light to a minimum. A single photon detector is used to count the photons, and the recorded photon trace is then evaluated according to the chosen FFS method [1–6].

The confocal setup provides a small sampling volume, an excellent signal to noise ratio (SNR), and good statistical accuracy. In vitro, the sample concentration is chosen to maximize the SNR [7, 8]. For instance, typical sampling volumes of 250 aL and nanomolar concentrations of the analyte are mostly used. However, many reactions in biology or biochemistry demand measurements at micromolar concentrations. This results in a high number of labeled molecules

in the confocal volume, with in consequence a small fluctuation amplitude or a high photon number beyond the linear range of single photon detectors.

In order to perform these experiments, the size of the sampling volume needs a further reduction. Webb et al. addressed the problem by limiting the sampling volume in their setup to far less than 1 μl by using nano-wells in an aluminium mask [9]. A potential drawback is the background from direct-reflected excitation light. Micro-channels in fused silica have been used as well and sampling volumes of less than 2 μl were achieved [10]. Another approach took advantage of a parabolic mirror in a total internal reflection fluorescence correlation spectroscopy (TIR-FCS) setup, which resulted in a sampling volume of about 5 μl [11]. Hassler et al. reported small sampling volumes of 60 μl by taking advantage of a high numerical aperture objective (NA = 1.45) and an evanescent field excitation [12]. They showed a high SNR as well as high count rates per molecule (CPM) and used their setup for binding-unbinding studies as well as for investigations of enzyme reactions [13].

In this project, we fabricated sub-wavelength sized circular apertures in a thin gold film in order to reduce the sampling volume. Back-illumination of such an aperture results in a highly confined excitation field. With the Green's tensor technique [14], we calculated an excitation volume of about 7 μl for an aperture with 150 nm diameter in a 150 nm thick gold film on top of a glass cover slip. This results in a reduction of the excitation volume by more than an order of magnitude. The detection volume is as for a conventional approach given by the confocal setup. The fluorescence is recorded from the volume in and just above the aperture while the metal mask shields most of the excitation light. Finally, the evaluation of the fluorescence signal provides information about the size of the excitation volume.

Fluorescence in the presence of a structured metal film is very dependent on the local excitation field, the local emission pattern, and the local fluorescence lifetime. Recently, Rigneault et al. reported an increased excitation intensity and a decreased fluorescence lifetime enhancing the CPM in circular aluminium nano-holes [15]. Using rectangular aluminium nano-apertures, Wenger et al. demonstrated that the enhancement is mainly due to a strong evanescent excitation field [16]. Here, we report on trans-illumination measurements collecting fluorescence within but mainly behind a circular nano-aperture. The local fluorescence emission would deserve further investigation but is out of the scope of this paper. Instead, we concentrate on the three-dimensional excitation field, which can also be mapped in detail with the help of a photoresist [17].

2. Experiment

2.1. Aperture masks

The circular apertures were fabricated with a focused electron beam lithography process [18]. A 170 μm glass cover slide was plasma cleaned and covered with 10 nm antimony doped tin oxide. The aperture structures were written into a spin coated high contrast negative tone resist. The resist was developed resulting in freestanding resist structures. These structures were coated with a titanium layer (5 nm) and with a 150 nm thick gold film. A final lift-off process resulted in the apertures shown in Fig. 1. Figure 2 outlines the layout of the entire gold mask. Within six fields, we fabricated a total of 144 arrays of 6×6 apertures. Each field was located and oriented with the help of triangular marks. We verified the dimensions of selected apertures by scanning electron microscopy (SEM). In addition, we checked all aperture arrays with an optical trans-illumination microscope (Carl Zeiss AxioVert 200m with Carl Zeiss AxioCam HRm). The inset in Fig. 2 shows the image of a homogeneous array used for measurements.

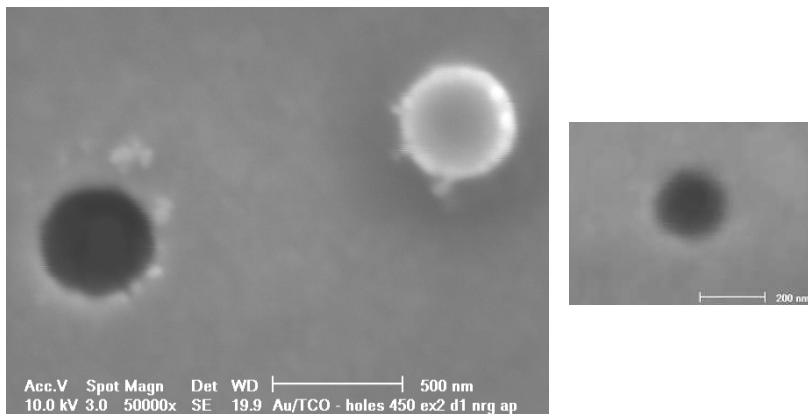


Fig. 1. Left: SEM image of a 420 nm aperture after evaporation of the 150 nm thick gold film. We noticed small gold particles around the aperture edge. Nanoscale particles and fibers were also found at the border of the gold cap. Right: SEM image of a single 230 nm aperture within a 6×6 array. This aperture was exempt of nearby gold particles.

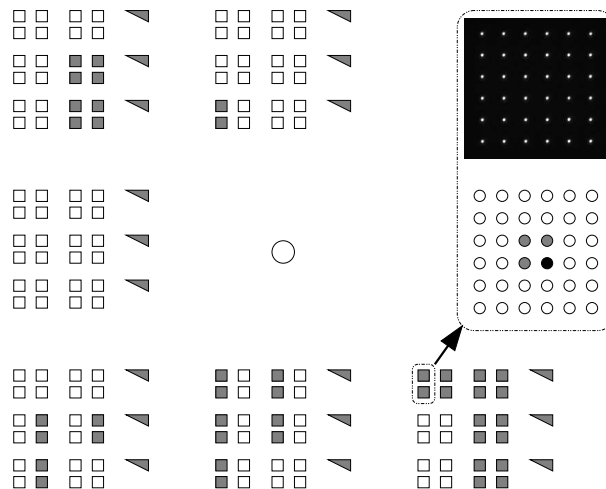


Fig. 2. Mask layout with orientation triangles and aperture arrays. Every square represents an array with 6×6 apertures of identical diameter. In each array, the apertures are located on a square grid with $5 \mu\text{m}$ period. We selected 21 array pairs in order to cover aperture diameters between 115 nm and 520 nm. Inset: Trans-illumination image and scheme of an array pair with $2 \times 6 \times 6$ apertures of 300 nm diameter in the 150 nm gold film. The central apertures in the selected arrays were measured with FCS.

2.2. Experimental setup and measurements

Figure 3 outlines our confocal trans-illumination setup with a piezo xyz -translation stage (Newport ULTRAlign 561D with μ Drive Controller ESA-C) for the sample positioning. A 12 mW HeNe gas laser (Laser 2000 LHRP-1201, linearly polarized) and a laser-line clean-up filter (Chroma Z633/10x) provided a spectrally pure 633 nm excitation. The beam was expanded to fill the aperture of a Carl Zeiss 40x0.90 NA water immersion objective. The beam waist in the focus was 350 nm. Neutral density filters (Thorlabs NDK01) were used to adjust the power in the excitation volume. The fluorescent light was collected with a 40x1.20 NA water immersion objective (Carl Zeiss) and filtered by a dichroic mirror (Chroma Q660LP), a band-pass filter (Chroma HQ710/100m) and a pinhole (Thorlabs ASFxx/125Y step-index fibers: 37.5 μ m, 50 μ m or 100 μ m core diameter). The pinhole provided a spatial filtering, hence contributing to the background rejection as well as to the limitation of the detection volume. A single photon counting module (PerkinElmer SPCM-AQR-14-FC) detected the fluorescence photons. The signal (number of photons over time) was correlated with a USB hardware correlator (Correlator.com Flex990EM-12C) attached to a standard PC. The liquid sample, sandwiched between the aperture mask and a microscope slide, was positioned with the mask in the focal plane.

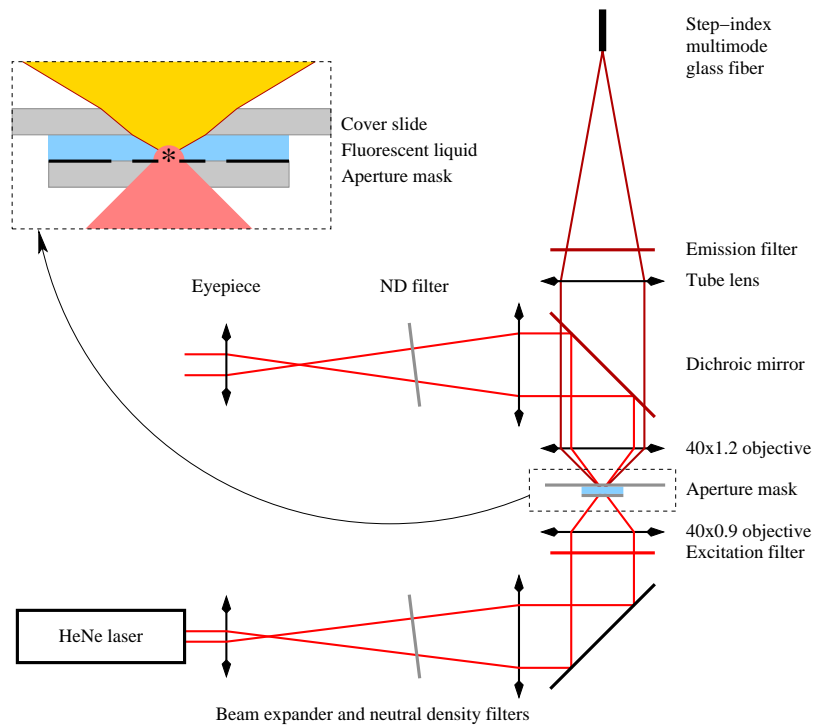


Fig. 3. Confocal trans-illumination setup. The 40x0.9 objective and the multimode fiber were mounted on xyz -translation stages. The aperture mask was aligned with a piezo xyz -translation stage.

3. Theory

The FCS and FFS theory was recently reviewed by Krichevsky et al. [19]. Following the general ideas, the fluorescence intensity $I(t)$ is correlated during a time interval T . The symmetrically

normalized auto-correlation function is defined as

$$G(\tau) = \frac{\langle I(t)I(t+\tau) \rangle}{\langle I(t) \rangle \langle I(t+\tau) \rangle} = (T - \tau) \frac{\int_0^{T-\tau} I(t)I(t+\tau) dt}{\int_0^{T-\tau} I(t) dt \int_{\tau}^T I(t) dt} \quad (1)$$

The auto-correlation $G(\tau)$ allows to extract essential single molecule parameters from the fluctuating fluorescence intensity. Typical fluctuation sources are diffusion (Brownian motion) of fluorescent particles through the detection volume; emission characteristics like triplet state occupation; or changes of the molecular conformation influencing the emission characteristics. The correlation amplitude is inversely proportional to the number of fluctuation sources (particles) in the detection volume. The shape of the correlation curve encodes all these processes, whereas the time dependencies modify the corresponding time windows.

3.1. Excitation field

Figure 4 shows the excited fields for three different aperture diameters calculated with the Green's tensor technique [14]. We simulated the transmission of a Gaussian beam through the apertures in the gold film. The Gaussian beam had a wavelength of 633 nm and was linearly polarized along the x -axis corresponding to the HeNe laser. In the glass substrate with a refractive index of 1.52, it was focused and centered on the bottom of the aperture. The transmission for an incident beam waist $w_0 = 350$ nm was simulated. In the aperture and on top of the gold film, we set the refractive index to 1.33 for water. The relative dielectric constant of the gold film was $-11.6 + 1.26i$.

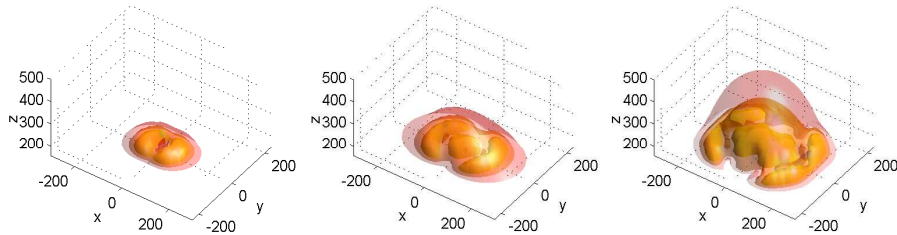


Fig. 4. Simulated excitation fields for aperture diameters of 150 nm (left), 250 nm (center) and 400 nm (right) in a gold film of thickness $h = 150$ nm. All dimensions are given in nanometers. The coordinate origins are located in the center at the bottom of each aperture. A Gaussian beam with 633 nm wavelength was focused with an opening angle equivalent to a numerical aperture of 0.6 on the apertures. The graphs show three surfaces of equal intensity at $e^{-1}I_{max}$ (inner surfaces), $e^{-1.5}I_{max}$ (middle surfaces) and $e^{-2}I_{max}$ (outer surfaces). I_{max} is the maximal excitation intensity at $z = h$. On top of the apertures, the average intensity was reduced to 22%, 73% respectively 87% of the incident intensity at the bottom.

For the 400 nm aperture, the excitation field is similar to the focus of the Gaussian beam. The aperture mainly truncates the tails of the Gaussian beam and diffraction shrinks the vertical extension to 330 nm after the hole. In the close vicinity of the aperture, the excitation field shows a fine structure reflecting the x -polarization of the incident beam and the wave modes in the aperture. With the 250 nm aperture, the y -extension of the excitation volume is slightly smaller, whereas the z -dimension is reduced significantly. This effect is even more important for the 150 nm aperture, where the excitation field extends only 80 nm into the liquid. Table 1

compares the extensions of the ellipsoid-like excitation fields and the estimated volumes. We estimated the excitation volume V_{ex} with W_1 [22] and the effective sampling volume V_{eff} for FCS with W_1^2/W_2 , where

$$W_n = I_{max}^{-n} \iiint I_{(\vec{r})}^n d\vec{r} \quad (2)$$

Here, we approximated the product of the excitation intensity and the detection efficiency by the excitation intensity alone. This is valid because the excitation intensity drops much faster than the detection efficiency, if $\vec{r} \rightarrow \infty$. In both cases, we added the aperture volume $V_{ap} = \pi h d^2/4$, where $h = 150$ nm is the aperture depth and d the diameter.

Table 1. Calculated extensions of the excitation fields along the x , y and z axes, respectively excitation volumes $V_{ex} = W_1 + V_{ap}$ and effective sampling volumes $V_{eff} = W_1^2/W_2 + V_{ap}$ for different aperture diameters d . The extensions are understood as e^{-2} "half-axes" for comparison with the e^{-2} xy -waist $w_0 = 350$ nm of the incident beam.

d	150 nm	250 nm	400 nm	∞^*	∞^\diamond	∞°
w_x	140 nm	240 nm	230 nm	350 nm	250 nm	180 nm
w_y	100 nm	140 nm	200 nm	350 nm	250 nm	180 nm
w_z	80 nm	160 nm	330 nm	2.0 μm	1.0 μm	700 nm
V_{ex}	6.7 al	17 al	38 al	130 al	130 al	55 al
V_{eff}	27 al	64 al	130 al	480 al	590 al	250 al

* At the glass surface without aperture. In free liquid, $V_{ex} = 260$ al and $V_{eff} = 960$ al.

\diamond State-of-the-art in free liquid for 633 nm wavelength [20].

\circ State-of-the-art in free liquid for 488 nm wavelength [20].

We would like to emphasize that diffraction and interference generate these highly confined excitation fields. In \vec{k} -space, diffraction creates a transverse component k_{xy} parallel to the xy -plane. Because the length of the wave vector \vec{k} is constant, k_z has to adopt according to

$$k_z^2 = k^2 - k_{xy}^2 \quad (3)$$

Sub-wavelength sized apertures enforce $k_{xy} > k$ resulting in an imaginary k_z . This gives the transmitted field a dominant evanescent field character along the z -axis. The vertical extension w_z decreases with the aperture diameter. Moreover, the lateral extensions decrease due to destructive interference of many surface waves with different k . A simulation at identical conditions but at a wavelength of 488 nm showed that the excitation field *grows* along the z -axis. Using sub-wavelength sized apertures, we took advantage of diffraction to obtain highly confined excitation fields below the far-field diffraction limit.

3.2. Auto-correlation model equation

As an approximation, we used the standard model equation for free diffusion of a single fluorescent species through a sampling volume with a 3D Gaussian shape [21, 22]. We modeled the normalized auto-correlation $G(\tau)$ by

$$G(\tau) = G_\infty + \left(1 - \frac{I_B}{\langle I \rangle}\right)^2 \frac{\gamma}{N} \left\{ \left(1 + \frac{\tau}{\tau_d}\right)^{-1} \left(1 + \frac{\tau}{K^2 \tau_d}\right)^{-1/2} + \frac{P_t}{1 - P_t} \exp\left(-\frac{\tau}{\tau_t}\right) \right\} \quad (4)$$

$G_\infty \approx 1$ is the correlation amplitude in the long lag time limit $\tau \rightarrow \infty$, N is the average number of molecules in the sampling volume, τ_d is the lateral diffusion time, K is the ratio of axial over

lateral extension of the sampling volume, P_t is the probability of molecules in the triplet state and τ_t is the correlation time of this triplet state population. I_B is the background count rate and $\langle I \rangle$ is the mean count rate (fluorescence intensity and background). In our case, we assumed γ to be $1/2$ because the mask cuts half of the sampling volume [12]. Figure 5 shows typical correlation amplitudes for different aperture diameters. For apertures larger than 250 nm, Eq. (4) yielded good results. For smaller apertures, the auto-correlations had a significant tail for lag times τ between 0.1 ms and 1 ms. We attribute the tail to constrained diffusion in the aperture,

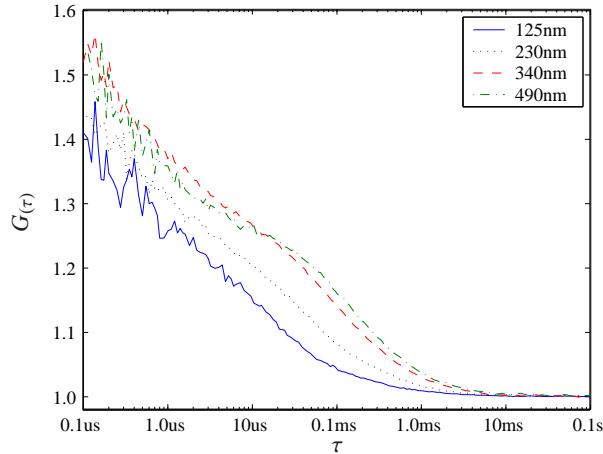


Fig. 5. Afterpulsing corrected auto-correlations $G(\tau)$ versus lag time τ for aperture diameters of 125 nm, 230 nm, 340 nm and 490 nm at a Cy5 concentration of 12 nM. The correlation amplitude for the 490 nm aperture was multiplied by 3. For the 125 nm and the 230 nm aperture, the correlation amplitudes show a different slope for delays between 0.1 ms and 1 ms. We interpret this as constrained diffusion of molecules entering into the 150 nm deep aperture.

i.e. molecules entering into the 150 nm deep aperture were laterally captured for some time interval. Therefore, they needed more time to diffuse out of the sampling volume. The boundary conditions for Eq. (4) are not taking into account this trapping inside the aperture. This leads to a mismatch if the fit is based on Eq. (4). Figure 6 shows fits and residuals for measurements at a Cy5 concentration of 30 nM. In free liquid and for the 490 nm aperture, Eq. (4) fits well with low residuals. For the 125 nm aperture, Eq. (4) leads to significant residuals and even a bias at large lag times. Nevertheless, the extracted diffusion time τ_d is a good approximation because it accounts only for the diffusion in the xy -plane. Also, the number of molecules N depends mainly on the correlation amplitude $G(0)$ and the triplet probability. Therefore, it does not change significantly for different diffusion models.

3.3. Evaluation of the auto-correlation

For analyzing the experimental auto-correlation curves, we corrected the correlation amplitude for afterpulsing to avoid a systematic bias on short diffusion times. Figure 7 shows how afterpulsing affected the auto-correlation amplitude up to a lag time $\tau \approx 10 \mu\text{s}$. According to Bismuto et al. [23], we estimated the afterpulsing contribution by averaging auto-correlations G_{uc} for an uncorrelated source (daylight). For minimizing the discrepancies between the curves, we introduced an exponent for the mean count rate $\langle I_{uc} \rangle$.

$$G_{ap}(\tau) = \left\langle (G_{uc}(\tau) - 1) \langle I_{uc}(t) \rangle^{1.02} \right\rangle \quad (5)$$

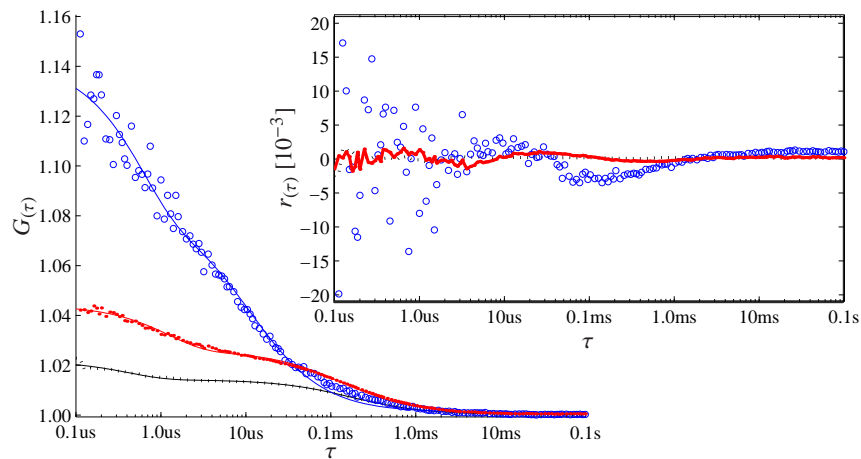


Fig. 6. Auto-correlations and fits $G(\tau)$ versus lag time τ for aperture diameters of 125 nm (blue circles), 490 nm (red points) and for free liquid (black dotted) at a Cy5 concentration of 30 nM. Inset: Fit residuals $r(\tau) = G_{fit}/G(\tau) - 1$.

Subtracting the estimated afterpulsing contribution $G_{ap}/\langle I \rangle^{1.02}$ prior to parameter extraction allowed to analyze diffusion times shorter than 20 μs accurately. The model parameters were extracted by fitting the curves with Eq. (4) on the measured auto-correlations. For fitting, we used a non-linear least-squares algorithm (multidimensional Gauss-Newton algorithm). The background count rate I_B and the mean count rate $\langle I \rangle$ were measured directly.

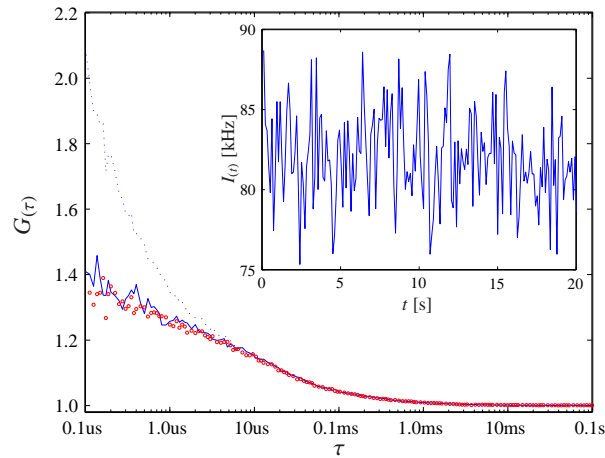


Fig. 7. Auto-correlations $G(\tau)$ versus lag time τ measured on a 125 nm aperture at a Cy5 concentration of 12 nM. The blue dotted line is the measured auto-correlation. The solid line shows the afterpulsing corrected amplitude. The circles trace a second measurement on the same aperture. Inset: intensity trace.

3.4. Prediction of FCS results

In case of free diffusion, the diffusion time τ_d is given by $w_0^2/4D$ where w_0 is the lateral beam waist and D the diffusion constant [22]. In our case, the extension of the sampling volume is

limited by the excitation field, which in turn is restricted by the diameter d of the aperture. Figure 5 suggests proportionality of the diffusion time and the aperture diameter. Based on our calculations, we expect to find $\tau_d \propto d^2$ for small apertures. For large apertures, the sampling volume is given by the beam waist w_0 and the diffusion time levels off to some value τ_∞ , which might be different from τ_d due to surface effects. Overall, we assume to get a behavior as

$$\tau_d \approx \tau_\infty \frac{d^2}{d_\tau^2 + d^2} \quad (6)$$

where d_τ marks the transition between the small and the large aperture regime. Equation (6) is understood as a first approximation of the effective relationship between τ_d and d .

The number of molecules N is determined by the effective sampling volume V_{eff} and the fluorophore concentration C .

$$N = CN_A V_{eff} \quad (7)$$

Here, $N_A = 6.022 \times 10^{23} \text{ mol}^{-1}$ is the Avogadro number. For small apertures, the sampling volume increases with the aperture diameter as shown in table 1. For large apertures, the sampling volume gets constant because the excitation field is no longer constrained by the aperture. Therefore, we expect a relationship similar to Eq. (6) between N and d .

4. Results and discussion

For the mask layout shown in Fig. 2, we selected 21 array pairs to cover 21 aperture diameters from 115 nm to 520 nm. Figures 8–11 summarize the results for a 150 nm gold mask on a 150 μm glass substrate. A 12 nM respectively 30 nM solution of Cy5 (Molecular Probes) was excited at 633 nm. We kept the laser power constant at 0.3 mW incident onto the apertures.

4.1. Diffusion time

For a concentration of 12 nM, we measured with a 38 μm , a 50 μm and a 100 μm pinhole diameter. Figure 8 shows the diffusion time versus the aperture diameter. For the 115 nm apertures, the diffusion time was around 15 μs . It increased with the aperture diameter and reached 140 μs for the 500 nm apertures. On the 400 nm apertures, we measured $\tau_d \approx 100 \mu\text{s}$ against 20 μs on the 150 nm apertures. This ratio of 1/5 is in good agreement with the calculated ratio of 1/4 for these aperture diameters.

The pinhole diameter had no significant influence on the measured diffusion time. With the 40 \times objective and the 38 μm pinhole, we got a projected pinhole diameter of roughly 1 μm in the mask plane, which was still much larger than the largest aperture. Our measurements show that the excitation volume was effectively smaller than the detection volume, which underlines the insensitivity to pinhole diameter variations. Also, we see that an increase of the fluorophore concentration to 30 nM did not significantly change the measured diffusion time. Only for aperture diameters above 300 nm, a slight increase was measured. We attribute this to detector saturation leading to a virtually increased sampling volume. Figure 10 shows that the detector was driven at more than 1.0 MHz for apertures larger than 300 nm. At these count rates, the detector death time of 50 ns started to become significant – particularly during photon bursts – and biased the FCS results [24].

Overall, Eq. (6) is well reproduced with a transition diameter d_τ of 450 nm and a diffusion time limit τ_∞ of 240 μs . Including the lateral penetration of the excitation light into the aperture walls, the excitation field had a diameter of about 500 nm at d_τ . In agreement with Eq. (6), d_τ marked the aperture diameter yielding 1/2 of the beam cross-section πw_0^2 . In free liquid, we measured a diffusion time $\tau_d \approx 160 \mu\text{s}$. When the confocal volume was placed at the cover slide

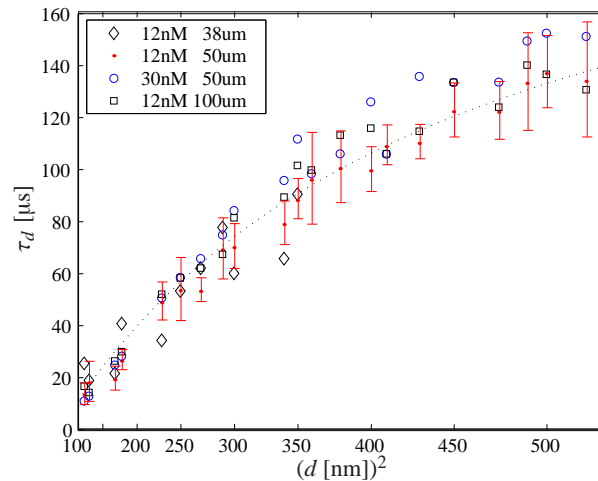


Fig. 8. Diffusion time τ_d versus aperture diameter d . The data points show the average and the error bars the standard deviation of 10 measurements per aperture diameter. For clarity, the standard deviation is shown for one case only (12 nM Cy5, 50 μm pinhole). The black dotted line was calculated with Eq. (6) for $\tau_\infty = 240 \mu\text{s}$ and $d_\tau = 450 \text{ nm}$. In free liquid, the diffusion time was 160 μs to 170 μs . Inset: concentration of Cy5 and pinhole diameter of all cases.

surface, τ_d reached 250 μs to 300 μs , which is consistent with τ_∞ . For the smallest apertures, τ_d was less than 1/10 of the value measured in free liquid. We conclude that the introduction of the 115 nm apertures reduced the lateral extension of the excitation volume to less than 1/3. Hence, the measured diffusion times indicate a reduction of the sampling volume to less than 1/10 of the conventional confocal volume.

4.2. Number of molecules

For a Cy5 concentration of 30 nM, we show the number of molecules obtained by fitting the afterpulsing corrected auto-correlations in Fig. 9. For an aperture diameter of 115 nm, we measured about 3 molecules in average in the sampling volume. Increasing the aperture diameter to 350 nm increased the number of molecules to about 12. Then, the number of molecules leveled off between 14 and 18 for larger apertures, which was roughly 1/4 the value in free liquid. The measured ratios of the number of molecules for the 150 nm, 250 nm and 400 nm apertures are close to the calculated ratios of the sampling volumes V_{eff} in table 1.

In contrast to the diffusion time, the number of molecules is affected by the background contribution of each individual aperture. Therefore, we measured first the background on each aperture with pure water. With the Cy5 solution, we measured these apertures again. However, it was virtually impossible to mutually realign the confocal volume and the apertures identically. Therefore, the excitation intensities differed by as much as 20% resulting in a 40% variance in the background corrected number of molecules. This made it difficult to measure the sampling volume for an individual aperture.

4.3. Signal to noise ratio

Figure 10 shows the background, the mean intensity and the SNR measured during the experiment described in subsection 4.2. The mean intensity increased with d^2 from about 90 kHz on the 115 nm apertures to 1.8 MHz on the largest apertures. On the other hand, the background

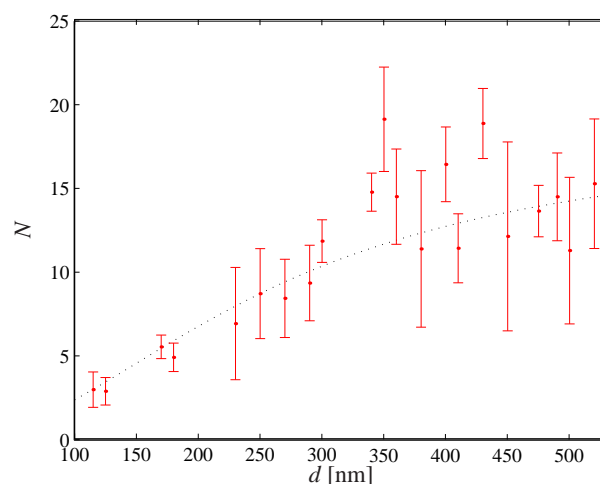


Fig. 9. Number of molecules N versus aperture diameter d for a Cy5 concentration of 30 nM and a 50 μm pinhole. The data points show the average and the error bars the standard deviation of 10 measurements per aperture diameter. The dotted line is for guiding the eyes. In free liquid, we measured about 72 molecules in the confocal volume.

depended very much upon the state of individual apertures. Its standard deviation was particularly low for apertures smaller than 200 nm. Thereby, despite the small signal, we were able to predict and correct background accurately for these apertures.

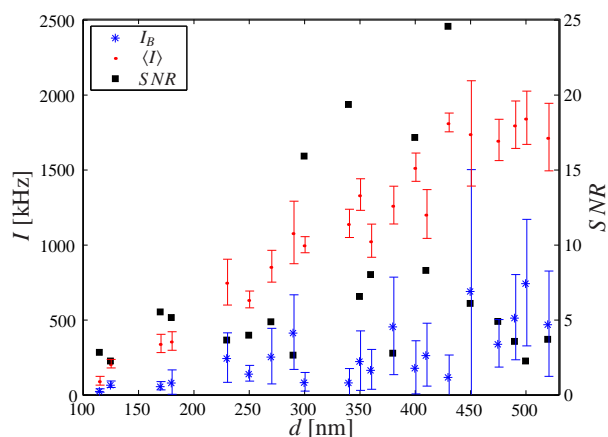


Fig. 10. Background count rates I_B , mean intensity $\langle I \rangle$ and $SNR = \langle I \rangle / I_B - 1$ versus aperture diameter d for a Cy5 concentration of 30 nM and a 50 μm pinhole. The data points show the average and the error bars the standard deviation of 10 measurements per aperture diameter. In free liquid, we measured an intensity of 4.7 MHz and a background of 6 kHz.

For aperture diameters up to 200 nm, we measured SNRs between 2.5 and 6. The best results were obtained with aperture diameters of 300 nm, 340 nm and 430 nm with corresponding SNRs of 16, 19, respectively 25. Typically, conventional instruments provide a $SNR > 50$ (2 kHz background, 100 kHz to 500 kHz mean intensity). By increasing the Cy5 concentration, we could reach a $SNR > 10$ for aperture diameters up to 200 nm. In our experiment, the SNR

was limited by the large background, which was mainly due to photo-luminescence of the gold [25] and the glass slide; surface enhanced Raman scattering [26] of water molecules, particularly at the aperture edge; and fluorescence of photo-resist residues if any. By mastering the lithography process, we could remove any photo-resist residue. For reducing the background further, we compared the photo-luminescence of different materials. For instance, we measured the photo-luminescence of silver and found it an order of magnitude lower than for gold. Nevertheless, we kept using gold for greater compatibility with biological applications (surface chemistry).

4.4. Count rate per molecule

Figure 11 shows the CPM obtained from the experiment described in subsection 4.2. Starting at about 23 kHz for the 115 nm apertures, the CPM increased quickly to about 61 kHz for the 250 nm apertures. Then, there was only a slight increase to about 82 kHz for the 400 nm apertures. This behavior qualitatively follows the calculated excitation intensities. The intensity on top of the 250 nm aperture is about 3.3 times the intensity of the 150 nm aperture, but only about 12% lower than for the 400 nm aperture.

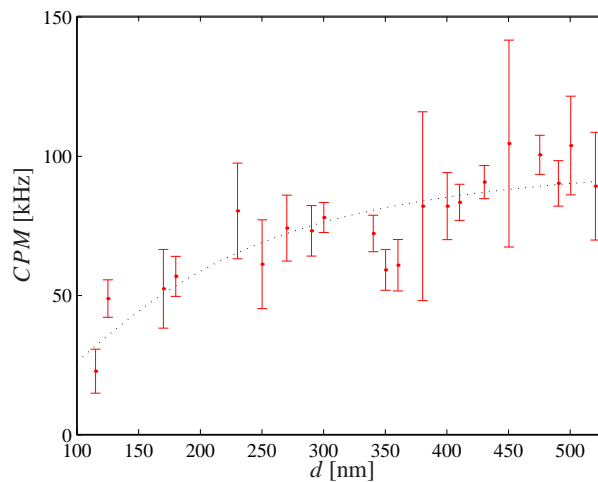


Fig. 11. Background corrected count rate per molecule CPM versus aperture diameter d for a Cy5 concentration of 30 nM and a 50 μm pinhole. The data points show the average and the error bars the standard deviation of 10 measurements per aperture diameter. The dotted line is for guiding the eyes. In free liquid, we obtained a $CPM \approx 65$ kHz for this experiment.

If we compare the values for the large apertures, we notice that the count rates per molecule exceed the values measured in free liquid. We interpret this by the mirror effect of the gold film, which reflects a significant part of the fluorescent light emitted towards the aperture and the gold film. In particular, the emission under high incidence angles falls onto the gold film surrounding the aperture and is efficiently reflected back into the objective. For instance, we measured a CPM of 103 kHz in case of the 500 nm apertures exceeding the CPM in free liquid by 60%.

5. Conclusions

We demonstrated that FCS on single apertures is an interesting approach for molecular investigations at 10 nM to 100 nM concentration. Using apertures of various sizes, we calculated

and engineered the excitation field. For small apertures, we verified that the diffusion time and the number of molecules are proportional to the aperture diameter. We measured a reduction of the effective sampling volume by an order of magnitude compared to the typical volume in confocal FCS.

The background on individual apertures was hard to predict, particularly for the large apertures. Therefore, we encountered some difficulties measuring the number of molecules and the count rate per molecule accurately. Nevertheless, the average values confirmed our calculations. In particular, we could report comparable or even higher count rates per molecule than in confocal FCS. Using homogeneous aperture arrays and an optimal combination of materials, excitation wavelength and power, we expect to measure all FCS parameters accurately.

We would like to point out that confocal trans-illumination FCS performs nearly as well as confocal epi-illumination FCS. With trans-illumination, the excitation light falls directly onto the detection pinhole. Therefore, the emission filter has to block the full excitation power instead of the small fraction of backscattered light. This results in a somewhat higher background but can be compensated by using two microscope objectives on either side of the sample, thereby doubling the detection efficiency. Finally, the alignment of the excitation and detection volumes is more precise since the small aperture serves as a common pinhole.

Acknowledgements

We gratefully acknowledge the Swiss National Science Foundation (SNSF) for financial support (contract number 200021-103333) and Benjamin Dwir at EPFL for electron-beam and nanostructuring assistance.

Marcel Leutenegger

born in August 11, 1976, at Altdorf (UR), Switzerland.

La Vy de Ballens
1145 Bière (VD)
Switzerland

marcel.leutenegger@a3.epfl.ch



Master EPF in Microengineering
Doctor of Science

Education

- 2003–2007 Ph.D. studies at the Laboratoire d'Optique Biomédicale LOB, École Polytechnique Fédérale de Lausanne EPFL, 1015 Lausanne, Switzerland.
Thesis title: *Single Molecule Detection on Surfaces*.
Director: Prof. Theo Lasser.
- 1999–2003 Studies in microengineering at EPFL.
Master project: *Design and evaluation of subwavelength apertures*.
Supervisor: Prof. Theo Lasser, LOB, EPFL.
- 1998–1999 Military services
- 1997–1998 Studies in microengineering at EPFL

Professional experience

- 2004: 2 years Teaching assistance for undergraduate students at EPFL.
Courses: *Photonique appliquée* and *Physique générale IV*.
- 2002: 3 months Creation of online support *Experimental optics* and *eTeaching* assistance at the Section Microtechnologie SMT, EPFL.

Languages

- German: mother tongue.
- French, english: spoken, read and written.

Skills in informatics

Advanced library programming in assembler, C and C++. Advanced Internet programming in HTML, CSS, Java and JavaScript. Experienced user of MATLAB and simulation tools like MIT Photonic-Bands or Finite Element Magnetic Methods.

Interests

Mountaineering, diving, programming, cooking and reading.